Studying the role of Arp2/3 complex in cell migration

Congying Wu

A dissertation submitted to the faculty of the University of North Carolina at Chapel Hill in partial fulfillment of the requirements for the degree of Doctor in Philosophy in the Department of Cell Biology and Physiology.

Chapel Hill
2013

Approved by:

James E. Bear, PhD

Keith Burridge, PhD

Richard Cheney, PhD

Kenneth Jacobson, PhD

Steven Rogers, PhD

Abstract

CONGYING WU: Studying the role of Arp2/3 complex in cell migration
(Under the direction of Dr. James E. Bear)

The actin cytoskeleton plays important roles in maintaining cell shape and mediating cell motility. Deregulation of actin dynamics occurs during pathological processes such as cancer metastasis, regeneration defects and developmental diseases. One specific form of actin cytoskeleton, the highly dynamic branched actin network, is critical for the formation and regulation of cell cortex and protrusions during cell migration and matrix degradation. The key nucleator for this branched actin network is the seven-protein Arp2/3 complex.

Functional studies of Arp2/3 *in vivo* have been severely hampered by effects on viability observed upon loss of this complex in a variety of organisms. Using fibroblasts derived from Ink4a/Arf-deficient mice, we generated a stable line depleted of Arp2/3 complex that lacks lamellipodia. This line shows defective random cell motility and relies on a filopodia-based protrusion system. Utilizing a microfluidic gradient generation system, we tested the role of Arp2/3 complex and lamellipodia in directional cell migration. Surprisingly, Arp2/3-depleted cells respond normally to shallow gradients of PDGF indicating that lamellipodia are not required for fibroblast chemotaxis. Conversely, these cells cannot respond to a surface-bound gradient of extracellular matrix (haptotaxis). Consistent with this finding, cells depleted of Arp2/3

fail to globally align focal adhesions suggesting that one principle function of lamellipodia is to organize cell-matrix adhesions in a spatially coherent manner.

Arp2/3-branched actin is critical for cell morphology and migration. However, perturbations and diseases affecting this network have phenotypes that cannot be fully explained by cell-autonomous effects. Using this stable Arp2/3 knockdown cell line, we also report the non-autonomous effects upon Arp2/3 depletion. We show that the main class of genes with altered expression levels was genes encoding secreted factors including chemokines, growth factors and matrix metaloproteases resembling the senescence associated secretory phenotype (SASP). These factors affect EGF chemotaxis in a non-autonomous way, resolving the recent contradictions about the role of Arp2/3 in chemotaxis. We indicate that these genes are targeted by NF-κB, via a CCM2-MEKK3 pathway that has been implicated in osmotic stress signaling. Thus, perturbations of Arp2/3 have potential non-autonomous effects which should be considered when evaluating diseases affecting the Arp2/3-actin cytoskeleton.

Our work has provided strong evidence that Arp2/3 complex is critical for lamellipodia and revealed the roles of Arp2/3-branched actin in cell-matrix interaction. We have also indentified and characterized novel non-cell-autonomous effects of perturbing the branched actin network which has potential clinical relevance.

Acknowledgements

I would like to first thank my advisor Dr. James Bear for the opportunity to work in his lab. He has been a wonderful mentor ever since my rotation days in graduate school. He has not only taught me how to do research, but also inspired me to embrace science.

I am also grateful to have amazing committee members Drs. Keith Burridge, Richard Cheney, Steve Rogers, and Ken Jacobson. Their guidance and advice have helped in my success as a graduate student. I would also like to thank all my collaborators especially Dr. Jack Griffith for their support and help along the way.

I am thankful to be part of the Bear lab, having lots of fun with my dear labmates. I would like to also thank them.

Table of Contents

LIST OF FIGURES

LIST OF ABBREVIATIONS

CP	Compass Parameter
ECM	Extracellular Matrix
EGF	Epidermal growth factor
ELISA	Enzyme-linked immunosorbent assay
FAAI	Focal Adhesion Alignment Index
FAK	Focal Adhesion Kinase
FMI	Forward Migration Index
HGF	Hepatocyte growth factor
KD	Knock Down
KDR	Knock Down-Rescue
PDGF	Platelet-Derived Growth Factor
SASP	Senescence Associated Secretory Phenotype
TIRF	Total Internal Reflection Fluorescence

Chapter 1

Introduction

1.1 Mesenchymal cell migration

Cell migration is important throughout development and under normal physiological conditions. Deregulation of cell migration is associated with disease states such as cancer metastasis, developmental defects, abnormal wound healing and chronic immune diseases [1, 2].

Based on cell morphology and the cellular machineries required, cell migration can be divided into two categories. Ameboid cells constantly change shape by rapidly protruding and retracting extensions that were originally described as pseudopods or “false feet” [3]. Mesenchymal migration describes the slow migration of elongated cells depending on complex cycles of protrusion, adhesion and retraction. It is characterized by a polarized distribution of actin filaments, with a network of short branched actin filaments at the leading edge, and polymers of actin filaments arranged into distinct classes of actin stress fibers behind the leading edge [4]. Mesenchymal cells send out actin-based protrusions in the forms of finger-like filopodia or sheet-like lamellipodia, forms focal adhesions linking extracellular matrix and actin stress fibers to generate force and employs actin-myosin contraction to move forward [5]. During this whole process, actin cytoskeleton plays important roles, especially at the very dynamic cell leading edge.

1.2 Actin at the leading edge of migrating cells

When cells migrate on 2D surfaces, they send out protrusions in the forms of filopodia or lamellipodia, both of which are actin-rich structures. Filopodia mainly contain bundled actin filaments, nucleated by formins and crosslinked by actin bundling proteins such as villin, fascin and espin [6]. Lamellipodia on the other hand contain actin networks of a dendritic geometry. These branched actin filaments are primarily nucleated by the Arp2/3 complex and modified by other branch associated proteins such as type one coronins [7, 8]. The polymerization of leading edge actin is tightly regulated by multiple signaling pathways involving kinases, proteases and small GTPases. Crosstalks at different levels exist in this signaling network and the roles of the two major actin protrusions have not been thoroughly clarified before our study [9-11].

1.3 Arp2/3 complex overview

Arp2/3 complex was first purified in a biochemistry screening for proteins interacting with profilin, an actin binding protein. The Arp2/3 complex contains seven protein subunits. Two of the subunits are actin related proteins Arp2 and Arp3. Based on the crystal structures, Arp2 and Arp3 mimic actin monomer structurally. They associate with the pointed end of the daughter filament and are predicted to seed new actin filaments. The other five subunits (ARPC1-5) provide a framework for positioning these two Arp subunits at the pointed end of the daughter filament which branches off of the mother filament [12]. Mapping the Arp2/3 complex crystal structure into the cryoEM actin filament structure has suggested models how different subunits interact with actin filaments [13].

The Arp2/3 complex is highly conserved in virtually all eukaryotes [14]. Biochemical and structural studies show that the Arp2/3 complex binds existing actin mother filaments, and initiates daughter filaments as branches off of the mother filaments at a characteristic angle of 70° [15]. Ar p2/3 by itself is not a potent actin nucleator. The activity of Arp2/3 depends largely on its nucleotide status, its interaction with the nucleation promoting factors (NPFs) and its binding to actin mother filament [16, 17]. ATP binding to Arp3 has been shown to induce a global conformational change on the complex, and increase its affinity for NPFs [18]. NPFs interact with Arp2/3 and prime the complex for activation by inducing additional conformational change. The Arp2/3 complex is further activated upon binding to the actin mother filament. NPFs also deliver ATP-bound G-actin to Arp2 and Arp3 subunits for the initiation and polymerization of the daughter filaments. In addition, several classes of negative regulators of the Arp2/3 complex have been identified in the past few years, including GMF[19], Coronins 1B [8], Gadkin[20] and PICK1[21]. Arp2/3 complex activity may also be regulated via functional interactions with actin binding proteins such as capping protein, which promotes Arp2/3-mediated filament nucleation [22].

The functional role of Arp2/3 complex in actin branch formation in cells has been confirmed by many, but not all studies. Functional studies of Arp2/3 in vivo have been severely hampered by effects on viability observed upon loss of this complex in a variety of organisms, leading to the prevailing notion that Arp2/3 complex is essential for viability in eukaryotes [23-26].

1.4 Directional cell migration

Random motility has important roles and is thought to allow cells to effectively sample their environment such as in the case of affinity maturation of B cells in the germinal center [27]. However, in vivo, cell migration is largely directional, as in the context of embryogenesis and wound healing. Cells can sense an extracellular cue, usually in a gradient, and signal to the cytoskeleton machinery, reorients the polarity and move towards (or against) the more concentrated cue. This directional migration involves not only complex cell motility machineries, but also intricate feedback loops in order to maintain directionality while being able to fine tune the signaling pathways under changing environment [28].

Three main types of directional migration have been classified: chemotaxis, haptotaxis[29] and durotaxis[30]. Chemotaxis describes cell migration towards a gradient of soluble factors, such as growth factors, cytokines and chemokines. Haptotaxis describes cell migration up an insoluble gradient, such as a gradient of extracellular matrix, or a gradient of chemokine bound to the matrix [29, 31] (Figure 1). Durotaxis involves more of the mechanosensation pathways. It refers to cell migration guided by gradients in substrate rigidity [30].

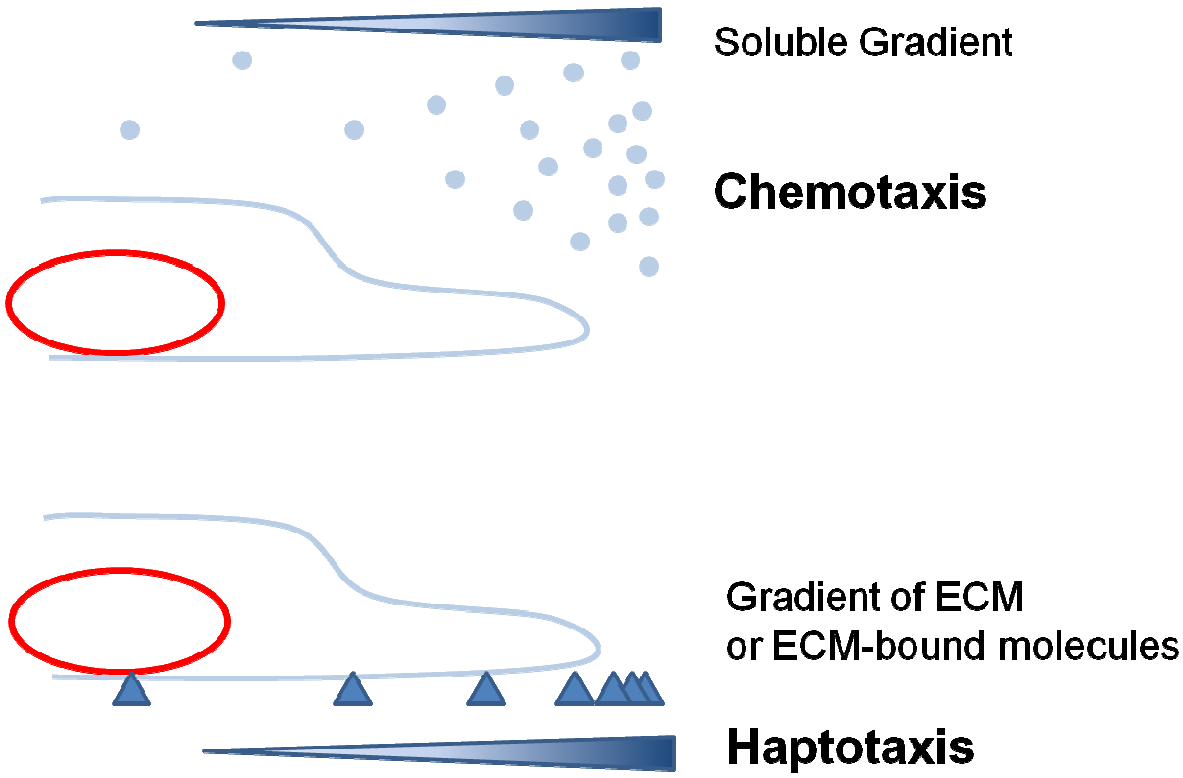

Figure 1 Models showing chemotaxis vs haptotaxis

Chemotaxis describes cell migration towards a gradient of soluble factors, such as growth factors. Haptotaxis describes cell migration up an insoluble and bound gradient, such as a gradient of extracellular matrix, or a gradient of molecules bound to the matrix.

1.5 Non-cell-autonomous effects of secretory factors

Perturbation of the cytoskeleton is tightly linked to abnormal cell migration [8, 32]. The direct or indirect autonomous effects of actin perturbation on cell motility have been reported in drug perturbation, genetic depletion or overexpression systems [29, 32, 33]. However, under these conditions and in cases of human diseases involving altered actin cytoskeleton, signaling changes caused by actin perturbation may also induce non-cell-autonomous effects which have largely been understudied.

It has long been noticed that the perturbation of cytoskeleton machinery affects signaling pathways [34-36]. Depolymerization of microtubules release the guanine exchange nucleotide factor GEF-H1, increasing Rho activity and resulting in increased actomyosin contraction [37]. It has also been reported that certain actin drugs lead to incresed NF-κB activity [38, 39]; however, its mechanism or effects on cell physiology have not yet been addressed. Emerging data has revealed that NF-κB signaling is the major signaling pathway which stimulates the appearance of SASP (the senescence associated secretory phenotype), in which senescent cells secrete pro-inflammatory factors [40]. All of these senescence-associated secreting factors are involved in homeostatic disorders such as cancer [41]. These factors including growth factors, cytokines and chemokines, are also likely to cause non-cell-autonomous effects on cell migration. Thus, the intriguing potential crosstalk among actin cytoskeleton perturbation, increased NF-κB activity, secretory factor release and non-autonomous effects on cell migration becomes extremely exciting and interesting to study.

Chapter 2

Arp2/3 is critical for lamellipodia and response to extracellular matrix cues but is dispensable for chemotaxis

2.1 Summary

Lamellipodia are sheet-like protrusions at the cell leading edge. They are composed of dendritic actin networks initiated by the seven-subunit protein complex Arp2/3. It is widely recognized that lamellipodia are critical for cell motility, however, whether Arp2/3 complex is required for directional migration has not been vigorously tested. We generated a stable cell line depleted of the Arp2/3 complex using fibroblasts derived from Ink4a/Arf-deficient mice. These Arp2/3-depleted cells lack lamellipodia, show defective random cell motility and rely on a filopodia-based protrusion system.

With this unique cell line, we tested the role of Arp2/3 complex and lamellipodia in directional cell migration using a microfluidic gradient generation system. To our surprise, Arp2/3-depleted cells respond normally to shallow gradients of PDGF. This result indicates that lamellipodia are not essential for fibroblast chemotaxis. In contrast, these cells lost the ability to respond to a surface-bound gradient of extracellular matrix (haptotaxis). Consistently, we also found that the Arp2/3-depleted cells show defected global alignment of their focal adhesions. This result

suggests that one important role of Arp2/3-branched actin and lamellipodia is to organize cell-matrix adhesions in a spatially coherent manner.

Introduction

Cell motility is an essential feature in a number of biological processes such as embryonic development, immune responses, and would heading. Deregulation of this process is leads to a variety of diseases including cancer metastasis, autoimmune disorders and developmental defects [2, 42]. Random cell migration allows cells to effectively sample their environment such as in the case of affinity maturation of B cells in the germinal center [27]. However, under most conditions, cell migration is a directional process and is frequently governed by various directional cues such as soluble factors (chemotaxis), substrate-bound factors (haptotaxis) or mechanical cues (durotaxis). Thus, it is an important topic in modern biology to understand how cells sense and respond to these directional cues.

Among these three types of directional migration, chemotaxis is perhaps the most well understood form. It involves a variety of signaling pathways connecting cell surface receptors to the motility machinery inside of cells [43]. These signaling cascades are thought to trigger directional protrusions at the leading edge through controlling actin polymerization pathways [44]. However, these results are based mainly on studies of rapidly migrating amoeboid cells such as neutrophils and *Dictyostelium* cells; little is known about directional migration in mesenchymal cells. Haptotaxis and durotaxis are much more poorly studied. They are thought to involve signaling events triggered by adhesive receptors such as integrins [45].

Fibroblasts are mesenchymal cells that perform a variety of tissue repair functions and respond to directional cues such as gradients of PDGF [46]. In addition, the *in vitro* motility of these cells has been extensively studied. The sheet-like, protruding leading edge of fibroblasts known as the lamellipodium contains a dense array of actin filaments arranged in a dendritic meshwork [47]. Extensive experimental evidence and theoretical models of lamellipodial protrusion indicate that the polymerization of actin filaments within this meshwork drives protrusion [22]. In addition to its function in protrusion, the lamellipodium is the site of formation for most cell-matrix adhesions [48]. Integrin binding to extracellular matrix (ECM) proteins and subsequent clustering lead to the formation of nascent focal complexes appearing continuously at the distal margin of the lamellipodium. A subset of the focal complexes mature into focal adhesions that are connected to bundled actin stress fibers.

The central pillar of the actin network found in lamellipodia is the seven-subunit Arp2/3 complex. The structure, regulation and biochemical properties of this complex have been extensively studied *in vitro* [reviewed in 49]. Once activated by nucleation promoting factors (such as SCAR/WAVE), Arp2/3 nucleates actin daughter filaments as branches off of existing mother filaments. The localization of Arp2/3 to actin filament branches *in vivo* [8, 47] and the functional role of this complex in lamellipodia formation in cells has been confirmed by many [50-52], but not all studies [53]. Recently, the existence of actin branches in lamellipodia has been called into question by experiments using alternate electron microscopy techniques [54].

Functional studies of Arp2/3 *in vivo* have been severely hampered by effects on viability observed upon loss of this complex in a variety of organisms. Genetic deletion of Arp2/3 subunits is lethal in yeast and *Dictyostelium*, and mouse knockouts produce pre-implantation lethality [23-25]. These data led to the prevailing notion that Arp2/3 complex is essential for viability in eukaryotes [26]. Here we describe a cell line derived from Ink4a/Arf-deficient mice that can support near complete and stable depletion of Arp2/3 subunits without compromising viability. This cell line has allowed us to directly test the role of Arp2/3 and lamellipodia in fibroblast chemotaxis and haptotaxis.

Results

Development of a stable Arp2/3-depleted cell line

The Bear lab has previously generated a clonal, mouse embryonic fibroblast cell line named IA32. It was derived from an *Ink4a/Arf*-/- animal with unusually large lamellipodia [8]. In order to visualize Arp2/3 in live cell, we developed a stable cell line with fluorescently-tagged Arp2/3 complex in this background. Utilizing an established lentiviral shRNA knockdown-rescue (KDR) system, we deplete the endogenous p34Arc subunit of the Arp2/3 complex and simultaneously express a GFP-tagged, RNAi-resistant subunit [55]. We separated single cell clones of fibroblasts infected with this construct and probed for p34Arc by western blot (Figure 2). As expected, we detected appropriate depletion and physiological levels of re-expression of the p34Arc-GFP in some clones (e.g. 3G6). To our surprise, we also generated clones that had near complete depletion of the endogenous protein without re-expression of p34Arc-GFP (e.g. 1B3). This result suggested that this cell line in the genetic background of *Ink4a/Arf-/-* (lacking both $p16^{INK4a}$ and Arf), might be able to survive and proliferate in the absence of Arp2/3 complex.

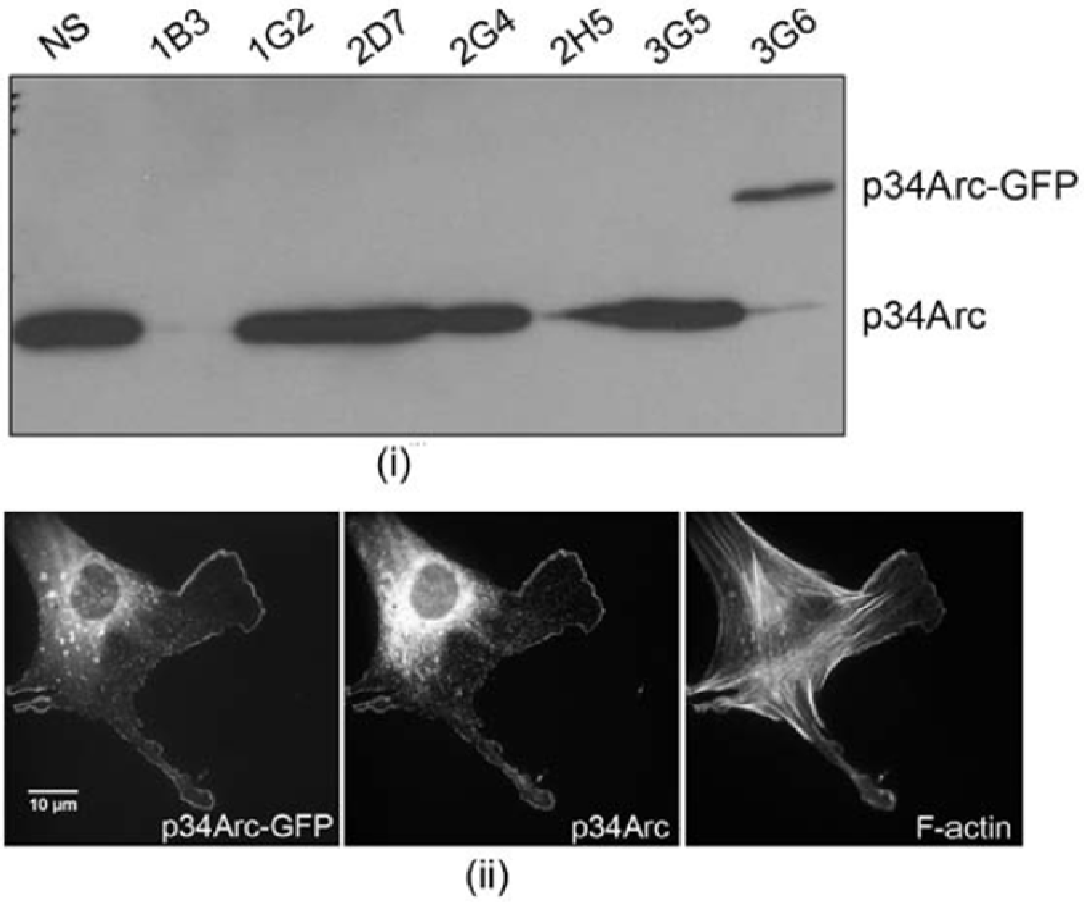

Figure 2 Characterization of p34-KDR cells

Panel (i) shows representative blot of clones from p34-KDR experiment with some clones showing knockdown rescue (3G6) and others showing only knockdown (1B3). Panel (ii) shows a representative p34-KDR cells stained for p34Arc and F-actin.

It has been reported that Arf is playing an important role in cell growth [56], so we repeated the Arp2/3-depletion experiments in early passage wild-type (WT) and *Arf-/-* MEFs (lacking Arf only, but retaining $p16^{INK4a}$). Growth rate was monitored and plotted (Figure 3A). Our result showed that the expression of a non-targeting shRNA (NS) in either background had no effect on cell growth, while depletion of p34Arc (not shown) or the Arp2 subunit strongly reduced the proliferation of WT MEFs, but not *Arf*-/- MEFs These results indicate that in the context of *Ink4a/Arf-/-* or *Arf-/-* MEFs, the Arp2/3 complex is not strictly required for cell viability and that its loss may activate specific growth arrest pathways requiring the Arf tumor suppressor.

We realized that single depletion of either p34Arc or Arp2 in the *Ink4a/Arf-/-* IA32 cell line was not stable. Over time, revertant cells started to re-express the endogenous gene product. To produce a more stable Arp2/3 knockdown, we simultaneously depleted both Arp2 and p34Arc subunits, resulting in a cell line we designated 2xKD (Figure 4). This cell line showed near complete depletion of both subunits by western blot. It also showed decreased level of other subunits of the complex, consistent with previous observations by others (Figure 3B) [52]. This depletion was also observed at the single cell level by immunofluorescence (Figure 3C). Consistent with the growth experiments in early passage MEFs, Arp2/3-depletion in IA32 cells had no effect on cell proliferation (Figure 3D). We used the 2xKD system to study the role of Arp2/3 complex in cell motility.

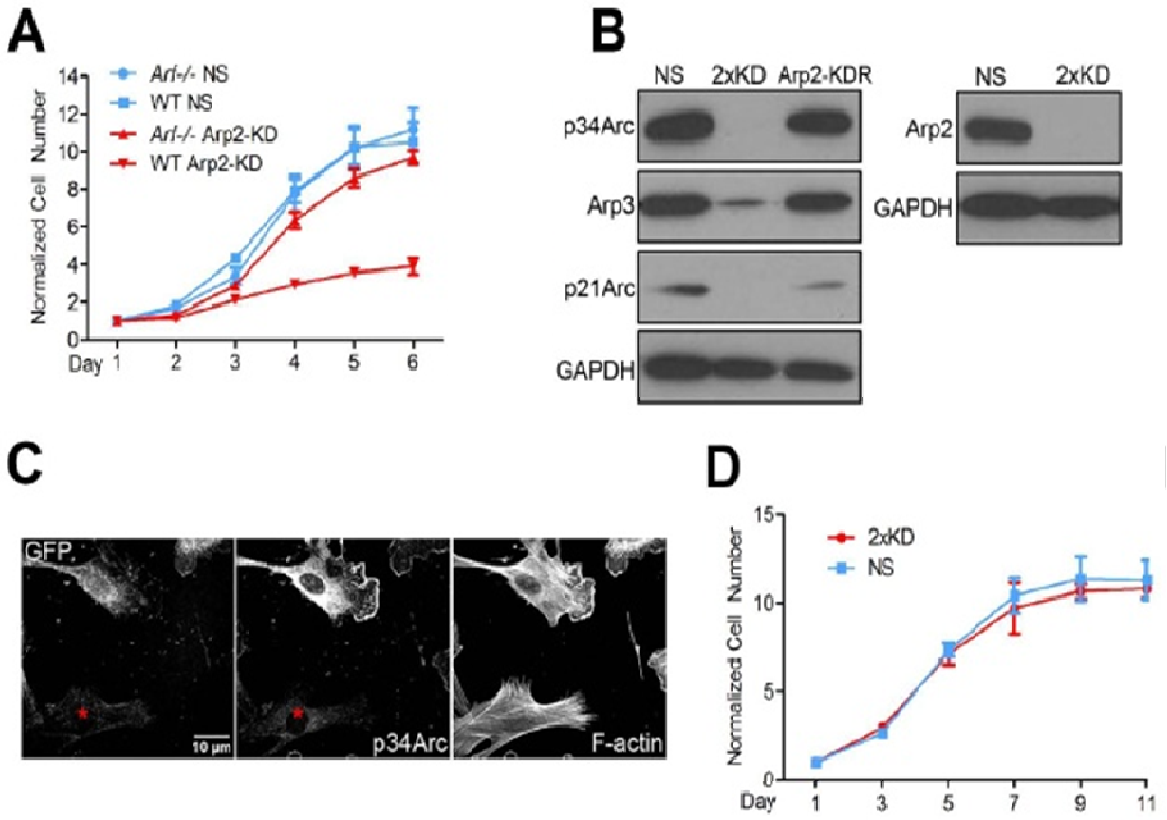
A
Arl-/- NS
WT NS
Arl-/- Arp2-KD
WT Arp2-KD
Normalized Cell Number
Day
B
NS
2xKD
Arp2-KDR
p34Arc
Arp3
p21Arc
GAPDH
NS
2xKD
Arp2
GAPDH
C
GFP
10 µm
p34Arc
F-actin
D
2xKD
NS
Normalized Cell Number
Day

Figure 3: Characterization of 2xKD cells

A) Growth curve of wild-type (WT) and *Arf -/-* early passage MEFs infected with lentivirus expressing a non-specific sequence (NS) shRNA or Arp2 shRNA (Arp2-KD). Error bars: SEM

B) IA32 cells were infected with lentivirus that expressed shRNAs against NS, p34Arc and Arp2 (2xKD), or shArp2 that also co-expressed human Arp2-GFP (Arp2-KDR). Lysates were blotted for p34Arc, Arp3, p21Arc, Arp2 and for GAPDH as a loading control

C) Mixed NS (expressing GFP) and 2xKD cells (marked by red asterisks) were immunostained for p34Arc to verify knockdown of the endogenous gene and phalloidin to visualize F-actin.

D) Growth curve of NS and 2xKD cells. Error bars: SEM

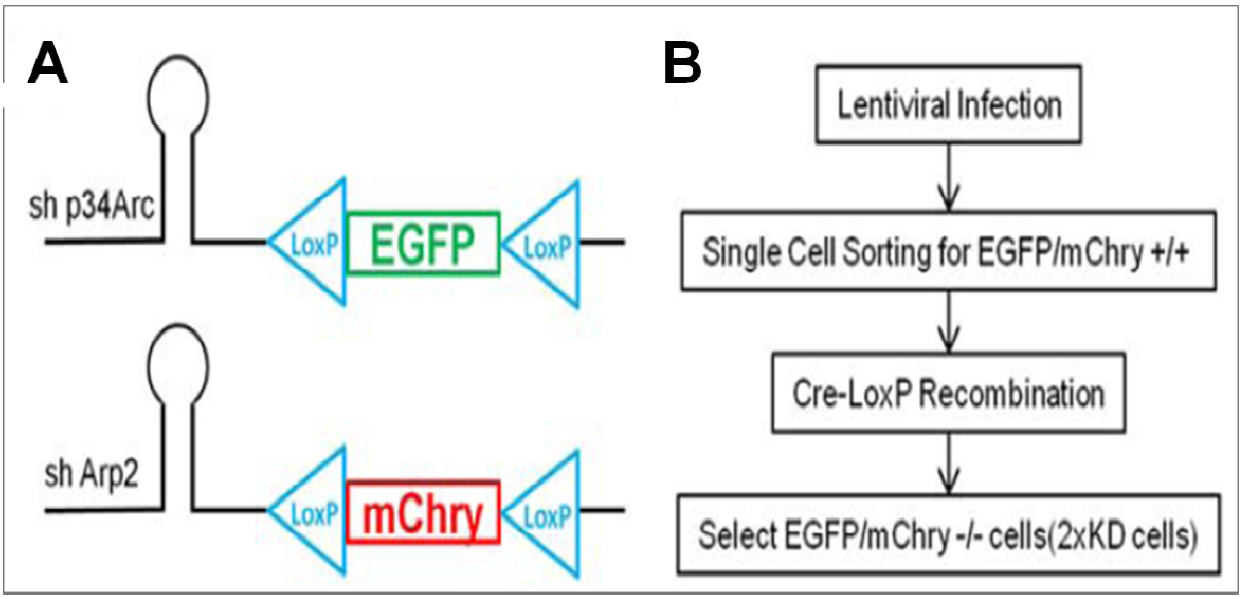

Figure 4 Generation of 2xKD cells

A) Diagram of the lentiviral vector combining p34Arc or Arp2 shRNA expression with EGFP or mCherry (mChry) expression flanked by LoxP sites.

B) Flow chart of stable Arp2/3-depleted cell line (2xKD) generation.

Depletion of Arp2/3 complex leads to the disappearance of lamellipodia and alters actin architecture

Depletion of Arp2/3 complex dramatically changed cell morphology, despite the fact that the proliferation rate is normal. 2xKD cells lost lamellipodia and formed excessive filopodial protrusions (Figure 5A), consistent with the role of Arp2/3 complex in generating branched actin networks within lamellipodia. To confirm that the lack of lamellipodia was indeed caused by the absence of Arp2/3 activity, we microinjected bovine Arp2/3 complex into the 2xKD cells, and observed the reappearance of lamellipodia within 20 min after injection (Figure 5B). This result confirmed the specificity of Arp2/3 depletion and indicated that the upstream activators of Arp2/3 complex were still present and functional in 2xKD cells. These striking changes in cell morphology prompted us to examine the actin cytoskeleton in the absence of Arp2/3 complex. As expected from the lack of morphological lamellipodia, 2xKD cells have a different pattern of phalloidin staining with no areas of enrichment in peripheral regions.

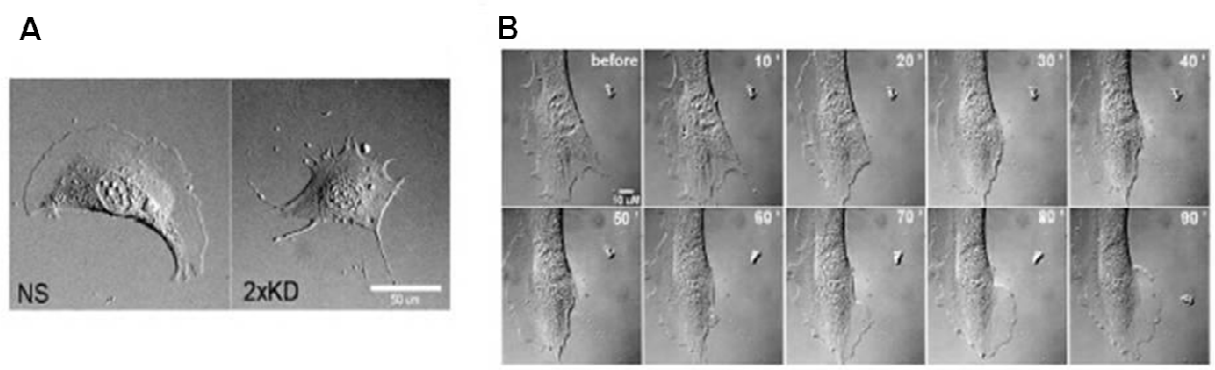

Figure 5 Cell morphology is changed upon Arp2/3-depletion and can be rescued by microinjection of Arp2/3 complex

A) DIC images of NS and 2xKD cells (Scale bar: 50 µm)

B) 2xKD cells were microinjected with 5 mg/mL Arp2/3 complex. Representative time-lapse sequence before and after injection show the reappearance of lamellipodia.

Cyro-shadowing electron microscopy (EM) has recently been described as a method involving rapid freezing, freeze-drying and high-resolution metal shadowcasting for visualizing purified protein complexes [57]. We used this technique to investigate leading edge actin networks in detail. We extended cryo-shadowing EM to the imaging of cells plated directly on EM grids. This method allowed us to prepare the cells without critical point drying and replica formation. By live-cell imaging, we were able to monitor the spreading and formation of protrusions of cells on the grids, confirming that the cells were under normal conditions before any sample preparation. We observed drastically different actin filament architectures at the margins of 2xKD cells compared to the NS control cells (Figure 6). The NS cells had a network of short, interconnected filaments with many examples of branching. This architecture is similar to the networks observed with platinum replica EM previously [47]. On the other hand, the leading edge actin network in 2xKD cells was much sparser, composed of longer filaments that were highly bundled which frequently converged into higher order bundles in filopodia. Actin filament crosslinks and some end-to-side junctions could be observed in the 2xKD cells, suggesting multiple forms of crosslinking and bundling still occur in the absence of the Arp2/3 complex. Overall, our results confirmed the essential role of Arp2/3 complex in generating the densely branched actin networks.

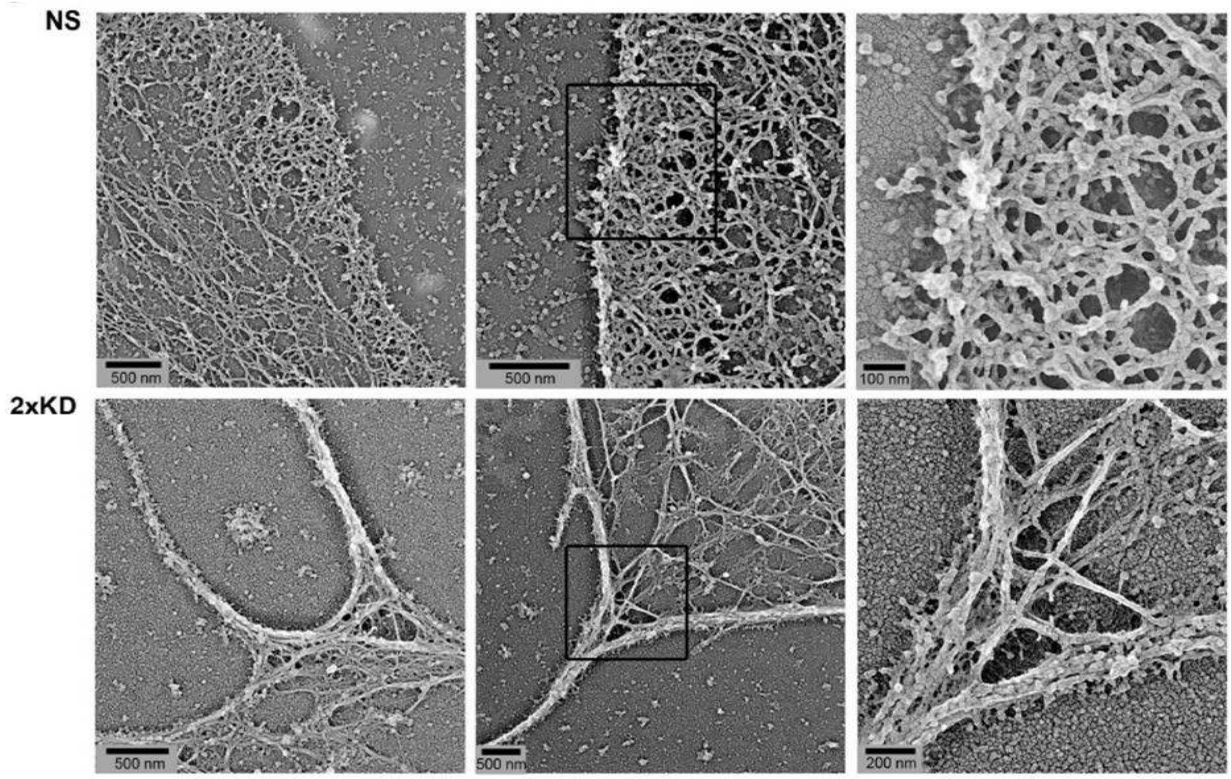

Figure 6 Electron-microscopy revealed altered leading edge actin structure in the absence of Arp2/3 complex

Cryo-shadowing EM images showing the leading edge actin networks of NS and 2xKD cells. Left and middle panels are separate cells, right panel is magnified portion of middle panels indicated by black boxes

Arp2/3-depleted cells show inefficient, filopodia-driven cell motility

Since lamellipodia are thought to play important roles in cell migration, we examined the effect of Arp2/3 depletion and loss of lamellipodia on cell motility. Using single cell tracking, we found that the 2xKD cells and cells singly depleted of either p34Arc or Arp2 showed a marked reduction in migration speed compared to NS cells. The reduced speed was fully rescued in both p34-KDR and Arp2-KDR cells re-expressing RNAi resistant p34Arc or Arp2 subunits respectively, as well as doubly depleted and doubly rescued (2KDR) cells (Figure 7A). This result confirmed that neither of the effects of the respective shRNAs was due to off-target effects.

We also observed a similar reduction of cell speed when NS cells were treated with the Arp2/3 inhibitor CK-666 (100 μM), but not with the inactive compound CK-689 [58]. This same concentration of the Arp2/3 inhibitor did not affect cell speed or morphology of 2xKD cells (Figure 7B), confirming the near complete depletion of Arp2/3 complex and suggesting that the residual motility in 2xKD cells was not dependent on any remaining Arp2/3 complex activity.

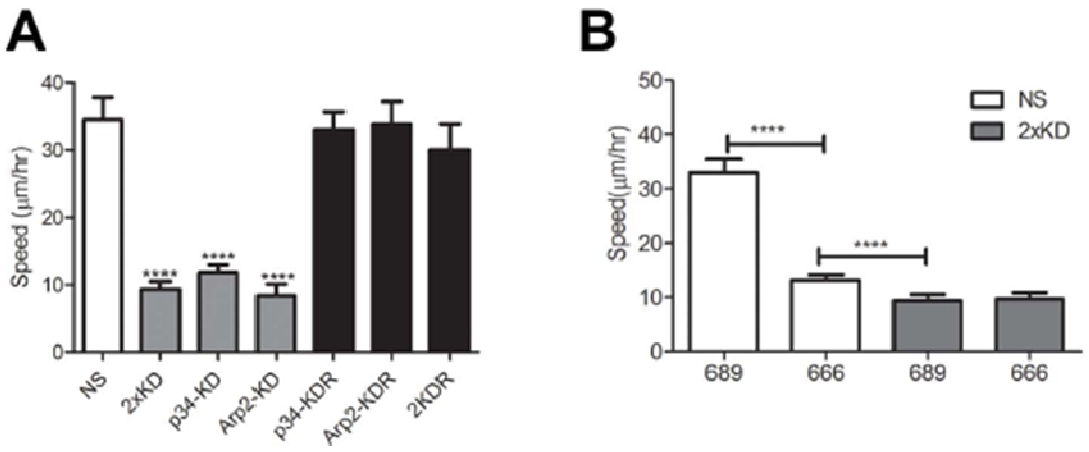

Figure 7 Loss of Arp2/3 activity leads to decreased cell migration speed

A) Time-lapse microscopy of NS, 2xKD, p34-KD Arp2-KD, p34-KDR and Arp2-KDR and 2KDR cell lines was used to determine single-cell speed, depicted in graph. Error bars represent 95% confidence intervals. ****P<0.0001 by Student's *t*-test

B) Single-cell speed of NS and 2xKD cells treated with 100 µM Arp2/3 inhibitor CK-666 or the inactive control compound CK-689. Error bars represent 95% confidence intervals. ****P<0.0001 by Student's *t*-test

One immediate question is whether the residual motility in 2xKD cells was still dependent on actin polymerization. To answer this, we treated cells with latrunculin B (LatB) to inhibit F-actin polymerization. Both NS and 2xKD cells showed significant reduction in cell speed when F-actin polymerization was impaired (Figure 8A), suggesting that the Arp2/3-depleted cells still rely on actin assembly to migrate. One possible mechanism for the 2xKD cells to continue to migrate, although at a much slower speed, is by employing myosin contractility. To address this, we treated cells with a myosin II inhibitor blebbistatin (BLB). In single cell tracking experiment, BLB treatment increased 2xKD cell speed significantly without an effect on the speed of NS cells (Figure 8B). BLB treatment decreased focal adhesion and stress fiber staining, but increased phosphorylation of the myosin light chain at Ser19 (Figure 8C-E), consistent with previous studies [59]. These results indicate that the residual motility of the Arp2/3-depleted cells does not depend on myosin contractility.

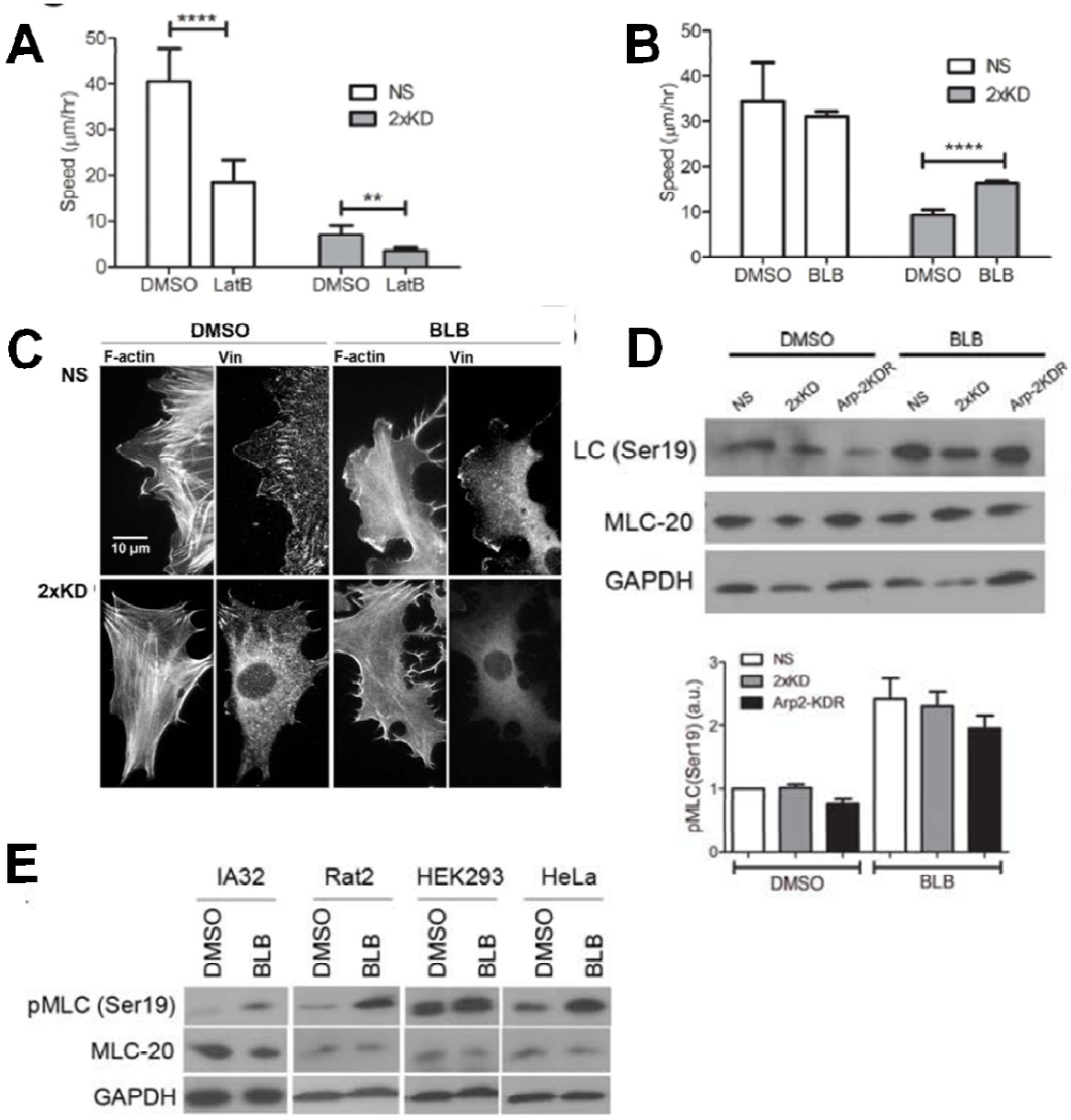

Figure 8 The residual motility in 2xKD cells relies on actin polymerization but not myosin contractility

A) Single-cell speed of NS and 2xKD cells treated with 1μM Latrunculin B (LatB) or DMSO as a control. Error bars represent 95% confidence intervals. ****P<0.0001, **P<0.01 by Student's t-test

B) Single-cell speed of NS and 2xKD cells treated with 15 μM blebbistatin (BLB) or DMSO as a control. Error bars represent 95% confidence intervals. ****$P<0.0001$ by Student's *t*-test

C) NS and 2xKD cells treated with vehicle (DMSO) or BLB (15 μM) were immunostained for endogenous vinculin (Vin) and F-actin (Scale bar: 10 μm). Note the disappearance of focal adhesions and the reorganization of actin stress fibers in both cell types.

D) (upper panel) Cell lysates from NS, 2xKD and Arp2-KDR cells treated with DMSO or BLB were blotted for phospho-myosin light chain (Ser19), total myosin light chain (MLC-20) and GAPDH; (lower panel) bar graph showing pMLC(Ser19) quantification from three independent experiments (normalized to GAPDH). Error bar: 95% confidence interval. No statistically significant differences were observed between the cell lines with either treatment, although BLB caused a significant increase in pMLC (Ser19) levels in all three lines.

E) Cell lysates from IA32, Rat2, HEK 293 and HeLa cells treated with DMSO or BLB were blotted for phospho-myosin light chain 2 (Ser19), total myosin light chain (MLC-20) and GAPDH. Consistent with observations from endothelial cells [59], BLB treatment caused a significant increase in levels of pMLC (Ser19). This effect appears to reflect a feedback loop where reduction of contractility caused by the inhibition of myosin heavy chain activity by BLB induces a calcium-dependent MLCK activation. However, it is important to note that increased pMLC does not reflect increased cellular contractility in this case.

We observed from time-lapse DIC images and F-actin staining that BLB treatment increased filopodia number in 2xKD cells. We quantified filopodia number in NS and 2xKD cells treated with BLB or DMSO control using scanning electron microscopy (SEM) (Figure 9A). Without treatment, 2xKD cells have approximately three-fold more filopodia than NS cells. Under BLB-treatment, filopodia number 2xKD cells increased significantly while the number of filopodia remained unchanged in NS cells (Figure 9B).

Using time-lapse imaging, we observed a very interesting phenomenon that the 2xKD cells create new areas of flat membrane protrusion by “filling-the-gap” between adjacent filopodia. Occasionally, the tips of two adjacent filopodia fuse and the resulting hole fills in. Due to the larger number of filopodia on the BLB-treated 2xKD cells, more of these “filling-the-gap” events were observed (Figure 9C), correlating with higher whole cell motility. Together, these observations suggest that cells have an alternate, filopodia-driven form of protrusion in the absence of Arp2/3 activity which leads to relatively inefficient whole cell translocation.

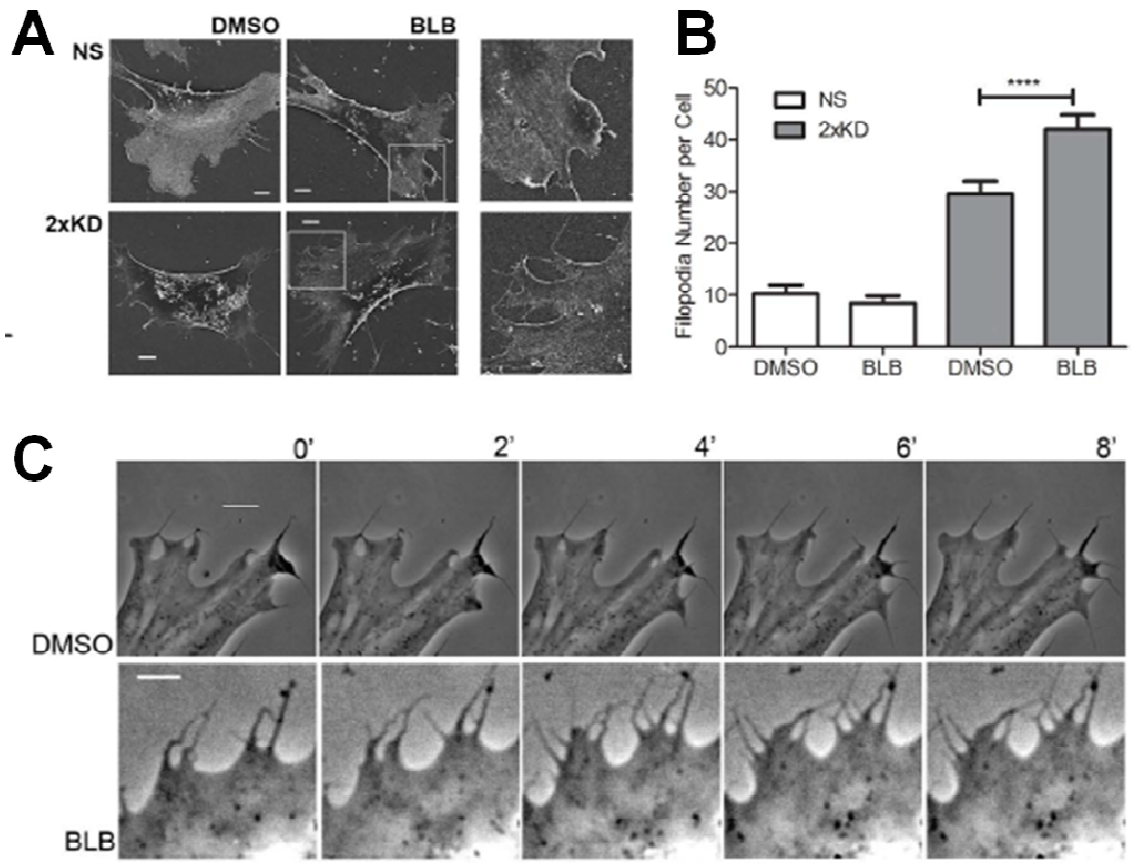

Figure 9: Arp2/3-depleted cells show filopodia-driven cell motility

A) SEM images of NS and 2xKD cells treated with DMSO or BLB

B) Number of filopodia/cell with DMSO or BLB treatment was calculated from >30 cells in each cell line from SEM images. ****P<0.0001 by Student's *t*-test

C) Time-lapse images of 2xKD cells treated with DMSO or BLB. Scale bar: 5 μm

Chemotaxis in the absence of Arp2/3 complex

Cell migration speed and the ability to respond to directional cues are independent properties. Although we have shown that loss of Arp2/3 complex causes changes in leading edge actin organization and disappearance of lamellipodia, leading to reduced random cell motility, whether cell directionality is affected is still unknown. To address this issue, we set up rigorous experimental approaches to separately measure cell speed and directionality by utilizing a modified version of a previously described microfluidic chemotaxis chamber (Figure 10A; [60]). This system allows us to directly image the migration of cells exposed to a defined gradient of chemoattractant for more than 12 hrs, without introducing shear force to cells. The establishment and maintenance of a linear soluble gradient in this device was confirmed using fluorescent dextran (Figure 10B). Based on the fluorescence intensity profile, this equates to a slope of 43.6 %/mm across the cell culture chamber. The average cell in our experiments was ~150 μm across in the dimension of the gradient which yields a chemoattractant slope of ~6.5% across an individual cell. In every experiment, NS expressing GFP and 2xKD cells were seeded in the same cell culture chamber and serum starved prior to establishment of the PDGF gradient. DIC and fluorescent live-cell imaging was used to monitor cell movement. We also monitored gradient stability at each time point by imaging the gradient of Cy5-dextran.

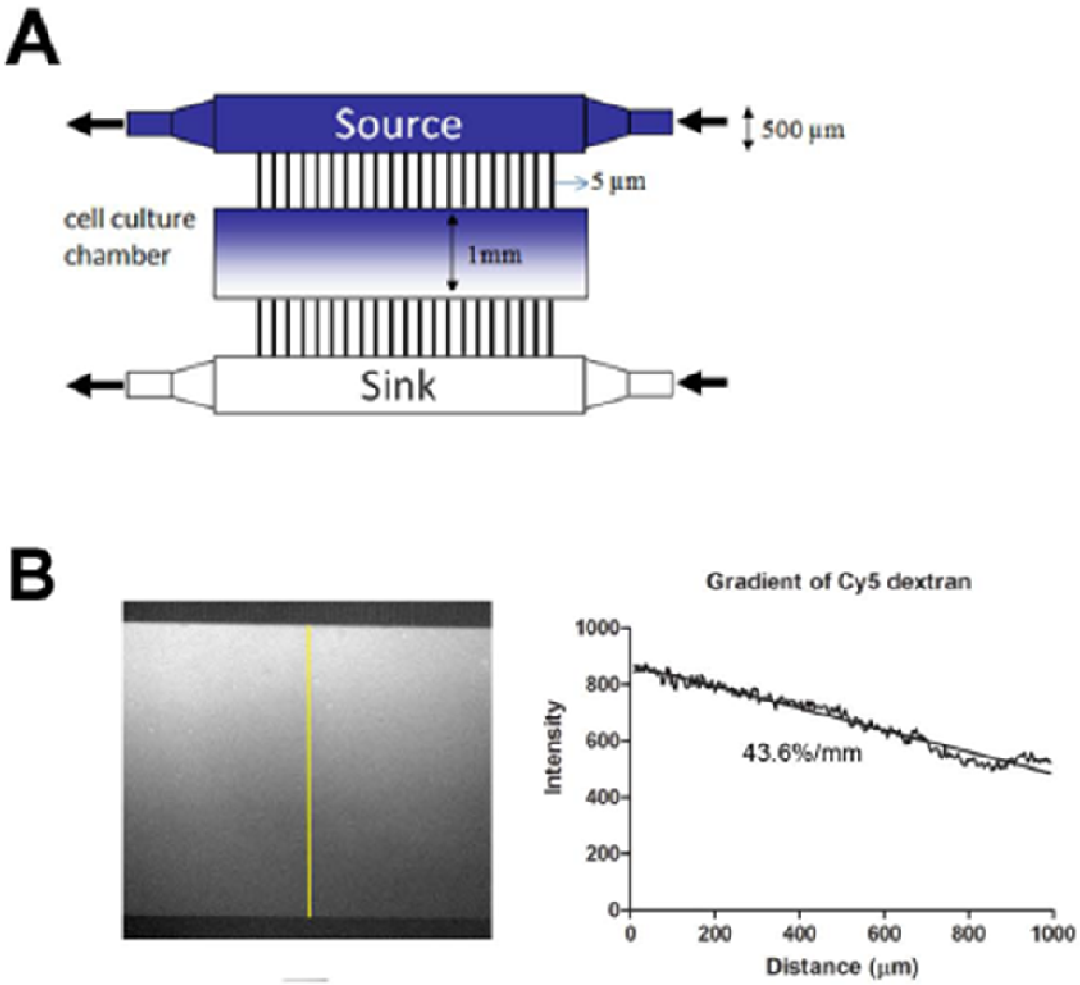

Figure 10 The set-up of chemotaxis devices

A) Schematic of the microfluidic chamber for chemotaxis and haptotaxis experiments

B) Left: fluorescent image of Cy5-dextran gradient formed inside the chamber as an indication of gradient formation and maintenance. Right: line-scan plot of the gradient along the yellow line depicted in the left panel, slope of the gradient is indicated under the curve

We used single cell tracking to follow individual cells over time and calculate the velocity and directionality of migration. Two methods were used to calculate the directionality of chemotactic cells. First, we transposed the tracks so that each had its start point at the origin and then computed the forward migration index (FMI) using the final position of the cell at the end of the track (Figure 11A). Second, we calculated the angle of each turn in the track relative to the gradient and plotted these as a histogram (Figure 11B). Using this distribution of turn angles, we used a non-linear curve fit to compute the compass parameter (CP) as described previously [61].

To our surprise, no statistically significant difference in either FMI or CP was observed between NS and 2xKD cells at all source concentrations of PDGF tested (Figure 11C). This result was further confirmed using Rat2 fibroblasts treated with the Arp2/3 complex inhibitor CK-666, in that the inhibition of Arp2/3 activity had no effect on the ability to respond to the PDGF gradient (Figure 11D). These results suggest that Arp2/3-branched actin and lamellipodia are not required for directional sensing of and responding to chemotactic gradients in mesenchymal cells.

A

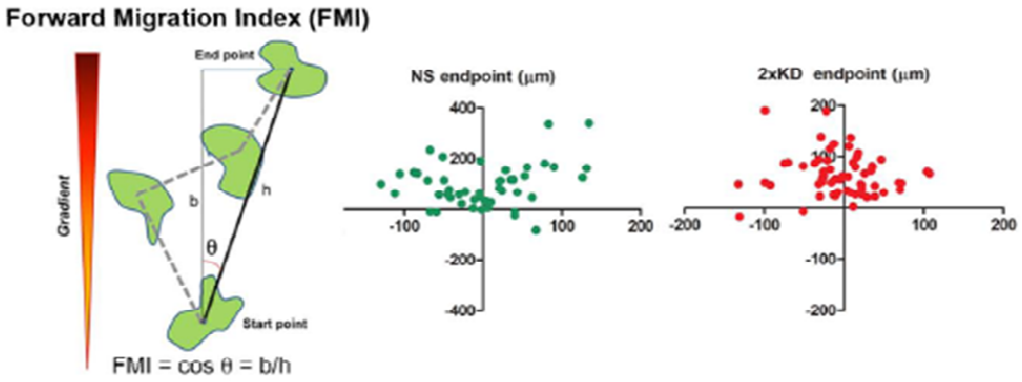

B

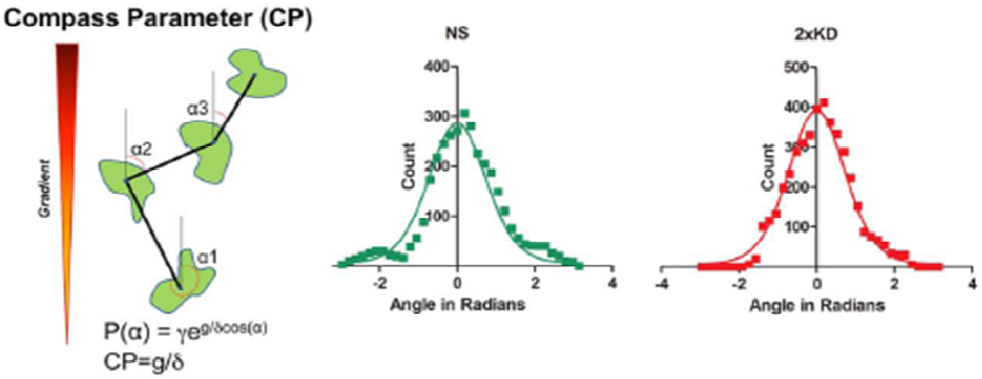

C

		80 ng/mL	120 ng/mL	160 ng/mL
NS	CP	1.38 (1.25,1.52)	1.18 (0.88,1.47)	1.9 (1.60,2.20)
	FMI	0.43 (0.34,0.52)	0.44 (0.33,0.53)	0.53 (0.44,0.62)
	V (μm/hr)	13.07 (10.85,15.29)	21.48 (19.29,23.68)	18.10 (15.56,20.64)
	N	53	74	51
2xKD	CP	1.56 (1.40,1.72)	1.71 (1.55,1.88)	1.97 (1.77,2.17)
	FMI	0.46 (0.36,0.57)	0.50 (0.40,0.60)	0.53 (0.47,0.59)
	V (μm/hr)	10.57 (9.23,11.92)	13.81 (11.96,15.66)	11.42 (9.89,12.94)
	N	63	71	65

D

Rat2 +CK-689	CP	1.43 (1.21,1.64)
	FMI	0.35 (0.29,0.42)
	V (μm/hr)	10.33 (9.18,11.4)
	N	69
Rat2 +CK-666	CP	1.58 (1.49,1.66)
	FMI	0.35 (0.28,0.43)
	V (μm/hr)	5.76 (5.16,6.36)
	N	77

Figure 11 Arp2/3 complex depletion does not affect chemotaxis

A) Diagram showing FMI calculation method and representative end point scatter plots of NS and 2xKD cells in chemotaxis assays (Data from 120 ng/mL source PDGF concentration)

B) Diagram showing Compass Parameter (CP) calculation and representative histograms showing angular turn per step of NS and 2xKD cells in the same PDGF chemotaxis assays. P(α) is the probably distribution of angles measured relative to gradient, γ is a constant, g is the gradient steepness and δ is the angular step size [61]

C) Table showing compass parameter (CP), forward migration index (FMI), velocity (V) and number of cells analyzed (N) in chemotaxis assays with indicated PDGF source concentrations. Numbers in parentheses for each entry are 95% confidence intervals

D) Table showing Rat2 cell chemotaxis parameters in the presence of Arp2/3 inhibitor CK-666 or its inactive control CK-689

To confirm that the PDGF signaling pathway was also unaffected by Arp2/3 depletion, we blotted total and phosphorylated Akt (pAkt) in response to PDGF stimulation. Similar changes in Akt signaling were observed in 2xKD and NS cells upon PDGF stimulation (Figure 12A). We then examined the morphological response of 2xKD cells to acute, uniform stimulation with PDGF, since they still response to PDGF as a chemoattractant. While NS cells produced lamellipodia and ruffles, 2xKD cell increased the number of filopodia (Figure 12B). We also examined 2xKD cells during chemotaxis up a PDGF gradient and observed that these cells had more filopodia on the up-gradient side of the cell (Figure 12C). Together, these results indicate that PDGF signaling is intact in the absence of Arp2/3 complex, but cells without Arp2/3show different morphological responses by producing filopodia in rather than lamellipodia.

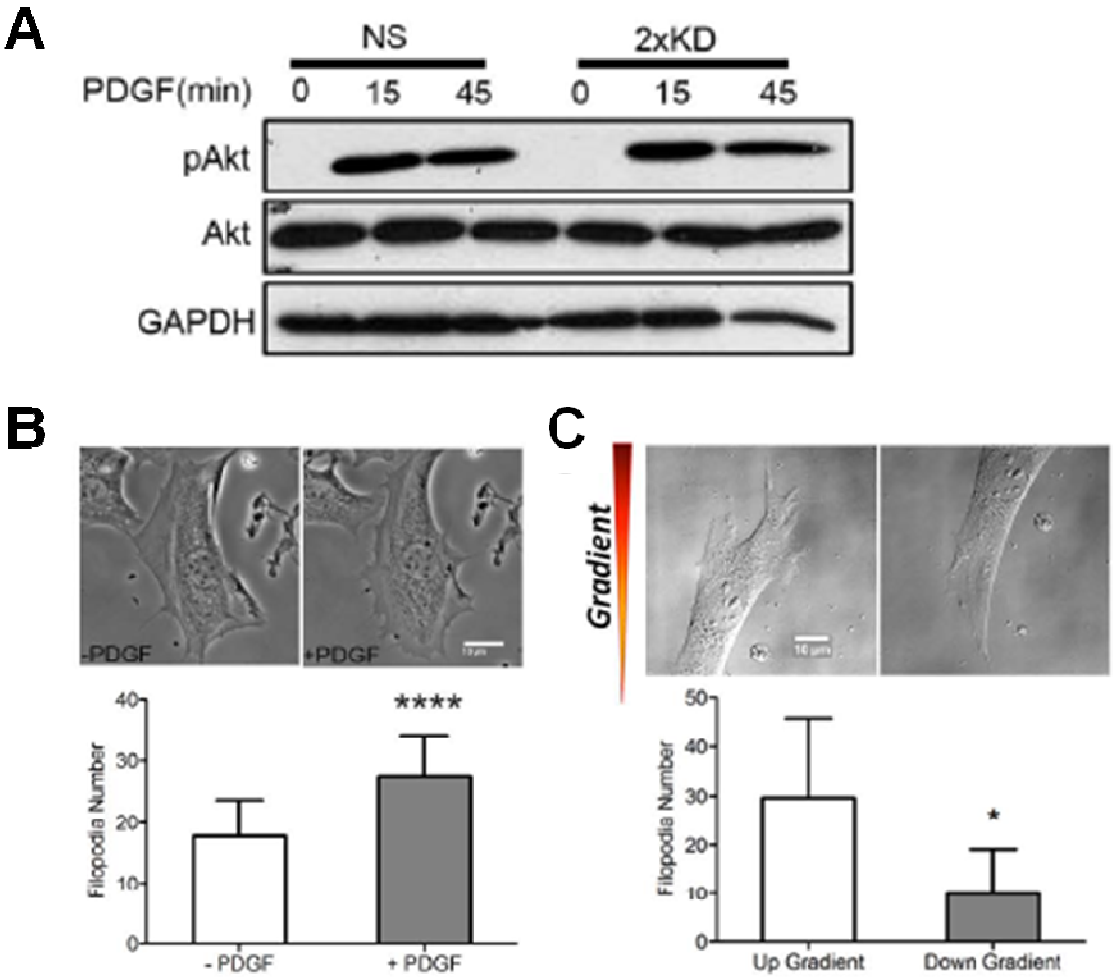
A
NS
2xKD
PDGF(min)
0
15
45
0
15
45
pAkt
Akt
GAPDH
B
-PDGF
+PDGF
Filopodia Number
****
- PDGF
+ PDGF
C
Gradient
Filopodia Number
*
Up Gradient
Down Gradient

Figure 12 Signaling is intact but morphology response is changes in 2xKD cells upon PDGF stimulation

A) Western blotting showing the change of phospho-Akt (pAkt) level upon PDGF stimulation. Cells were serum-starved overnight before stimulation with 40 ng/mL PDGF

B) 2xKD cells before and after PDGF stimulation (images) and the number of filopodia before and after PDGF treatment of 2xKD cells was calculated from >30 2xKD cells. *P<0.05 by Student's t-test

C) Example of the filopodia up and down the PDGF gradient in 2xKD cell chemotaxis was shown and the number of filopodia was calculated from >30 2xKD cells. *P<0.001 by Student's t-test

Depletion of Arp2/3 leads to defects in cell spreading

Cells initiate a spreading process involving the dynamic reorganization of the actin cytoskeleton when they encounter surfaces coated with extracellular matrix proteins. To examine whether Arp2/3-branched actin plays a role in the spreading process during the early cell-matrix interaction, we plated NS and 2xKD cells expressing GFP-Paxillin (GFP-Pax) on fibronectin (FN)-coated surfaces and stained cells at different time-points for F-actin and phospho-tyrosine (pTyr). The 2xKD cells showed a marked delay in spreading kinetics and the expected absence of peripheral lamellipodia (Figure 13A, B). Both pTyr and GFP-Pax showed focal adhesions had formed in the 2xKD cells by 90 min, but most of these adhesions remained associated with the periphery compared with the NS controls.

To quantitatively study the defect in cell-spreading, we used an impedance-based system that measures electrical changes caused by cells interacting with a microelectrode within the surface of a dish. Compared to control cells, the 2xKD cells showed statistically significant decrease in cell spreading (Figure 13C). Consistent with the delay in physical spreading, the 2xKD cells showed delayed and reduced adhesion signaling during spreading by comparing the phosphorylation of Focal Adhesion Kinase (FAK) at Tyr397 through western blotting (Figure 13D).

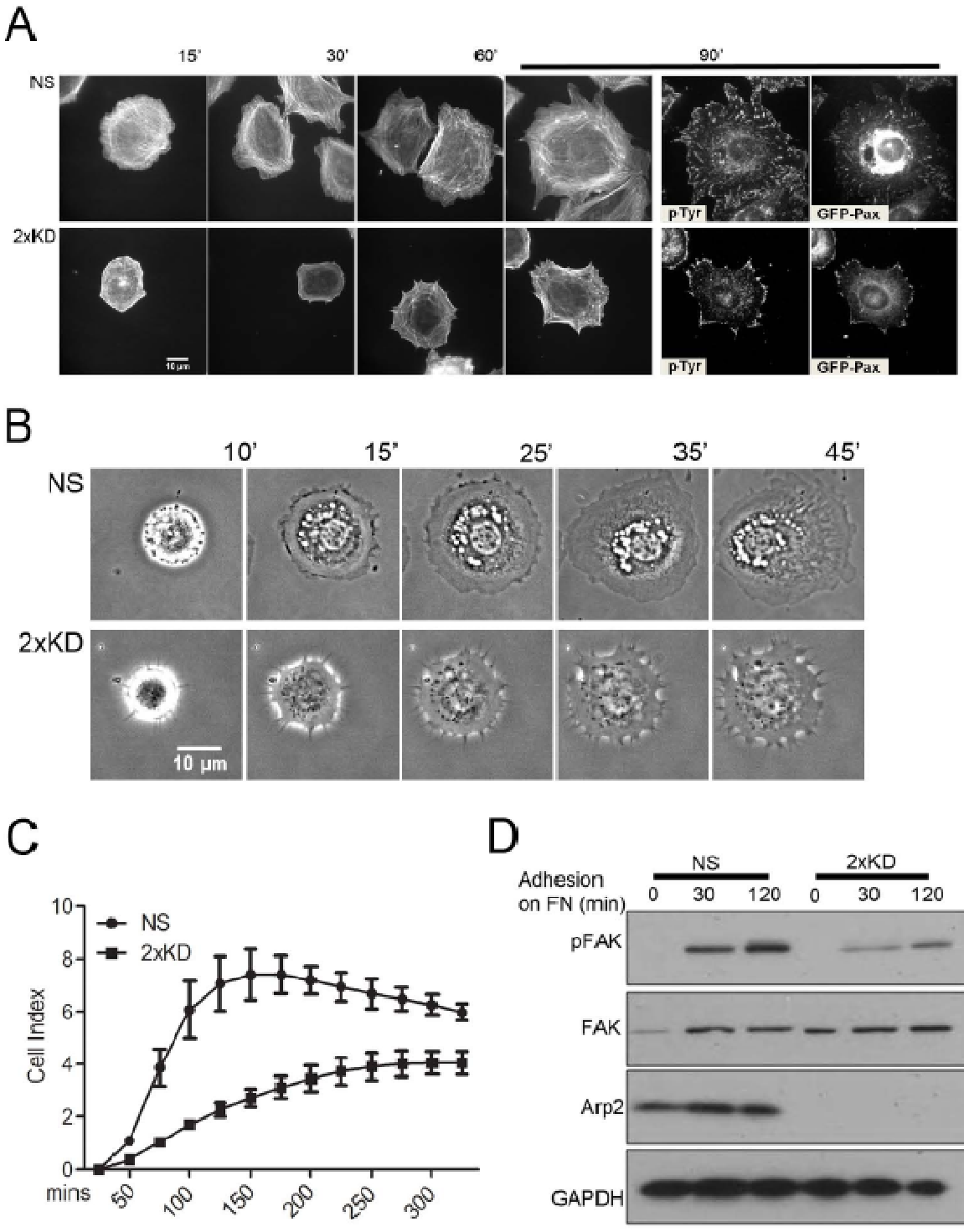
A
15'
30'
60'
90'
NS
2xKD
p-Tyr
GFP-Pax
p-Tyr
GFP-Pax
B
10'
15'
25'
35'
45'
NS
2xKD
10 µm
C
Cell Index
NS
2xKD
mins
0
2
4
6
8
10
50
100
150
200
250
300
D
Adhesion on FN (min)
NS
2xKD
0
30
120
0
30
120
pFAK
FAK
Arp2
GAPDH

Figure 13 Arp2/3 depletion inhibits cell spreading

A) NS and 2xKD cells expressing GFP-Pax were immunostained for phospho-tyrosin (pTyr) and F-actin at different time points during cell spreading

B) Time-lapse images showing the spreading of NS and 2xKD cells

C) Cell adhesion and spreading kinetics of NS and 2xKD cells were analyzed using an impedance based system and reported as arbitrary units (Cell Index). Error bars: SEM

D) Western blotting showing the change of phosphorylated FAK (pFAK) level upon cell adhesion to fibronectin. Cells were serum-starved overnight and trypsinized and plated on fibronectin-coated surface. Lysates were blotted for pFAK, total FAK, Arp2 and GAPDH as control

Arp2/3 and lamellipodia are essential for responding to absolute or gradient changes in ECM concentration

Although spreading provides useful information about the initial formation of cell-matrix adhesions, changes in the motility of fully spread cells in response to changes in matrix concentration are more physiologically relevant. Many investigators have noted that cells display a biphasic motility response when plated on different concentrations of ECM with optimal motility occurring at intermediate concentrations [62, 63]. We tested the role of Arp2/3 and lamellipodia in this biphasic motility response. As expected, when plated on different concentrations of FN, NS cells displayed a biphasic motility response. However, 2xKD cells migrated at a constant, slow speed on all FN concentrations tested (Figure 14A). This result was confirmed with Rat2 fibroblasts treated with the Arp2/3 inhibitor CK-666 (Figure 14B). This loss of biphasic motility response led us to explore the role of Arp2/3 complex and lamellipodia in haptotaxis. These results reveal an essential role of Arp2/3 complex and lamellipodia in responding to changes in the absolute concentration of ECM.

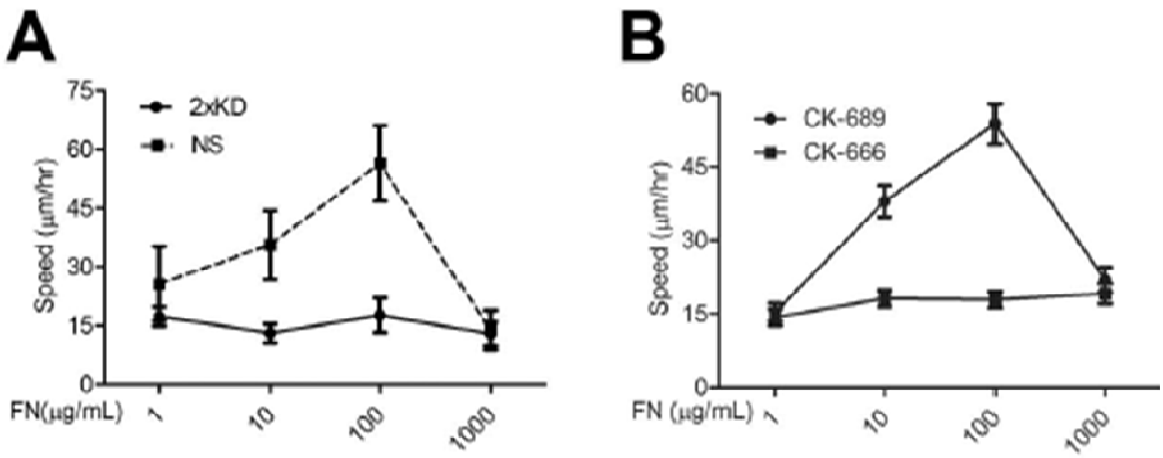

Figure 14 Arp2/3 complex depleted cells do not show biphasic response to changing ECM

A) Single-cell speed of NS and 2xKD cells plated on different concentrations of fibronectin was plotted (N>30). Error bars represent 95% confidence intervals

B) Speeds of Rat2 cells treated with CK-666 or CK-689 and plated on different concentrations of FN were plotted (N>30). Error bars represent 95% confidence intervals

The same microfluidic device used in the chemotaxis experiments can be utilized to establish a linear ECM gradient bound to the surface of the cell culture chamber prior to plating the cells (Figure 15A). The chamber was thoroughly flushed with PBS prior to plating the cells, ensuring that no soluble fibronection remained that could act as a chemoattractant. NS and 2xKD cells were plated in the same device exposing to the same condition for live cell imaging during haptotaxis as in the chemotaxis experiments. We quantified cell directionality in haptotaxis by ploting endpoint positions and angular turn per step based on cell tracking data. Both measurements showed a dramatic difference between NS and 2xKD cells (Figure 15B, C). In contrast with a robust haptotactic response of NS cells plated in the same chamber, haptotactic FMI and CP of 2xKD cells showed that these cells have no directional response to concentration gradients of FN. This result was the same with all source concentrations of FN tested (Figure 15D). We also confirmed this result with Rat2 fibroblasts treated with the Arp2/3 inhibitor CK-666 and observed decrease capability in haptotaxis when Arp2/3 activity is absent (Figure 15E). Finally, we tested other ECM proteins (laminin (LN) and vitronectin (VTN)) In addition to FN. These two matrix utilize different integrin receptors and we observed that 2xKD cells show complete absence of haptotaxis on all ECMs tested (Figure 15F). Together, these results reveal an essential role of Arp2/3 complex and lamellipodia in responding to changes in gradient presentation of ECM.

A

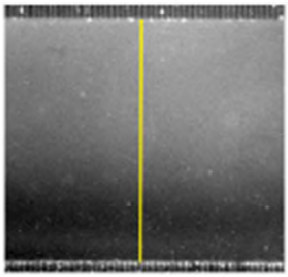

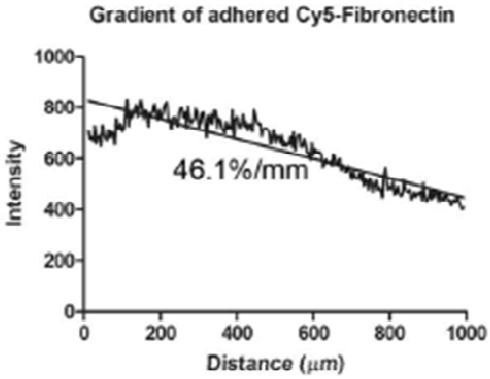

B

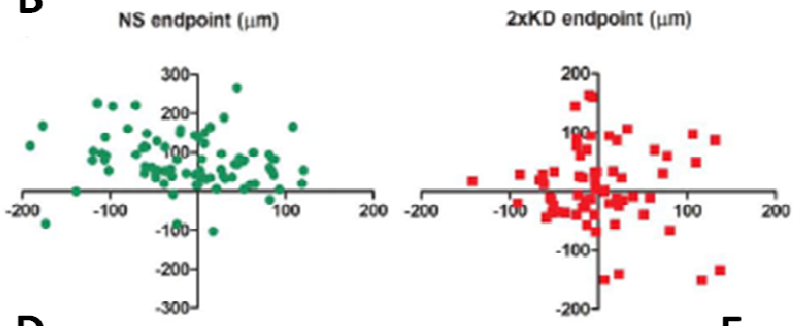

C

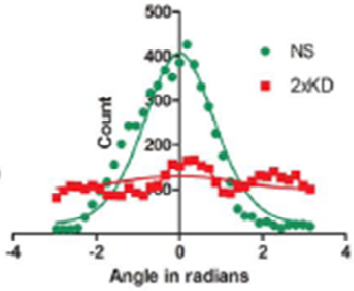

D

		100 μg/mL FN	250 μg/mL FN	500 μg/mL FN
NS	CP	0.67 (0.57,0.78)	1.3 (1.11,1.50)	1.00 (0.86,1.15)
	FMI	0.16 (0.06,0.26)	0.38 (0.32,0.44)	0.23 (0.14,0.31)
	V (μm/hr)	15.20 (14.24,16.16)	22.56 (21.11,24.01)	14.91 (14.09,15.73)
	N	50	100	60
2xKD	CP	0.14 (0.07,0.21)	-0.04 (-0.11,0.04)	0.02 (-0.09,0.13)
	FMI	0.03 (-0.04,0.11)	0.0006 (-0.08,0.08)	0.02 (-0.08,0.12)
	V (μm/hr)	21.59 (20.36,22.82)	17.88 (15.53,20.23)	17.24 (16.21,18.27)
	N	53	85	57

E

Rat2 +CK-689	CP	1.23 (0.96,1.52)
	FMI	0.30 (0.25,0.36)
	V (μm/hr)	23.46 (21.3,25.62)
	N	109
Rat2 +CK-666	CP	0.15 (0.02,0.27)
	FMI	-0.01 (-0.05,0.03)
	V (μm/hr)	20.0 (18.23,21.73)
	N	121

F

		250 μg/mL FN	500μg/mL LN	100 μg/mL VTN
NS	CP	1.3 (1.11,1.50)	1.63 (1.43,1.83)	1.00 (0.71,1.3)
	FMI	0.38 (0.32,0.44)	0.26 (0.21,0.30)	0.30 (0.23,0.38)
	V (μm/hr)	22.56 (21.11,24.01)	22.85 (21.43,24.3)	21.36 (19.82,22.91)
	N	100	84	46
2xKD	CP	-0.04 (-0.11,0.04)	0.15 (-0.02,0.31)	-0.09 (-0.18,0.001)
	FMI	0.0006 (-0.08,0.08)	0.01 (-0.04,0.07)	-0.04 (-0.13,0.05)
	V (μm/hr)	17.88 (15.53,20.23)	15.95 (14.9,17.9)	15.56 (14.48,16.64)
	N	85	54	43

Figure 15 Arp2/3-depleted cells cannot respond to gradient changes in extracellular matrix

A) Left: fluorescent image of Cy5-fibronectin gradient formed on the glass surface inside the cell culture chamber. Right: line-scan plot of the gradient along the yellow line depicted in the left panel

B) Representative end point scatter plots of NS and 2xKD cells in haptotaxis assays (250 μg/mL source fibronectin concentration)

C) Representative histogram showing angular turn per step of NS and 2xKD cells in the same haptotaxis assays

D) Table showing compass parameter (CP), forward migration index (FMI), velocity (V) and number of cells analyzed (N) in haptotaxis assays with indicated FN source concentrations. Numbers in parentheses for each entry are 95% confidence intervals

E) Table showing compass parameter (CP), forward migration index (FMI), velocity (V) and number of cells analyzed (N) in Rat2 cell haptotaxis assays with 250 μg/mL source fibronectin concentration and treated with CK-666 or CK-689

F) Table showing compass parameter (CP), forward migration index (FMI), velocity (V) and number of cells analyzed (N) in haptotaxis assays with indicated extracellular matrix

Depletion of Arp2/3 complex leads to altered focal adhesion morphology and dynamics

Our observation that 2xKD cells have defects in sensing and/or responding to changes in ECM suggests that cell-matrix interactions may be changed when Arp2/3 complex and lamellipodia are absent. To test this hypothesis, we compared the distribution of focal adhesion proteins by immunofluorescence staining. Endogenous Paxillin (Pax), Vinculin (Vin) and FAK were all present at clearly recognizable focal adhesions in 2xKD cells (red asterisks, Figure 16A). We also notice that there were no obvious nascent adhesions (focal complexes) in 2xKD cells due to the lack of lamellipodia. In order to visualize the dynamics of focal adhesions, GFP tagged Paxilin (GFP-Pax) was expressed in NS and 2xKD cells. We observed that both cell types contained GFP-Pax positive focal adhesions by TIRF microscopy. However, higher time resolution movies revealed that these two cell types tended to form adhesions in qualitatively different ways. Consistent with previous observations from other cell types, the NS cells generated small focal complexes at the distal margin of lamellipodia, a subset of which matured into focal adhesions at the rear of lamellipodia. However, in the 2xKD cells, the focal adhesions first appeared at the base of filopodia and reached maximal intensity quite rapidly (within 1-2 min, Figure 16B). These adhesions matured in the proximal to distal direction (Figure 16C). These qualitative differences in the formation of focal adhesions suggested that cells depleted of Arp2/3 complex were utilizing alternative pathways of adhesion assembly.

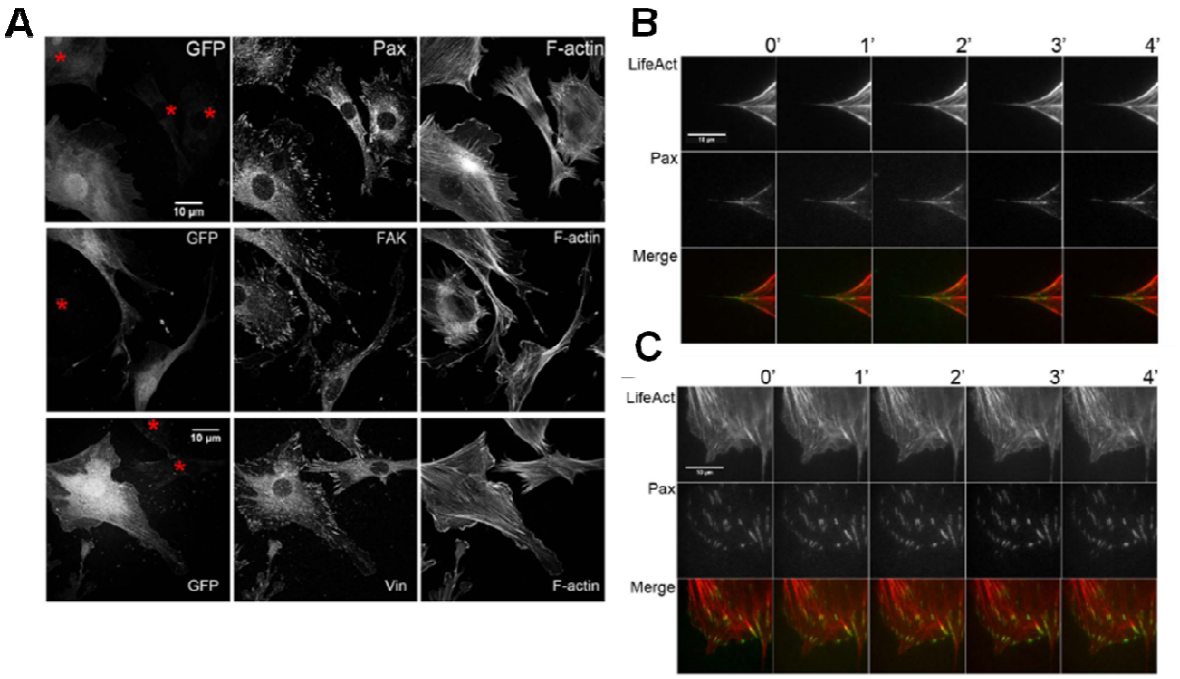

Figure 16 Depletion of Arp2/3 complex leads to defective focal adhesion morphology and dynamics

A) Mixed NS (expressing GFP) and 2xKD cells (marked by red asterisks) were immunostained for endogenous paxillin (Pax), focal adhesion kinase (FAK), vinculin (Vin) and F-actin (Scale bar: 10 µm).

B) Representative time-lapse TIRF images of an NS cell expressing GFP-Pax and LifeAct-tagRFP

C) Representative time-lapse TIRF images of a 2xKD cell expressing GFP-Pax and LifeAct-tagRFP

Recently, an automated method to detect and quantify the parameters of the individual focal adhesions was developed in the Gomez group at UNC (Figure 17A-D) [64]. To better understand the difference in focal adhesion properties between control and Arp2/3-depleted cells, we used this method to segment and track every focal adhesion in an unbiased manner.

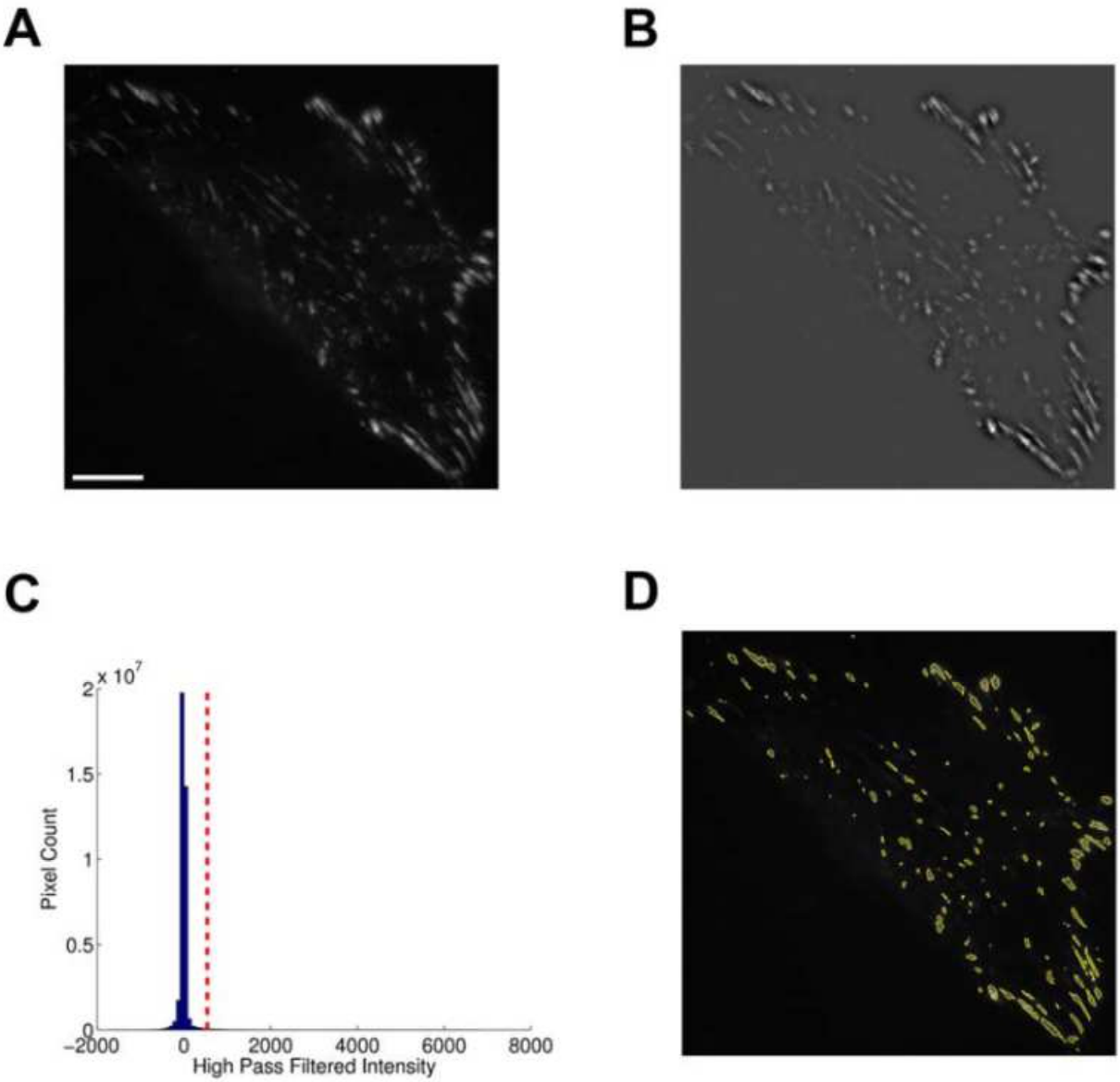
A
B
C
D
x 10^7
2
1.5
1
0.5
0
Pixel Count
−2000
0
2000
4000
6000
8000
High Pass Filtered Intensity

Figure 17 An automated method to detect and analyze focal adhesion properties

A) TIRF image of an NS cell expressing GFP-Paxillin on a 100 μg/mL FN coated surface (bar = 10μm).

B) High-pass filter applied to the image in A.

C) Distribution of high-pass pixel intensities from the entire time-lapse image series in A. The red dotted line indicates the focal adhesion pixel rejection threshold of the mean plus two standard deviations.

D) Locations of focal adhesions as determined by applying the threshold determined in C to the high-pass filtered image in B and overlaying the result on the image in A. Each identified adhesion is outlined in yellow.

We compared the focal adhesion properties of NS and 2xKD cells across three concentrations of fibronectin (Figure 18) and found some interesting trends. With increasing fibronectin concentration, mean focal adhesion area and mean longevity were increased in the NS cells. Interestingly, neither of these properties varies significantly in the 2xKD cells with changes in fibronectin concentration. Mean long axis length and mean axial ratio are the same in both cell types and do not vary with fibronectin concentration. The number of adhesions per cell (per 10 min) decreases in NS while increases in 2xKD cells as a function of fibronectin concentration.

To confirm these changes were due to loss of Arp2/3 activity, we also examined the focal adhesions in Rat2 fibroblasts expressing GFP-Pax treated with the Arp2/3 inhibitor CK-666 or its inactive analogue CK-689. With transient Arp2/3 inhibition, some of the same trends in focal adhesion properties were evident and statistically significant, but were not as dramatic as in the RNAi-based depletion. Together these data suggest that some focal adhesion properties are changed when Arp2/3 is depleted, while others remain the same in the absence of Arp2/3.

		Mean Area (μm^2)	Mean Axial Ratio	Mean Major Axis (µm)	Mean Minor Axis (µm)	Mean Longevity (min)	Adhesions/Cell/10 min	# Adhesions	# Cells
NS	1 µg/mL FN	0.057±0.00031	2.0±0.0015	0.4±0.0007	0.2±0.0004	4.4±0.03	728.0±193.0	169735	25
	10 µg/mL FN	0.065±0.00081	2.0±0.0022	0.4±0.0013	0.2±0.0007	4.9±0.05	431.5±124.0	80552	16
	100 µg/mL FN	0.082±0.00107	1.9±0.0034	0.4±0.0020	0.2±0.0010	6.1±0.09	262.6±79.3	49154	17
2xKD	1 µg/mL FN	0.054±0.00037	2.0±0.0023	0.4±0.0008	0.2±0.0005	4.5±0.04	286.6±95.9	77917	21
	10 µg/mL FN	0.056±0.00049	2.0±0.0026	0.4±0.0010	0.2±0.0006	4.6±0.04	324.6±152.1	63260	15
	100 µg/mL FN	0.053±0.00019	2.0±0.0012	0.4±0.0004	0.2±0.0003	4.4±0.02	802.5±161.7	254105	22
Rat2	CK-689	0.057±0.00053	1.9±0.0031	0.4±0.0012	0.2±0.0007	4.7±0.07	303.1±124.1	42576	12
	CK-666	0.054±0.00048	1.9±0.0021	0.4±0.0008	0.2±0.0005	4.4±0.04	305.0±147.5	77942	20

Figure 18 Difference in focal adhesion properties between control and Arp2/3-depleted/inhibited cells

Table of focal adhesion parameters: NS vs 2xKD plated on 1, 10 and 100 µg/mL FN; Rat2 fibroblasts treated with CK-666 or CK-689 on 100 µg/mL FN. Numbers after the +/- indicate 95% confidence intervals as determined by a t-distribution fit

Lamellipodia promote global focal adhesion alignment

Although the characterization and comparison of individual focal adhesion properties is important, the ensemble pattern of adhesions is the most relevant parameter to whole cell behavior, especially cell migration. How cells control these global parameters of focal adhesions is poorly understood. We observed different focal adhesion patterns in 2xKD and NS cells during spreading and after cells had fully spread. NS cells had focal adhesions more aligned to each other while 2xKD cells had adhesions that were more radially arrayed. To quantify global focal adhesion alignment, we developed a method to measure the deviation of adhesion angles from the most frequent or dominant angle observed in the whole cell (Figure 19). By plotting the angles of all the adhesions that met this criterion, we were able to determine the most frequent or dominant focal adhesion angle by rotating the image frame of reference until the standard deviation (SD) was minimized and the peak of the distribution of angles moved close to zero (Figure 19B).

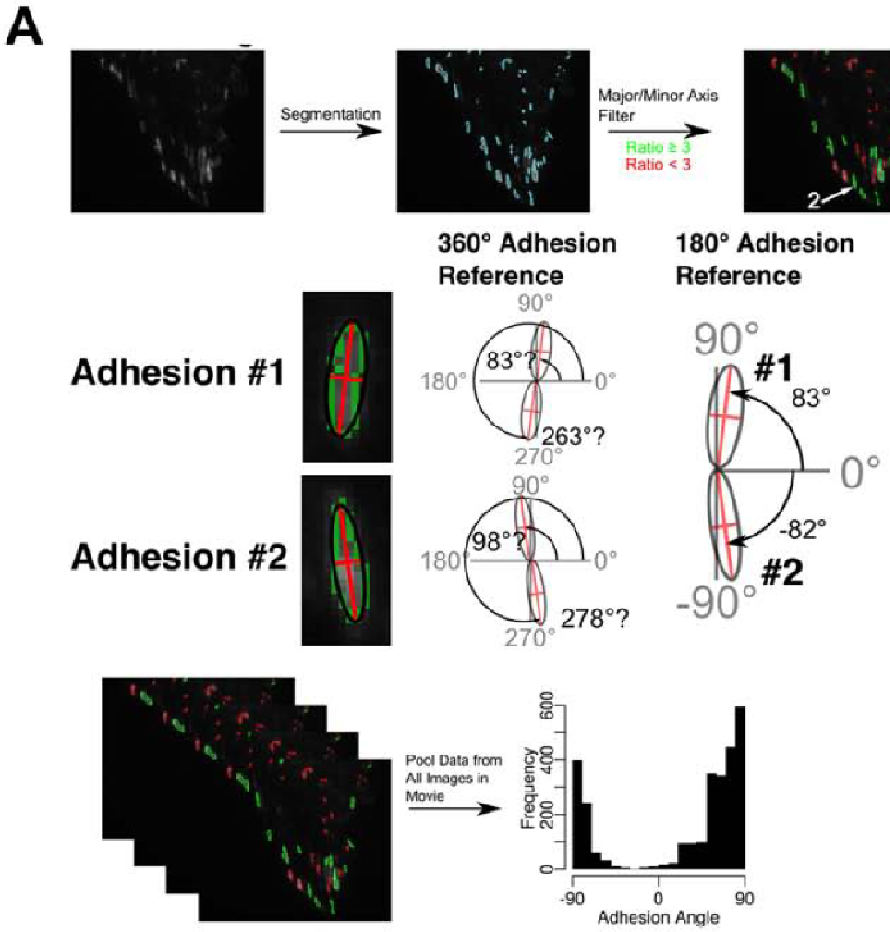
A
Segmentation
Major/Minor Axis Filter
Ratio ≥ 3
Ratio < 3
1
2
360° Adhesion Reference
180° Adhesion Reference
Adhesion #1
Adhesion #2
90°
180°
0°
270°
83°?
263°?
98°?
278°?
#1
#2
83°
-82°
-90°
Pool Data from All Images in Movie
Frequency
Adhesion Angle
B
Reference 0°
Reference 45°
Reference 90°
Reference 135°
FAAI=90-SD
FAAI= 23.7
FAAI= 64.7
FAAI= 65.3
FAAI= 47.1
Alignment Index
Dominant FA Alignment = 74.9°
FA Alignment Index = 65.5
Alignment Angles (degrees)

Figure 19 Determination of focal adhesion alignment index (FAAI)

A) Focal adhesions were segmented via the method described previously and filtered to exclude adhesions with a major to minor axis ratio of less than three as indicated by color coding. The angle of the major axis with the positive x-axis was measured and the adhesions angles throughout the time-lapse image set pooled.

B) Sample search through the potential reference angles to determine the FAAI.

One possible way adhesions could become aligned to each other is through rotation of their long axis. Although our visual impression from TIRF movies of cells expressing GFP-Pax strongly argued against this possibility, we tested this by plotting the average deviation in long-axis angle during the time that an individual adhesion was observed. Consistent with our visual impression, focal adhesions show very little variation in their long-axis angle over time in either cell type (Figure 20A). Thus, any change in global alignment must arise from spatially coherent formation, rather than post-formation realignment. In order to reliably determine the angle of the individual adhesions, we limited our measurements to those adhesions with a length/width ratio of at least 3 (Figure 20B).

The dominant focal adhesion angle was simply the degree to which the image had to be rotated to center the peak over zero. The Focal Adhesion Alignment Index (FAAI) is directly related to the standard deviation of this distribution; FAAI = 90-SD in order to have a higher index value correspond to more aligned adhesions (Figure 20C). To illustrate this measurement, a cell with high FAAI and low FAAI are shown in Figure 20D.

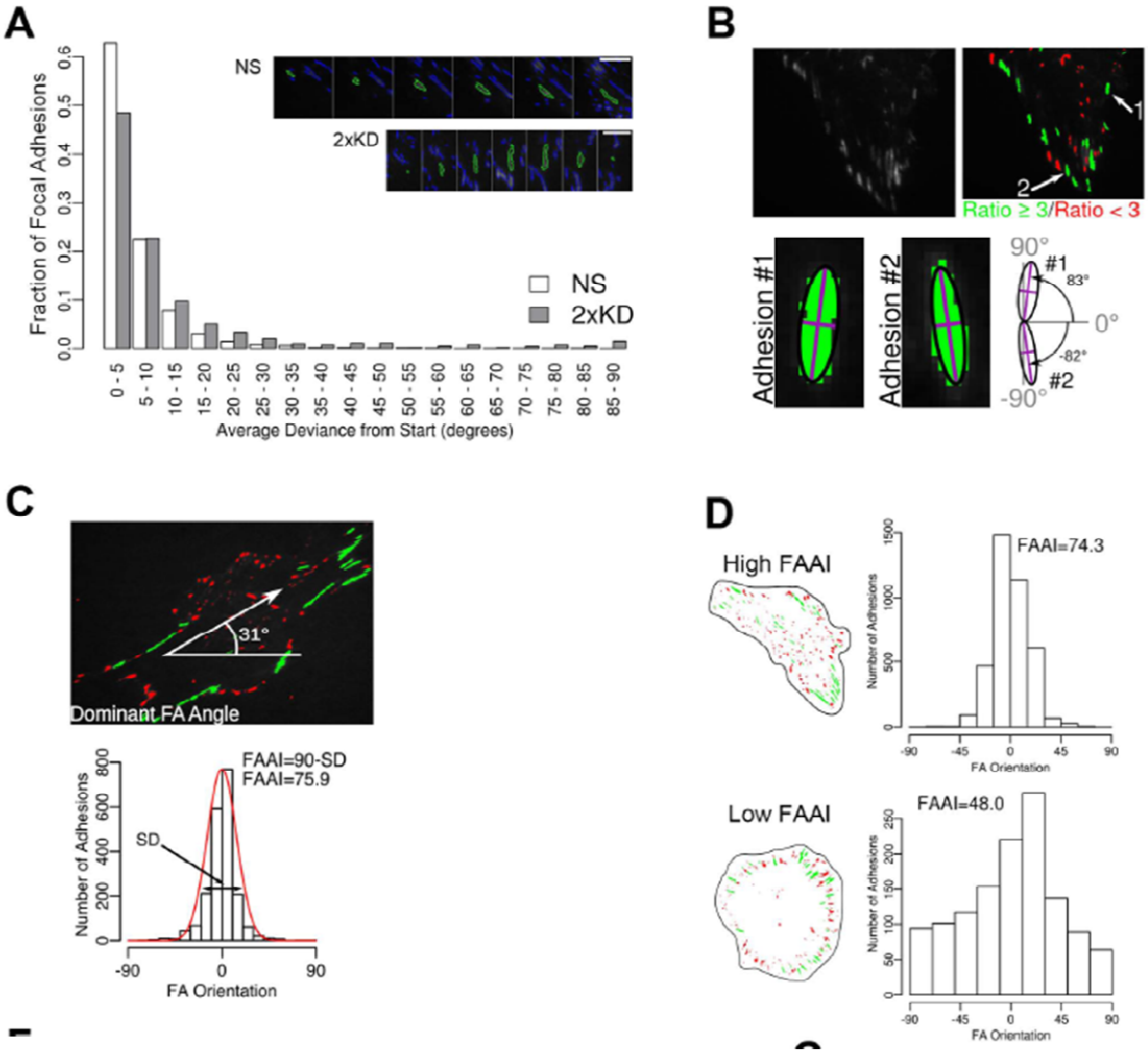
A
NS
2xKD
Fraction of Focal Adhesions
0.0
0.1
0.2
0.3
0.4
0.5
0.6
NS
2xKD
0 - 5
5 - 10
10 - 15
15 - 20
20 - 25
25 - 30
30 - 35
35 - 40
40 - 45
45 - 50
50 - 55
55 - 60
60 - 65
65 - 70
70 - 75
75 - 80
80 - 85
85 - 90
Average Deviance from Start (degrees)
B
1
2
Ratio ≥ 3/Ratio < 3
Adhesion #1
Adhesion #2
90°
#1
83°
0°
-82°
#2
-90°
C
31°
Dominant FA Angle
FAAI=90-SD
FAAI=75.9
SD
Number of Adhesions
0
200
400
600
800
-90
0
90
FA Orientation
D
High FAAI
FAAI=74.3
Number of Adhesions
0
500
1000
1500
-90
-45
0
45
90
FA Orientation
Low FAAI
FAAI=48.0
Number of Adhesions
0
50
100
150
200
250
-90
-45
0
45
90
FA Orientation

Figure 20: Focal adhesion orientation with time and segmentation method for FAAI detection

A) Distribution of single focal adhesion mean deviations from their first orientation measurement starting point. The adhesions analyzed were from NS (17 cells and 3184 adhesions) or 2xKD (22 cells and 1132 adhesions) cells plated on 100 µg/mL fibronectin. Insets show single adhesions outlined in green through time, 6 min between images

B) Diagram showing adhesion filtering through a minimum axial ratio of 3 and two sample adhesion orientations

C) Diagram showing the determination of dominant angle and focal adhesion alignment index (FAAI)

D) Sample single cell cartoons showing representative high and low FAAI cells with corresponding adhesion orientation data sets

Using this metric, we quantified the FAAI of NS and 2xKD cells plated on 1, 10 and 100 µg/mL fibronectin. We observed increased alignment of adhesions across the cell (increasing FAAI) with increasing fibronectin concentration in the NS cells, while the alignment in the 2xKD cells was decreased compared to the NS cells and was constant at all fibronectin concentrations (Figure 21A). Since mean adhesion area showed similar trends, we tested whether focal adhesion alignment was independent from adhesion area. To do this, we re-calculated the FAAI considering only small, medium or large adhesions in the NS and 2xKD cells (Figure 21B). Regardless of which size adhesions we used to calculate FAAI, the same difference in alignment was observed between NS and 2xKD cells. To ensure that this result was not specific to the expression of GFP-Pax, we calculated the FAAI of NS and 2xKD cells expressing fluorescent fusions of FAK and Vinculin. With all three markers, 2xKD cells showed significantly lower FAAI compared to NS control cells (Figure 21C). Finally, we confirmed this result in Rat2 fibroblasts treated with the Arp2/3 complex inhibitor CK-666 where we observed decreased FAAI with Arp2/3 inhibition (Figure 21D). These results suggest that one of the principal functions of the lamellipodium is to promote global focal adhesion alignment.

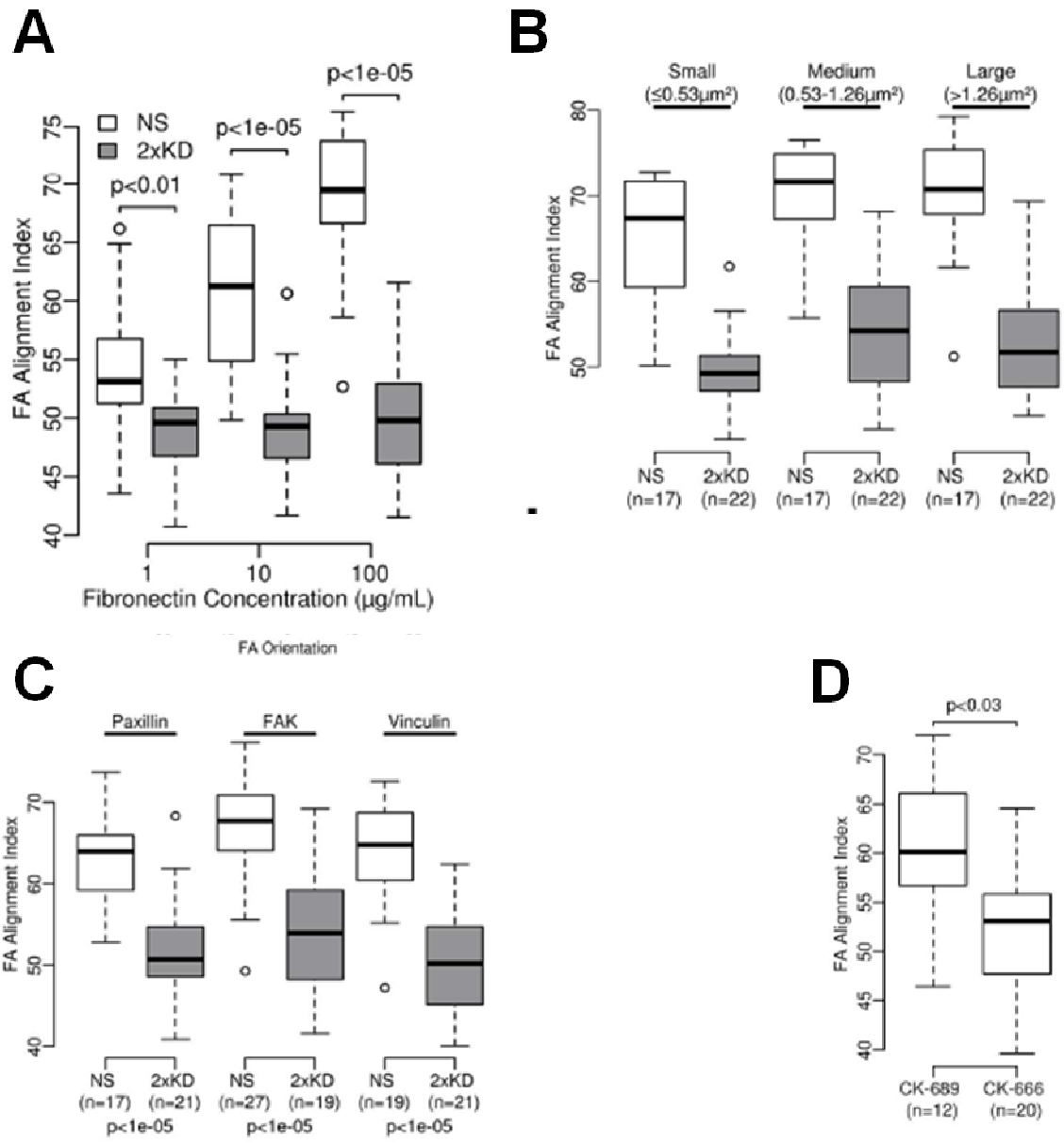
A
NS
2xKD
p<0.01
p<1e-05
p<1e-05
FA Alignment Index
Fibronectin Concentration (µg/mL)
FA Orientation
B
Small (≤0.53µm²)
Medium (0.53-1.26µm²)
Large (>1.26µm²)
FA Alignment Index
NS (n=17)
2xKD (n=22)
C
Paxillin
FAK
Vinculin
FA Alignment Index
NS (n=17)
2xKD (n=21)
NS (n=27)
2xKD (n=19)
NS (n=19)
2xKD (n=21)
p<1e-05
p<1e-05
p<1e-05
D
p<0.03
FA Alignment Index
CK-689 (n=12)
CK-666 (n=20)

Figure 21 Arp2/3 depletion leads to poor global alignment of focal adhesions

A) FAAI of NS and 2xKD cells expressing GFP-Paxillin plated on different concentrations of fibronectin (number of cells same as in Fig. 6D, p-values for the difference between the means were calculated by bootstrapping with 10000 replicates)

B) FAAI of NS and 2xKD cells with the adhesions grouped by size (p-values for each size range <0.0005)

C) FAAI of NS and 2xKD cells expressing indicated focal adhesion markers. (n = number of cells analyzed)

D) FAAI of Rat2 cells with CK-666 or CK-689

Discussion

In this work, we have established a stable Arp2/3-depleted cell line that allowed us to study random and directional cell motility in the absence of lamellipodia. The depletion of Arp2/3 complex causes striking changes in cell morphology, motility and global focal adhesion geometry. Furthermore our study also reveals the essential role of lamellipodia in fibroblast haptotaxis, but not chemotaxis.

Establishment of a stable Arp2/3 depleted cell line

It is widely believed that Arp2/3 complex is required for viability in eukaryotic organisms; however our data suggest that this is not strictly true in mammalian cells in culture. It is worth considering why we were able to recover stable cell lines depleted of >98% of Arp2/3 complex. First, we quickly separated the cells as clones after they were infected with the shRNA-expressing lentiviruses through the use of fluorescent protein reporters rather than relying on drug resistance. Any selective growth advantage conferred by less than full knockdown is cancelled out under these circumstances. Although we initially had some concerns about using clones, these were put to rest by the microinjection rescue experiment that indicated that these cells were still capable of making lamellipodia within minutes of the re-introduction of the Arp2/3 complex. Second, we depleted two essential subunits (p34Arc and Arp2) to create a “fail-safe” condition where loss of either shRNA conferred no advantage due to the continued absence of another essential subunit. Third, the complexity of mammalian cells may have been working in our favor. Simpler eukaryotes may be strictly dependent on Arp2/3 activity for viability-

associated processes such as nutrient uptake, while mammalian cells have a multitude of partially redundant pathways. Finally, we performed these experiments in the *Ink4a/Arf*-deficient background. These genes are well known as tumor suppressors that arrest cell growth upon oncogenic insult [65]. Our results indicate that cells harboring an intact Arf gene are much more sensitive to the loss of Arp2/3 complex, suggesting that the deranged actin cytoskeleton resulting from the loss of Arp2/3 activity may trigger an Arf-dependent growth arrest pathway.

The relationship between Arp2/3 complex and lamellipodia

The most striking morphological change we observed in the Arp2/3 complex depleted cells was the disappearance of lamellipodia. We report several lines of evidence to support the idea that the phenotypic loss of lamellipodia is due to a specific loss of Arp2/3 complex activity. Both shRNAs used to deplete p34Arc and Arp2 respectively could be fully rescued by co-expression of RNAi-resistant versions of these genes. Pharmacological inhibition of Arp2/3 complex by CK-666 produced a similar, although slightly milder phenotype as the double depletion of p34Arc and Arp2. Importantly, this compound had no further effect on the 2xKD cells, indicating that any residual Arp2/3 activity was not contributing to the residual motility. Furthermore, lamellipodia could be recovered in the 2xKD cells within minutes of microinjection of bovine Arp2/3 complex. Therefore, the 2xKD cells are not only useful in the study of Arp2/3 complex dependent functions, but also serve as useful tools to dissect the functional role of lamellipodia in cell motility.

Previous studies have shown that the actin networks within lamellipodia contain short, branched filaments nucleated by Arp2/3 complex [47], consistent with observations of networks generated with purified Arp2/3 complex and actin [66]. Recently, this model has been called into question based on an alternate electron microscopy protocol [54]. Using this technique, mostly long actin filaments were observed in the lamellipodia. Our results with the cryo-shadowing technique are entirely consistent with the notion of highly branched networks of short actin filaments in lamellipodia as originally observed by platinum replica EM [47]. Further evidence for the role of Arp2/3 complex in branch generation comes from the apparent lack of these structures in cells with near total depletion of Arp2/3 complex.

In the absence of branched actin generated by the Arp2/3 complex, more filopodial protrusions form on the periphery of cells. 2xKD cells engage in a form of filopodia-dependent cell motility, in which new flat cell surface area is created by “filling the gap” between adjacent filopodia. The filopodia of 2xKD cells protrude and bend until they become anchored to the underlying matrix, at which time the membrane between two filopodia gradually fills-in. When myosin II was inhibited in the 2xKD cells using blebbistatin, we observed increased filopodia number and “filling the gap” behavior, and a proportional increase in cell speed. This suggests that the Arp2/3 depleted cells rely on this filopodia-initiated “filling the gap” motility to migrate. This form of motility is relatively inefficient compared to motility using lamellipodia; however, efficiency of motility does not necessarily relate to the ability of cells to sense or respond to directional cues.

The role of lamellipodia in chemotaxis

Chemotaxis is required for numerous physiological processes and has been the subject of intense study for well over a century. The most successful model systems have been the social amoeba *Dictyostelium* and amoeboid cells of the haematopoietic system such as neutrophils [44].

Studies of chemotaxis in amoeboid cells and other cell types have largely focused on the signal transduction cascades that connect cell surface receptors to the polymerization of actin at the protrusive leading edge. As lamellipodia are the actin-rich, protrusive organelle in fibroblasts, we fully anticipated that depletion of Arp2/3 complex and the resulting loss of lamellipodia would have a profound impact on fibroblast chemotaxis. To our surprise, depletion of Arp2/3 complex has no effect whatsoever on fibroblast chemotaxis up shallow gradients of PDGF, other than affecting the speed at which the cells crawl. Although stimulated actin assembly may still be important for chemotactic response, this assembly clearly does not involve the Arp2/3 complex in this cell type. However, other forms of actin assembly such as those that lead to the increased filopodia on the 2xKD cells may be important for chemotaxis. It is also worth noting that our results may not translate to amoeboid cell chemotaxis, which may require Arp2/3 activity. Future studies will focus on testing the role of alternate actin assembly pathways in fibroblast chemotaxis and testing the generality of our findings for other cell types.

Although the normal chemotaxis of Arp2/3-depleted fibroblasts is surprising, several studies point toward a more complex picture of chemotaxis than previously

appreciated. Transient depletion of either the Cdc42 or Rac1 small GTPase or both does not affect the ability of fibroblasts to respond to gradients of PDGF [67]. Similar to our cells, these depletions affect the morphology of the leading edge without affecting chemotaxis, although some non-GTPase dependent activation of Arp2/3 cannot be excluded. Another enzyme that was initially thought to be crucial for chemotaxis, PI-3 Kinase, is also not strictly required for chemotaxis of *Dictyostelium* amoebae based on genetic studies [68] or fibroblast chemotaxis towards PDGF based on pharmacological inhibition of this enzyme [69]. Together with our results, these studies highlight the complexity of chemotactic mechanisms and the insufficiency of current models in explaining this process.

The role of lamellipodia in sensing/responding to changes in ECM

Our results with the Arp2/3 depleted cells reveal the importance of Arp2/3 complex and lamellipodia in sensing and responding to the changes in the ECM. Several groups have reported that cells exhibit a biphasic motility response to variable extracellular matrix concentration with fast migration occurring at intermediate ECM concentration and slower migration occurring at low and high ECM concentrations [62, 63]. The molecular basis of this biphasic response is thought to involve spatiotemporal feedback between actomyosin and focal adhesion systems [63]; however, the relationship between this response and specific cellular architecture is unclear.

Our data indicate that Arp2/3 and lamellipodia are required for the biphasic response of cells to variable ECM. Stated another way, the adhesions formed by the

filopodial protrusions on the 2xKD cells are insufficient to allow cells to sense or respond to these differences in ECM concentration. This suggests that the adhesions formed within lamellipodia have qualitatively different properties that allow the whole cell to coordinate global motility.

Cells not only can regulate velocity when migrating on different concentrations of ECM, but also can sense and respond to ECM gradients and migrate in a directional way. This process, termed haptotaxis, requires cells to 1) sense differences of ECM concentration/engagment across a single cell, 2) polarize cytoskeletal and motility machinery, and 3) migrate up the gradient. Our data show that Arp2/3 depletion and subsequent loss of lamellipodia completely ablates haptotaxis. Importantly, this was true not only on gradients of fibronectin, but also on gradients of laminin or vitronectin, ECMs that require different integrin heterodimers.

One outstanding question about the role of lamellipodia in haptotaxis is whether this structure is involved in sensing the gradient or responding to the gradient or both. Considering the intact PDGF chemotactic response without Arp2/3 complex, the loss of haptotaxis appears to be a specific effect rather than a general defect in direction sensing. This remarkable difference in the need for lamellipodia between chemotaxis and haptotaxis suggests that cells use very different mechanisms to sense and respond to these different directional cues.

Spatial organization of cell-matrix adhesions and global cell motility

Although focal adhesions have been intensively studied for decades, the processes that spatially organize these structures in an ensemble manner across

the whole cell are poorly understood. Our results indicate that lamellipodia play a major role in bringing spatial coherence to focal adhesion formation. Without lamellipodia, focal adhesions are poorly aligned to each other, which may explain why these cells migrate slowly.

An open question is how lamellipodia promote the alignment of focal adhesions. One possibility is that the retrograde flow of actin networks in lamellipodia, which is itself spatially coherent over 0.5-5 µm length scales, could promote the alignment of the adhesions that form and mature within this flow field. However, how the alignment of focal adhesions within lamellipodia contribute to global alignment is less clear. Since the rear of the cell was once the front the cell, this alignment may reflect the history of these adhesions as born within previous lamellipodia. How cells manage to define a new axis of focal adhesion alignment upon turning will be the subject of future studies.

Our observations also provide a conceptual framework for linking events occurring at small length scales such as the formation of branches by the Arp2/3 complex (~10 nm) to whole cell motility at much longer length scales (~100 µm) (Figure 22). Branched actin networks generated by the Arp2/3 complex are the main component of the lamellipodial cytoskeleton.

As we have shown in this paper, lamellipodia are critical for the alignment of focal adhesions. Cells with aligned focal adhesions will have aligned stress fibers attached to those adhesions. Since stress fibers are the main contractile structure of fibroblasts, cells with aligned focal adhesions will have more coherent contractility.

We postulate that this coherent contractility will contribute directly to efficient whole cell migration. This overall notion is consistent with our observation that a strong relationship exists between the fibronectin concentration the cells are plated on, the global alignment of focal adhesions, and their increased cell speed. Future studies will focus on testing this hypothesis in context of other 2D and 3D motility events.

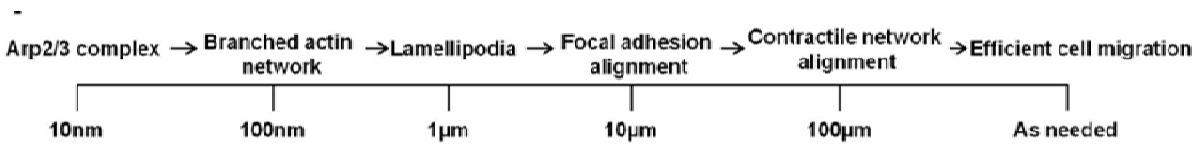

Figure 22 Conceptual model of cell motility events across length scales

Materials and methods

Reagents and Materials: Commercial antibodies were obtained from Cell Signaling Technologies (Akt (pan), Phosphor-Akt(Ser473), ECM Bioscience (Arp2(C-terminal region)), Sigma-Aldrich (Monoclonal anti-vinculin Clone hVIN-1, Monoclonal anti-ARP3, CloneFMS338), Upstate Biotechnology (Anti-FAK clone 4.47, Rabbit (Polyclonal) Anti-FAK[pY397]), BD Biosciences (Mouse anti-Paxillin), Millipore(Anti-p34-Arc/ARPC2), and Ambion Applied Biosystems (Anti-GAPDH). AlexaFluor647 dye conjugated phalloidin was from Invitrogen. Arp2/3 complex inhibitor CK-666 and the inactive control CK-689 are from EMD4Biosciences. Latrunculin B, (-)-Blebbistatin, Laminin were from Sigma-Aldrich, human plasma Fibronectin from BD Biosciences, Human Vitronectin from R & D Systems, Cy5 labeling kit from Amersham, Rhodamine Red-X and HRP conjugated secondary antibodies were from Jackson ImmunoResearch Laboratories. Bovine Arp2/3 complex was from Cytoskeleton Inc. PLL(20)-g[3.5]-PEG(2) was from SuSoS (Dübendorf, Switzerland). Western blotting was done by standard techniques. For quantitative western analysis, the blot was probed using primary antibodies followed by incubation with infrared-conjugated secondary antibodies. The membrane was scanned in an Odyssey SA scanner (LI-COR Biosciences, Lincoln, NE), and band intensities were quantified using the Odyssey software. Molecular cloning was conducted using standard procedures and details including primer sequences are available upon request.

Cell culture, viral transduction and generation of 2xKD cells: Cells were cultured in DMEM supplemented with 10% FBS (HyClone), 100 U/mL penicillin, 100

μg/mL streptomycin and 292 μg/mL L-glutamine. DMEM supplemented with 0.1% fatty-acid free BSA (Equitech-Bio), 100 U/mL penicillin, 100 μg/mL streptomycin and 292 μg/mL L-glutamine was used to culture cells during serum starvation. Transient transfections were performed using FuGene 6 (Roche) for HEK293 FT cells. Retroviral packaging, infections, and fluorescence-activated cell sorting were as described[32]. Lentivirus production and infection were as described [7].

IA32 cells infected with shArp2-mChry (target sequence: TGACCATGGCTTTAAACA AGTT) and shp34-EGFP (from [8]) viruses were cloned by fluorescence-activated cell-sorting (FACS) and screened for p34 and Arp2 expressions by Western blot. Infection with adenoviruses expressing Cre-recombinase (U of Iowa Gene Transfer Core) was used to deplete fluorescent protein expression before a second round of FAC sorting to yield 2xKD cells.

Growth Curves: MEFs were plated at 1×10^4 cells/well as triplicates in 24 well plates. Cell number was counted every 24 hr for indicated days, and normalized to the number on the first day. Growth curve was measured the same way for IA32 NS and 2xKD cells, but with different initial cell number (3000 cells/well). Cell viability was determined by trypan blue exclusion.

Microinjection Rescue of 2xKD cells: Bovine Arp2/3 protein complex was reconstituted with distilled water to 5 mg/mL in the following buffer: 20 mM Tris pH 7.5, 25 mM KCl, 1 mM $MgCl_2$, 0.5 mM EDTA, 0.1 mM ATP, 0.2% dextran and 2% sucrose. To confirm successful microinjection, rhodamine-dextran was co-loaded with the Arp2/3 complex. Microinjection of Arp2/3 complex was performed with a

semiautomatic Eppendorf InjectMan NI 2/Femtojet system. Injected volume was estimated to be less than 10% total cell volume.

Spreading assay: Cell spreading assays were performed as described previously [70] with minor modifications. Briefly, NS and 2xKD cells were serum starved for 1 hr. Cells were then detached with trypsin containing 1 mM EDTA, washed with regular cell culture medium, and then suspended at 1×10^4 cells/mL. Cells were seeded at 1000 cells/well in the electrode sensors (16X E-plate 16, Roche) coated with 25 µg/mL FN. Cell adhesion during the subsequent 5 hr period was continually monitored by taking a measurement with the RTCA apparatus (Roche Applied Science) operated with RTCA Software every 30 sec.

Phase contrast microscopy of cell spreading: Cells were trypsinized, resuspended in complete culture medium. Phase contrast time-lapse sequential cell images were captured with Nikon BioStation IM.

Light Microscopy and image analysis

Immunofluorescence: For immunofluorescent staining, the cells were fixed, stained and mounted as described previously [33]. Cells were plated on acid-washed coverslips coated with 10 µg/mL FN overnight before fixing with 4% PFA and permeabilized in 0.1% Triton X-100 in PBS for 5 min. Cells were then blocked for 15 min in PBS containing 5% normal goat serum (Jackson Laboratories) and 5% fatty-acid-free BSA. Primary antibodies were applied to cells in PBS containing 1% BSA for 1 hr at room temperature. Cells were stained in various combinations with

AlexaFluor-647 phalloidin for F-actin (1:200 dilution), p34Arc (1:250 dilution), Pax (1:500 dilution), Vin (1:400 dilution) or FAK (1:400 dilution) antibodies. After washing the cells three times in PBS, fluorescent dye conjugated secondary antibodies were diluted to 1:250 in 1% BSA in PBS and applied to the coverslips for 1 hr. After three washes in PBS, the coverslips were mounted onto slides with Fluoromount G (Electron Microscopy Sciences).

Images were captured using a FluoView FV1000 scanning confocal inverted microscope (FV1000, Olympus) equipped with a 1.42 N.A. 60× objective, a Hamamatsu PMT and controlled by Fluoview software. Maximum intensity projection was generated with ImageJ (ZProject-Maximum intensity function) from a z-stack (4 slices, 100 nm interval). Images were combined and annotated in Photoshop for presentation. Images were initially saved as 16-bit tiff files and converted to 8-bit tiff files in ImageJ during the analysis.

Single cell tracking: Cells were plated on 10 μg/mL FN-coated glass bottom culture dishes (MatTek Corporation) for 8-12 hr before imaging. Time-lapse microscopy was performed on an Olympus VivaView FL incubator fluorescent microscope (20x objective) with a Hamamatsu camera (OrcaERAG - c4742-80-12AG), or with Nikon BioStation IM (20x objective). Cell speed was measured with ImageJ using the Manual Tracking plug-in (http://rsbweb.nih.gov/ij/plugins/track/track.html).

In ECM biphasic response experiments, glass bottom culture dishes (MatTek Corporation) dishes were first coated with indicated concentrations of FN at 37 ℃ for 1 hr and thoroughly washed with distilled water. Coated dishes were then

blocked with 1 mg/mL PLL(20)-g[3.5]-PEG(2) at 37 ℃ for 1 hr to prevent non-specific cell adhesion.

Focal adhesion imaging: IA32 cells infected with shNS-GFP-PAX, shNS-Vin-GFP, mChry-FAK, 2xKD cells infected with shArp2-GFP-PAX, shArp2-Vin-GFP, mChry-FAK, and Rat2 cells treated with CK-666 or CK-689 were plated on FN coated Delta T dishes (Bioptechs). Total internal reflectance microscopy was performed using Olympus cell^TIRF illuminator motorized multicolor TIRF microscope (60x objective). Images were captured using an ImagEM camera (c9100-14). Images were taken every 15 sec for 1 hr to monitor focal adhesion dynamics and 150 sec for 3 hr to analyze focal adhesion alignment.

Electron Microscopy

Scanning EM: Cells were plated onto 10 µg/mL FN coated coverslips overnight, rinsed gently 2-3 times with serum-free medium warmed to 37 ℃ and fixed with 3% glutarldehyde in 0.1 M sodium cacodylate buffer (pH 7.4) with 0.05% $CaCl_2$ for 30min at room temperature followed by subsequent treatment with 2% tannic acid for 10 min and 1% osmium tetroxide in water for 10 min [71]. The coverslips were dehydrated with ethanol and dried in a Samdri-795 critical point dryer using carbon dioxide as the transitional solvent (Tousimis Research Corporation, Rockville, MD). Coverslips were mounted on aluminum planchets with double-sided carbon adhesive and coated with 10 nm of gold-palladium alloy (60Au:40Pd, Hummer X Sputter Coater, Anatech USA, Union City, CA). Images were taken using a Zeiss

Supra 25 FESEM operating at 5 kV, working distance of 5mm, and 10µm aperture (Carl Zeiss SMT Inc., Peabody, MA).

Cryo-shadowing EM: Nickel grids (150-mesh) covered with a carbon film were treated with a glow discharge at 200 torr for 2 min. FN (10 µg/mL) was used to coat the glow-treated surface for 1 hr at 37 ℃. Cells were plated on grids for 2.5 hr in regular cell culture medium before extraction with extraction buffer (1% Triton X-100 and 2 µM phalloidin in PEM buffer containing 100 mM PIPES, 1 mM EGTA, 1mM $MgCl_2$, pH 6.9) for 4 min at room temperature [72]. After extraction, cells were rinsed with PEM buffer (pH 6.9) for 1 min and fixed with 1% glutaraldehyde in PBS for 5 min at room temperature. After fixation, grids were briefly rinsed with distilled water and transferred to the chamber of an FEI Vitrobot freezing robot held at 37 ℃ and 100% humidity [57]. The water remaining on the grid was gently blotted with filter paper before plunging the grid into liquid ethane for rapid freezing. The grids in an enclosed box under liquid nitrogen were transferred to the stage of a modified Balzers freeze etch machine held at -120 ℃. The chamber was evacuated and the sample slowly freeze dried at $1x10^{-5}$ to $5x10^{-7}$ torr for 4 hr while the temperature was ramped from -120 to -85 ℃. The samples were then rotary shadowcast with tungsten prior to breaking the vacuum.

The grids were examined in an FEI Tecnai T12 Teat 80 kV. The images were taken with either sheet film or using a GATAN Inc Oris 1000 2Kx2K digital camera. Images on film were scanned using an Imacon 848 film scanner. Image levels were adjusted and the contrast inverted using Adobe Photoshop.

Directional migration assays

Microfludic device preparation: Transparency masks were printed using a high-resolution printer (Fineline Imaging, CO). The pattern for the chemotaxis chamber was fabricated on 4” silicon wafers using a two-step photolithography process. The first step involved a 5 µm tall layer of SU-8 (25) from microposit and the microcapillaries were transferred to the wafer. After developing the first layer a second 100 µm tall layer of SU-8 (100) was applied to the same wafer and after alignment the channels were transferred to the wafer. After developing and post-baking, the silicon wafer was exposed to silane overnight. Polymethylsiloxane (PDMS) was then poured on the wafer and cured in overnight at 70ºC. Individual PDMS devices were cut out from the wafer and placed in a clean dish until use. The sharp ends of 20 gauge needles were cut off and the ends were then smoothed using a Dremel tool. The needles were then used to punch out ports in the devices. The devices were then washed with water and ethanol, blow-dried and exposed to air plasma for 2 min in a plasma cleaner (Harrick plasma). Glass bottom culture dishes (MatTek) or Delta T dishes (Bioptechs) glass dishes were cleaned using water and ethanol and then exposed to plasma for 2 min. The PDMS device was placed into contact with glass dish bottom immediately following plasma treatment of both pieces, ensuring that an irreversible seal was formed. The cell culture chamber was then filled with 10 µg/mL FN for 1 hr at 37 ºC, followed by flushing with sterile PBS. Cells were loaded into the cell culture chamber using a gel loading pipette tip. The cell chamber ports were plugged with short pieces of tubing (Upchurch Scientific, .0025” x 1/32”).

Chemotactic gradients: The exit ports of the sink and source channels were connected to waste using tubing of ID 0.015". Gas tight 100 µL Hamilton glass syringes (81020,1710TLL 100 µL SYR) were connected to 27 1/2 gauge needles connected to tubing. The source syringe and tubing were filled serum free DMEM containing indicated chemoattractant and 10 µg/mL of TRITC-dextran to visualize the gradient. The sink syringe and tubing were filled with serum free DMEM. The tubing was then inserted into the source and sink channels respectively, and the syringe pump was operated at a flow rate of 20 nL/min. A stable gradient was then established in the cell culture chamber within 30 min, and typically remained stable for 18 hr as monitored by TRITC-dextran fluorescent intensity.

Haptotaxis gradients: Identical chambers as in the chemotaxis experiments were prepared. After bonding device to dish, the cell culture was coated with a minimal concentration of 2.5 µg/mL FN (or 5 µg/mL LN) to promote cell attachment throughout the chamber. The source and sink syringes were filled with the indicated concentration FN (or LN or VTN) in PBS or PBS alone respectively. The syringe pump was maintained at a flow rate of 20 nL/min. The chambers were allowed to equilibrate for 1 hr. Once the ECM gradient was established, 1 mg/mL PLL(20)-g[3.5]-PEG(2) was flowed into all channels of the device to block non-specific adhesion. Thorough wash of the chambers with distilled water was performed before plating the cells.

Directional migration image acquisition and analysis: Chemotaxis assays were performed on an Olympus DSU microscope with a 20X objective using MetaMorph imaging software. Images were collected every 10 min for over 12 hr. Haptotaxis

assays were performed on the Nikon Biostation IM using a 20x objective and at the same time interval. Individual cells were manually tracked using ImageJ software Manual Tracking plug-in. The tracks obtained were further analyzed using the chemotaxis tool developed by IBIDI (http://www.ibidi.de/applications/ap_chemotaxis.html#imageanalysis). This analysis tool was used to extract the FMI and histogram of angular direction of tracks from the manual tracking results. To obtain the Compass Parameter (CP), the histograms obtained were further analyzed in GraphPad Prism software by performing a non linear curve fit to the chemotaxis equation.

Focal Adhesion Segmentation and Measurements: To identify focal adhesions in each image of a time-lapse series, a set of segmentation methods were used [64]. Each movie was cropped to only include one cell. Starting with the raw images from the TIRF movies, we used a high-pass filter to minimize background noise and the overall distribution of pixel intensities after high-pass filtering was used to select a threshold for adhesion detection. For all image sets examined, we selected a threshold of the mean plus two standard deviations of the high-pass filtered pixel intensities. We then applied the threshold and connected components labeling to identify each adhesion and removed any single pixel objects identified. After identifying the adhesions, they were tracked through time using a previously published method [64] and a range of properties were collected. All of the per adhesion properties (mean area, axial ratio, major axis length, minor access length and longevity) were only calculated for adhesions where both a birth and death event was detected.

In order to measure the global alignment of focal adhesions across the entire cell, we developed the focal adhesion alignment index (FAAI). The index is determined by a two-step process. The first step involved collecting and filtering the adhesion angles in each image of the time-lapse, while the second step involved searching for a reference angle that minimizes the deviation between all of the adhesion angle measurements. We began the first step by segmenting the adhesions from each frame of a time-lapse movie. From this set of identified adhesions in each frame, we calculated the best-fit ellipse to each adhesion. From this ellipse, we found the length of the major axis, the length of the minor axis and the angle the major axis of the adhesion made with the positive x-axis. Angle measurement was on a scale of -90°-90° to avoid the ambiguity of the 360° measurem ent scale. We set the minimum ratio of the lengths of the major over minor axes to three as a filter to select adhesions whose orientation could be determined. After collecting the adhesion angles with the positive x-axis as the reference, the second step of calculating the index began with a search through a range of potential reference angles. The search began at with the x-axis as the 0° position and the calculation of the standard deviation of the adhesion angles. Then the reference angle is increased by 0.1°, the adhesion angles with the new reference axis are recalculated and the standard deviation measured. This search process continued until the full range (0°-179.9°) of potential reference angles had been sampled. The FAAI is calculated for all reference angles as:

FAAI = 90 – SD (adhesion angles at a given reference angle)

We choose this formulation as it provides an intuitive interpretation of the index; high values of the FAAI indicate that the adhesions in a cell are well aligned (low standard deviation) and low values of the FAAI indicate that the adhesions are not well aligned (high standard deviation). The dominant adhesion angle is defined as the reference angle that maximizes the FAAI. In cases where there are multiple angles that maximize the FAAI, the reference angle that minimizes the absolute value of the mean adhesion angle is selected from the list of angles that maximize the FAAI as the dominant angle. The final number reported is the value of the FAAI at the dominant angle.

We also wanted to measure the variation through time in the angles formed by single adhesions. To measure single adhesion angle variation, we tracked the adhesions identified through each frame of the movie using a tracking method based on overlap with prior adhesions and the centroid distance between nearby adhesions [64]. From this data set of tracked adhesions we excluded angle measurements with a major/minor length ratio less than three and determined each adhesion's dominant angle. We rotated each adhesion's frame of reference to match that adhesion's dominant angle and measured the mean absolute value difference between the adhesion's first measured angle and the rest of the adhesion's angle measurements.

Chapter 3

Loss of Arp2/3 complex induces an NF-κB-dependent secretory response that leads to non-autonomous effects on chemotactic signaling

3.1 Summary

The actin cytoskeleton has well-established roles in motility, cytokinesis and vesicular trafficking, but also participates in signaling pathways in ways that are incompletely understood. Using RNAseq, we compared the global transcriptional profiles of cells with and without the Arp2/3 complex that generates branched actin structures. Surprisingly, the main class of genes with altered expression levels were not cytoskeleton genes, but genes encoding secreted factors including chemokines, growth factors and matrix metaloproteases. Highlighting the importance of these secreted factors up-regulated upon Arp2/3 perturbation, we demonstrate that conditioned media harvested from Arp2/3 depleted cells can reversibly block EGF chemotaxis in microfluidic chambers, resolving recent contradictory findings about the role of Arp2/3 complex in chemotaxis. The gene expression signature induced by Arp2/3 loss resembles the senescence associated secretory phenotype (SASP) that is activated upon oncogenic and cellular stress. These genes are predominantly targets of the NF-κB pathway, and depletion of Arp2/3 or treatment with the newly developed small molecule inhibitor (CK-666) leads to NF-κB activation in cultured cells and zebrafish embryos. Loss of Arp2/3 complex or its inhibition activates NF-κB

via a CCM2-MEKK3 pathway that has previously been implicated in osmotic stress signaling. Cells depleted of Arp2/3 show elevated and sustained p38MAPK activation upon sorbitol treatment. Interestingly, shifting Arp2/3 depleted cells to hypo-osmotic conditions recues the signaling defects. Consistent with this, live imaging of Arp2-knockdown/rescue cells reveals that Arp2/3 complex is mobilized to the actin cortex in a delayed fashion following osmotic shock, indicating its important role in strengthening actin cortex. These data suggest that experimental manipulations and human diseases that affect the Arp2/3-actin cytoskeleton have both autonomous effects on the cytoskeleton and potential non-autonomous effects such as confounding inflammatory responses.

3.2 Introduction

Cytoskeletal integrity is important for cell morphology and motility, and is thought to be critical for some signal transduction pathways [34-36]. Defects in actin cytoskeletal integrity are seen in a variety of human diseases and cytoskeletal dynamics become deregulated in cancer metastasis and autoimmune disorders [1, 2]. Perturbation of cytoskeleton is tightly linked to abnormal cell migration [8, 32]. The direct or indirect autonomous effects of actin perturbation on cell motility have been reported in drug perturbation, genetic depletion or overexpression systems [29, 32, 33]. However, under these conditions and in cases of human diseases involving altered actin cytoskeleton, signaling changes caused by actin perturbation may also induced non-cell-autonomous effects which have largely been understudied.

It has long been noticed that the perturbation of the cytoskeleton machinery affects signaling pathways [34-36]. Depolymerization of microtubules release the guanine exchange nucleotide factor GEF-H1, increasing Rho activity and resulting in increased actomyosin contraction [37]. Actin stress fibers are shown to have mechanosensitive properties and involved in cascades of signaling events [73]. It has also been reported that certain actin drugs lead to incresed NF-κB activity [38, 39]; however, its mechanism or effects on cell physiology have not yet been addressed. Emerging data has revealed that NF-κB signaling is the major signaling pathway which stimulates the appearance of SASP (the senescence associated secretory phenotype), in which senescent cells secrete pro-inflammatory factors [40]. All of these senescence-associated secreting factors are involved in homeostatic disorders such as cancer [41]. These factors including growth factors, cytokines and

chemokines, highly resembling what has been reported in SASP (senescence associated secretory phenotype). SASP factors are known to cause non-cell-autonomous effects on cell migration, and are under regulation of NF-κB and p38MAPK pathways [40, 74-76]. Thus, the intriguing potential crosstalk among actin cytoskeleton perturbation, increased NF-κB activity, secretory factor release and non-autonomous effects on cell migration becomes extremely exciting and interesting to test.

Cells have a special actin structure-the branched actin network that has been primarily studied focusing on the cell leading edge. Branched actin network is initiated and maintained by the seven-subunit protein complex Arp2/3. Arp2/3 complex binds existing actin mother filaments and generates new daughter filaments as branches off of the mother filaments, creating a dentritic network with ~70 degree angle underneath the plasma membrane. We recently established a stable fibroblast cell line lacking two subunits of the Arp2/3 complex (p34Arc and Arp2, referred to as 2xKD cells throughout) that are devoid of branched actin-generated structures such as the lamellipodium [29]. We showed that the branched actin network is important for normal cell migration and essential for sensing and responding to changes in extracellular matrix concentration (haptotaxis). Despite defects in random and haptotactic migration, these cells were still capable of chemotaxis towards PDGF using a microfluidic system [29], suggesting important differences in the molecular machinery of chemotaxis vs. haptotaxis. The surprising viability of these cells was due, in part, to the genetic background effects of the loss of Ink4a/Arf tumor

suppressors[29]. These results suggest that the loss of Arp2/3 may induce senescence in an Ink4a/Arf-dependent manner.

In the present study, we compared the global transcriptional profiles of cells with and without the Arp2/3 complex and identified the cell-non-autonomous effects of Arp2/3-depletion, through the regulation of NF-κB and MAPKs. Our data suggest that experimental manipulations and human diseases that affect the Arp2/3-actin cytoskeleton have both autonomous effects on the cytoskeleton and potential non-autonomous effects such as confounding inflammatory responses.

3.3 Results

Depletion of Arp2/3 complex induce expression of secretory factors

To further understand the role of Arp2/3-generated branched actin on overall cellular physiology, we performed whole transcriptome RNASeq-based expression profiling of our 2xKD cells, and detected unexpected up-regulation of many genes encoding secreted proteins such as chemokines, growth factors and proteases. Based on DAVID Analysis of the top 500 genes increased in 2xKD cells, the list of upregulated genes contains an over-representation of immune and inflammatory genes (Figure 23A). This result was confirmed for a subset of the genes at the transcript level by qRT-PCR (Figure 23B) and at the protein level by ELISA analysis of proteins secreted from the cells (Figure 23C).

A

DAVID Analysis of Top 500 Genes Ranked by Fold Increase in 2xKD	
Gene Ontology Term	**Benjamini Score**
defense response	3.54E-11
inflammatory response	7.83E-11
immune response	2.83E-10
response to wounding	5.40E-09
acute inflammatory response	8.74E-08
innate immune response	3.51E-07
cell adhesion	1.47E-05
biological adhesion	1.34E-05
humoral immune response mediated by circulating immunoglobulin	5.77E-04
immune effector process	6.81E-04
positive regulation of immune response	1.37E-03
lymphocyte mediated immunity	1.58E-03
acute-phase response	2.07E-03
complement activation, classical pathway	2.07E-03
immunoglobulin mediated immune response	2.49E-03
B cell mediated immunity	2.94E-03
activation of immune response	3.26E-03
positive regulation of immune system process	3.18E-03
leukocyte mediated immunity	3.81E-03
complement activation	4.22E-03
activation of plasma proteins involved in acute inflammatory response	4.22E-03

B

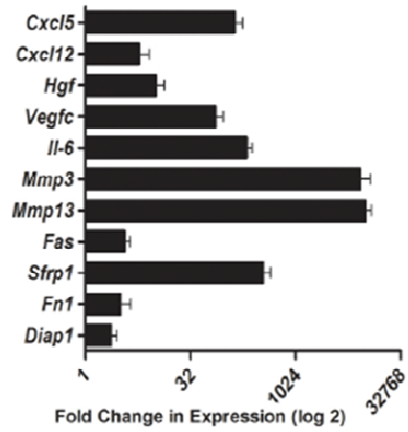

C

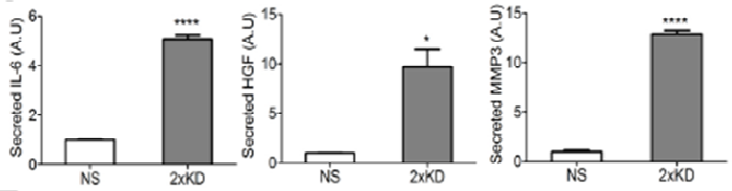

Figure 23: Loss of Arp2/3-complex induced upregulation of secretory factors

A) The transcriptomes of IA32 fibroblasts and their Arp2/3-depleted derivatives (2xKD) [29] were analyzed by RNASeq. DAVID analysis of top 500 genes (>10 fold up-regulated) with highest fold increase in 2xKD cells, ranked by Benjamini score.

B) qRT-PCR showing fold changes of a subset of growth factors, MMPs and cytokines up-regulated in 2xKD cells in the RNA-Seq experiments. Error bar: 95% confidence interval. 2 biological replications (each has 3 technical replications) for each sample.

C) ELISA showing levels of secreted IL-6, MMP3 and HGF in control NS and 2xKD cells. NS and 2xKD cells were cultured in serum free DMEM for 12 hrs before collecting the media. Conditioned media from NS and 2xKD cells were then analyzed by commercial ELISA kits with 3 repeats. Normalized protein levels were plotted with Prism. Error bar: 95% confidence interval. ****P<0.001, *P<0.05 by Student's t test.

Secretory factors released by Arp2/3-depleted cells affect chemotaxis in a non-cell-autonomous way

One functional consequence of the change in secreted proteins upon Arp2/3 depletion is that signaling/motility processes such as chemotaxis may be affected in a non-cell autonomous manner depending on the experimental regime. For example, we recently demonstrated that Arp2/3 deficient cells could chemotax up gradients of PDGF in a microfluidic device [29], whereas Suraneni et al observed the loss chemotaxis of Arp2/3 deficient cells in response to gradients of EGF [77]. Given that Arp2/3 deficient cells secrete increased levels of growth factors such as HGF, we reasoned this apparent discrepancy could be due to differences in media exchange in the respective chemotactic chamber designs (closed [77] vs continuous flow [29, 78]). To mimic the closed chamber design, we used conditioned media (CM) in our continuous flow chambers. CM from the Arp2/3-depleted cells (2xKD) blocked EGF chemotaxis in both control (NS) and 2xKD cells, but NS CM did not affect this process in either cell line (Figure 24A). To test whether conditioned media affected EGF signaling, we compared AKT activation (p-AKT) levels of NS and 2xKD cells after EGF stimulation in the different media. In the presence of 2xKD CM, both cell types had high basal level of AKT activation that could not be further stimulated by EGF (Figure 24B). Together, these results indicate that 2xKD conditioned media disrupts normal EGF signaling sensitivity and perturbs the ability of fibroblasts to migrate up an EGF gradient. Interestingly, 2xKD conditioned media did not show the same effect on PDGF chemotaxis or signaling (Figure 24C, D), suggesting that this pathway is relatively insensitive to the factors contained in the 2xKD CM. To

establish that the effects of 2xKD CM are reversible, we replaced 2xKD CM with control CM part way through an EGF experiment and observed restored chemotactic response (Figure 24E).

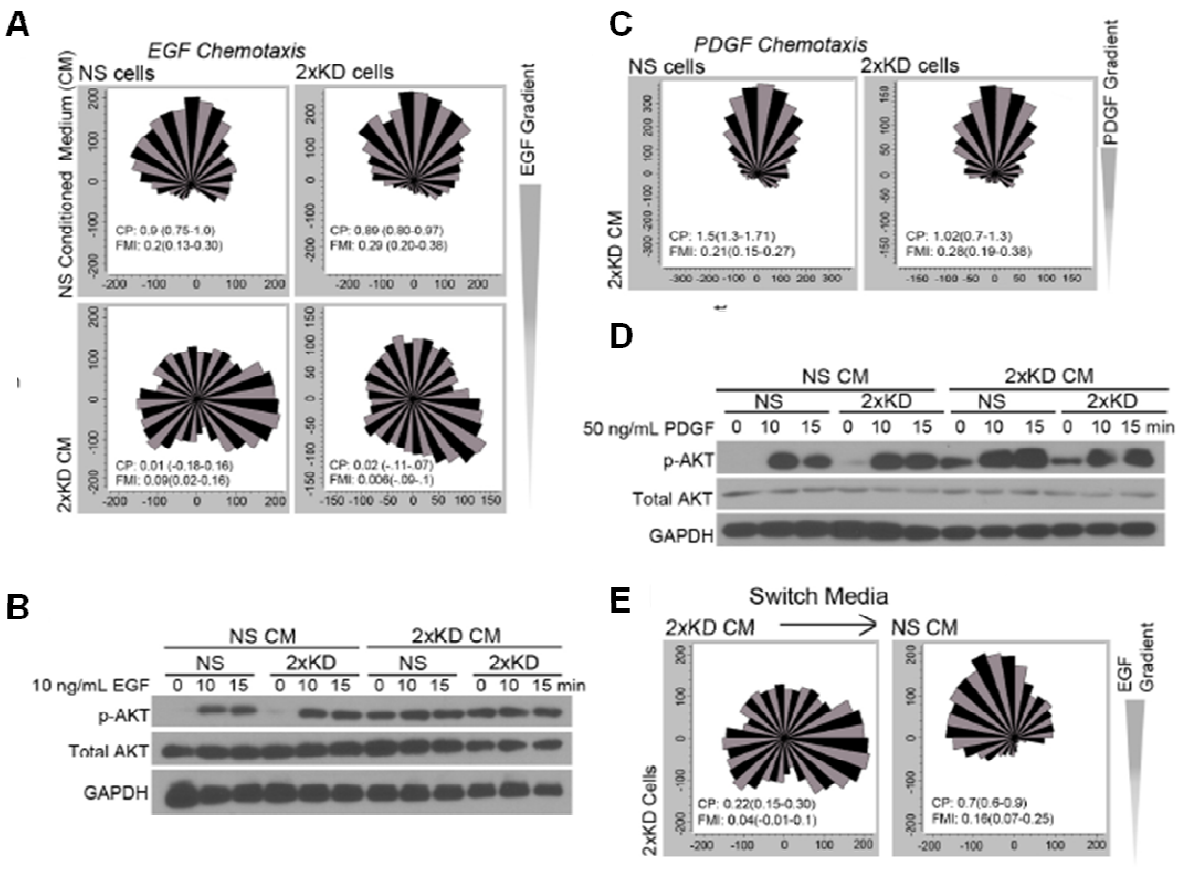

Figure 24: Loss of Arp2/3-complex affects chemotaxis in a cell non-autonomous way

A) Wind rose plots showing NS and 2xKD cells in NS conditioned media (NS CM) or 2xKD CM in EGF chemotaxis. 100 ng/mL EGF was used as chemoattractant. Compass parameter (CP) and forward migration index (FMI) are indicated on the graph, numbers in parentheses show 95% confidence intervals. N=72 for 2xKD cells in 2xKD CM, N=73 for 2xKD cells in NS media, N=79 for NS cell in 2xKD CM and N=60 for NS cells in NS CM.

B) Western blots showing phospho-AKT (p-AKT), total AKT and GAPDH levels in NS and 2xKD cells upon EGF stimulation at indicated timepoints. Representative blot from three experiments is shown.

C) Wind rose plots showing NS and 2xKD cells in NS CM or 2xKD CM during PDGF chemotaxis. 100 ng/mL PDGF was used as chemoattractant. Compass parameter (CP) and forward migration index (FMI) are indicated on the graph, numbers in parentheses show 95% confidence intervals. N=76 for 2xKD cells in 2xKD CM and N=72 for NS in 2xKD CM.

D) Western blot showing p-AKT, total AKT and GAPDH levels in NS and 2xKD cells upon EGF stimulation at indicated timepoints.

E) Wind rose plots showing 2xKD cells in EGF chemotaxis, before (right) and after (left) switching from 2xKD CM to NS CM. Compass parameter (CP) and forward migration index (FMI) are shown on the graph, numbers in parentheses show 95% confidence intervals. 2xKD cells were plated in chemotaxis chamber and serum-starved overnight before carrying out EGF chemotaxis experiment in the presence of 2xKD CM. After 4 hrs, 2xKD CM was switched to NS CM and EGF chemotaxis was continued for another 4 hrs. Compass parameter (CP) and forward migration index (FMI) are indicated on the graph, numbers in parentheses show 95% confidence intervals. N=52.

Secretory pathway activated by loss-of-Arp2/3 is regulated by NF-κB

Interestingly, the secretory factor genes up-regulated in the Arp2/3-depleted cells largely overlapped with the SASP (senescence associated secretory phenotype) signature [40, 76, 79]. The SASP response has been reported to occur with DNA damage, oncogene activation and cellular stress, and is regulated by NF-κB [75, 80, 81]. Thus, we postulated that the loss of Arp2/3 complex would lead to activation of NF-κB. Using phosphorylated RelA/p65 (p-p65) as a surrogate for NF-κB activity, we detected strong activation in Arp2/3-depleted cells and in multiple cell lines treated with the Arp2/3 complex inhibitor CK-666 (Figure 25A, B).

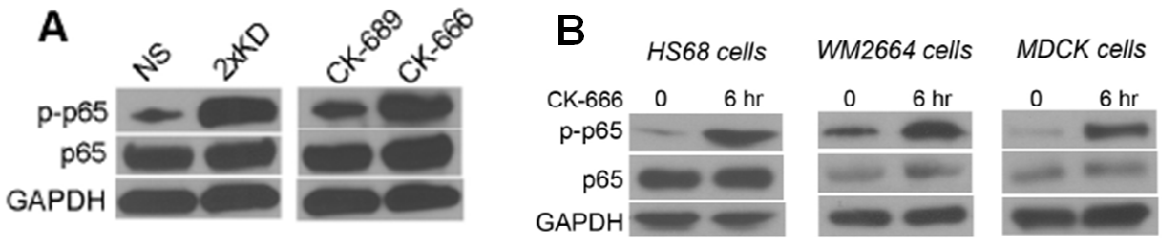

Figure 25 Up-regulation of secretory pathways by Arp2/3-depletion is regulated through NF-κB

A) Western blot showing phospho-p65 (Ser536) (p-p65), total p65 and GAPDH levels in NS and 2xKD cells (left) and NS cells treated with 100 μM Arp2/3 inhibitor CK-666 or its inactive control compound CK-689 for 6 hrs (right).

B) Inhibition of Arp2/3 complex caused increased NF-κB activation in multiple cell lines. HS68 (human foreskin fibroblasts), WM2664 (human melanoma cells) and MDCK (epithelial cells) were treated with 100 μM CK-666 for 0 or 6 hrs before being lysed. Western blot showed p-p65, p65 and GAPDH levels in these three cell lines under indicated treatment.

Using an IKK inhibitor (cmpdA) [82], we observed that the elevated p-p65 level in 2xKD cells could be reduced suggesting that a canonical NF-κB activation pathway was involved (Figure 26A). This same treatment decreased the expression of secretory factors by qRT-PCR and ELISA (Figure 26B, C). Importantly, this treatment did not affect the reduced random migration speed or altered cell morphology that we reported previously for loss of Arp2/3 complex activity (Figure 26D, E)[29]. To confirm our findings with an alternate approach, we utilized a zebrafish NF-κB reporter line [83]. Treating day 2 post-fertilization embryos of this line with CK-666 showed an increased expression of GFP in tail fin fold relative to controls (Figure 27).

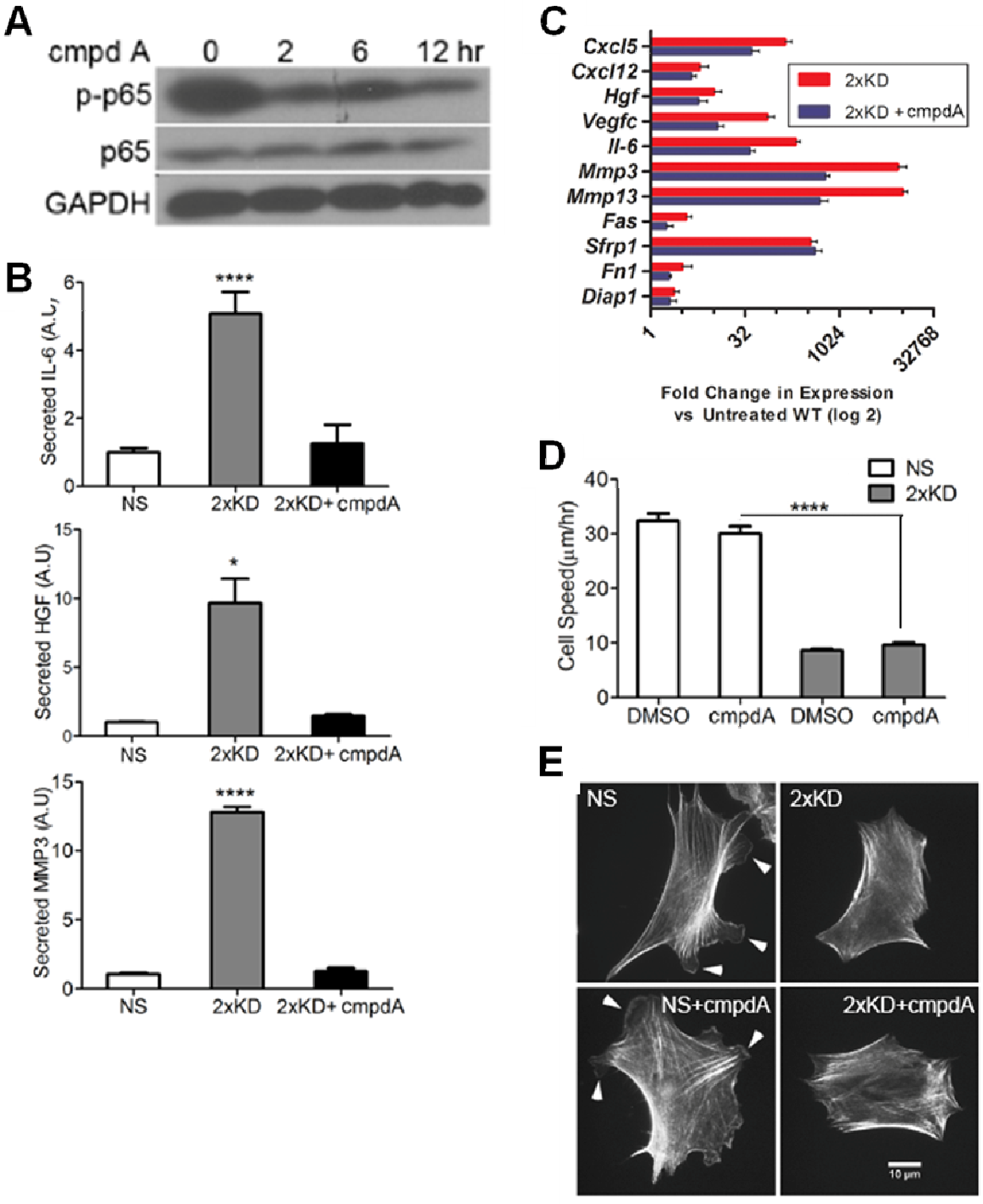
A
cmpd A
0
2
6
12 hr
p-p65
p65
GAPDH
B
Secreted IL-6 (A.U)
****
NS
2xKD
2xKD+ cmpdA
Secreted HGF (A.U)
*
Secreted MMP3 (A.U)
****
C
Cxcl5
Cxcl12
Hgf
Vegfc
Il-6
Mmp3
Mmp13
Fas
Sfrp1
Fn1
Diap1
2xKD
2xKD + cmpdA
1
32
1024
32768
Fold Change in Expression
vs Untreated WT (log 2)
D
Cell Speed(μm/hr)
NS
2xKD
****
DMSO
cmpdA
DMSO
cmpdA
E
NS
2xKD
NS+cmpdA
2xKD+cmpdA
10 μm

Figure 26 Cmpd A reversed the effect of Arp2/3 loss on secretory factor upregulation without affecting cell motility or morphology

A) Western blot showing levels of p-p65, p65 and GAPDH in 2xKD cells treated with IKK inhibitor cmpdA (5μM) for indicated time.

B) ELISAs showing secreted IL-6, HGF and MMP3 levels in 2xKD cells with and without cmpdA treatment compared to NS cells. Conditioned media (CM) from 2xKD cells with or without 5 μM cmpdA treatment were collected after culturing cells in serum-free DMEM for 12 hrs. ELISAs were then performed according to the manufacture's protocols.

C) qRT-PCR showing the expression fold changes of indicated genes compared to Wild Type IA32 cells. 2xKD cells were treated with or without 5 μM cmpdA for 12 hrs before being harvested for qRT-PCR. Fold changes were analyzed using pfaffl method.

D) Graph showing cell speed of NS and 2xKD cells with 0.5% DMSO or 5 μM cmpdA treatment. N=40 for each group. ****P<0.001. d) Phalloidin staining showed F-actin in NS and 2xKD cells. Lamellipodia in NS cells were pointed out by white arrowheads. Scale bar: 10 μm.

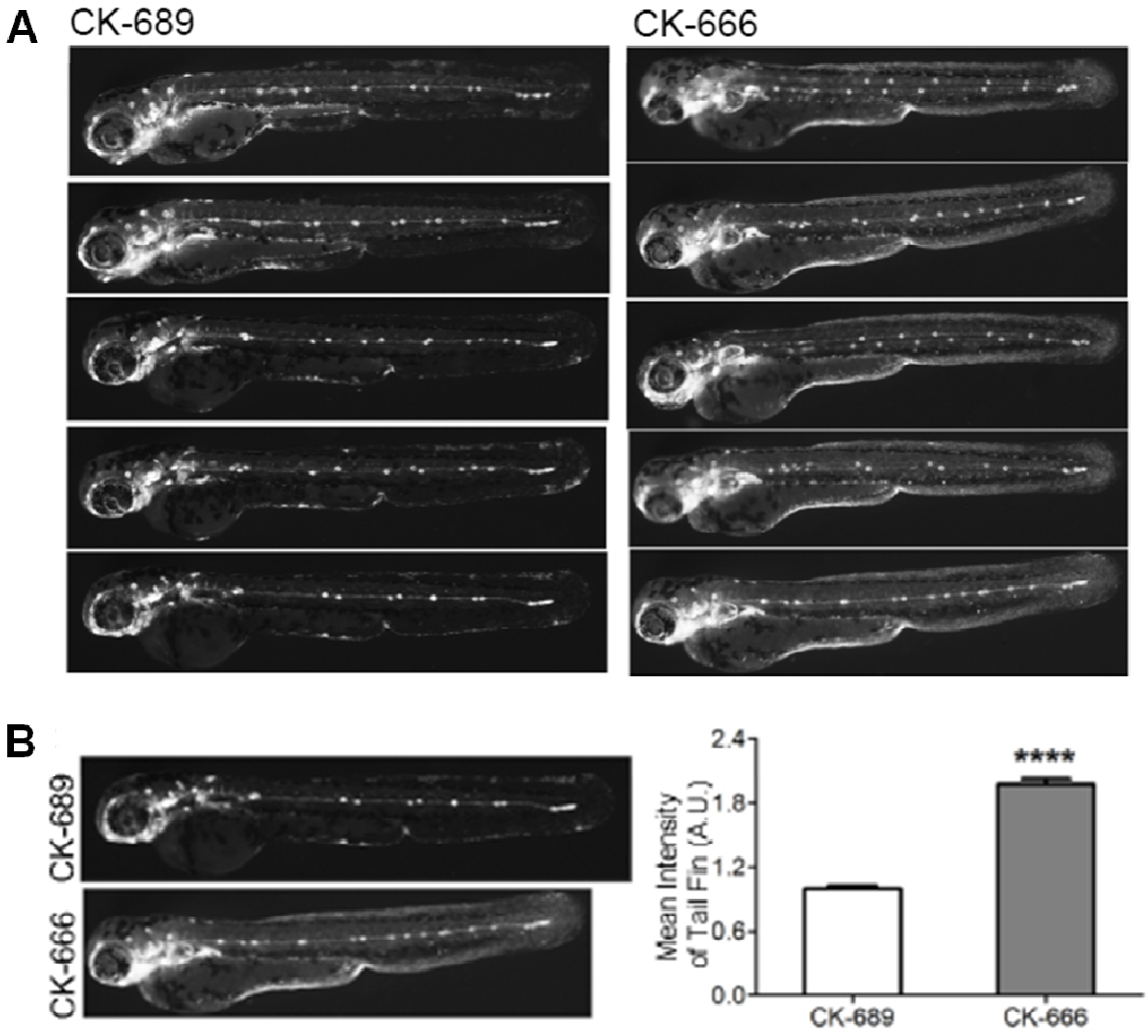
A
CK-689
CK-666
B
CK-689
CK-666
Mean Intensity of Tail Fin (A.U.)
2.4
1.8
1.2
0.6
0.0
****
CK-689
CK-666

Figure 27 NF-κB activation by loss of Arp2/3 activity is confirmed in a zebrafish reporter line

A) Multiple examples showing day 2 post fertilization pNF-κB:GFP zebrafish embryos [83] treated with 100 μM CK-666 and its control compound CK-689 for 12 hrs.

B) Day 2 post fertilization pNF-κB:EGFP zebrafish embryos were treated with 100μM Arp2/3 inhibitor CK-666 or its control compound CK689 for 12 hrs before imaging. (Left) Fluorescent images showing EGFP expression representative fish; (Right) quantification of the mean fluorescent intensity of fish tail fin. N=10. ****P<0.001 by Student's t test.

Activation of NF-κB by Arp2/3-depletion is regulated through MEKK3/CCM2 pathways

Previous work has implicated p38MAPK as a key upstream factor in the activation of the SASP pathway [75]. To test whether p38MAPK is activated by the loss of Arp2/3, we blotted for p-p38 (active) and observed elevated levels in both Arp2/3 depleted and CK-666 treated cells (Figure 28A). To test whether p38MAPK is upstream of the observed NF-κB activation in Arp2/3 inhibited cells, we simultaneously treated cells with p38MAPK inhibitor SB203580 and CK-666 and still observed elevated p-p65, suggesting that p38MAPK is not directly upstream in this case (Figure 28B). However, consistent with previous studies, pre-treatment with SB203580 for >12 hours did inhibit CK-666's effect on p-p65 levels (Figure 28C), suggesting that p38MAPK may indirectly affect this response.

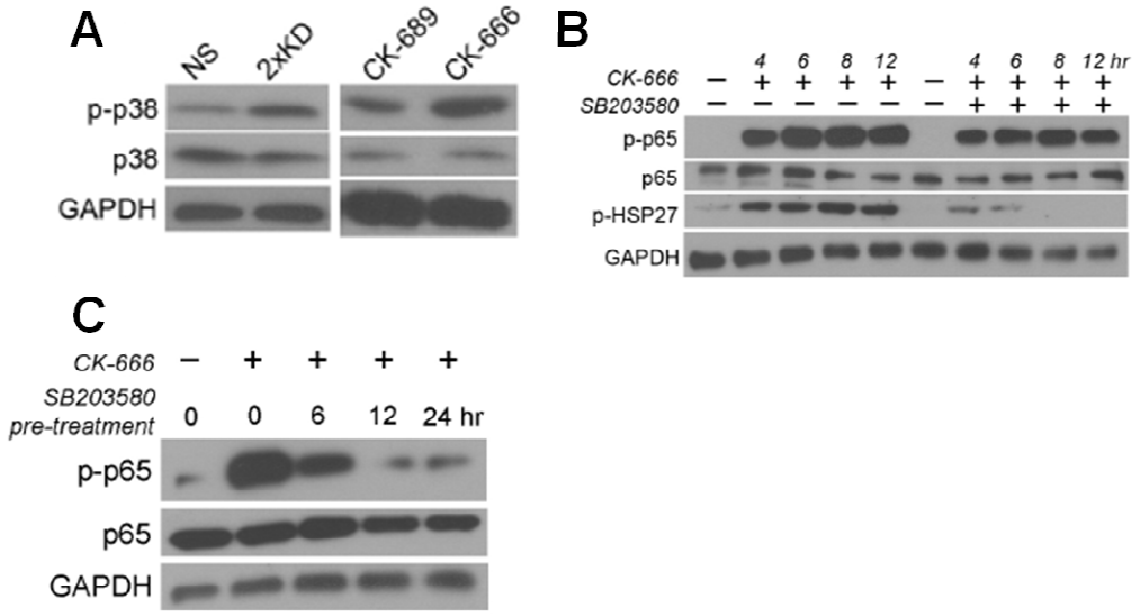

Figure 28 p38MAPK is indirectly involved in regulating NF-κB upon loss of Arp2/3 activity

A) Western blot showing phospho-p38 MAPK (Thr180/Tyr182) (p-p38), total p38 and GAPDH levels in NS and 2xKD cells (left); and NS cells treated with 100μM CK-689 or CK-666 for 6 hrs (right).

B) Western blot showing p-p65, p65, p-HSP27 and GAPDH levels of IA32 cells with 100 μM CK-666 only and simultaneous 10 μM SB203580+100 μM CK-666 treatments at indicated timepoints. Decreased p-HSP27 levels indicate effective inhibition of p-38 activation by SB203580.

C) Pre-inhibition of p38MAPK for >12 hrs abrogated the effect of Arp2/3 inhibition on NF-κB activation. IA32 cells were pre-treated with 10 μM p38MAPK inhibitor SB203580 for indicative time before adding 100 μM CK-666. p-p65, p65 and GAPDH were blotted.

One upstream candidate molecule that activates both IKK-NF-κB and p38MAPK is MEKK3 [84-86]. To test whether MEKK3 is involved in this pathway, we treated MEKK3-/- cells with CK-666 and observed no activation of NF-κB (Figure 29A). To test how specific MEKK3 is for this pathway, we added CK-666 to cells lacking MEKK2 (the closest protein relative of MEKK3 [87]), and observed NF-κB activation (Figure 29B). MEKK3 activity is regulated by the actin-binding scaffolding protein CCM2 (also known as OSM) [84]. To test whether CCM2 is involved in Arp2/3-based regulation of NF-κB, we depleted CCM2 using two distinct siRNAs and observed no activation of NF-κB in response to CK-666 treatment (Figure 29C, D).

Previous work has implicated the CCM2-MEKK3 pathway in osmotic stress signaling. Using live-cell imaging of tagged CCM2, we observed a transient nuclear translocation of this protein during hyper-osmotic response (Figure 30A). Interestingly, CK-666 treatment caused a slow, but more persistent nuclear translocation of CCM2 (Figure 30A) with no diminished nuclear signal even after 4 hrs of treatment (Figure 30B).

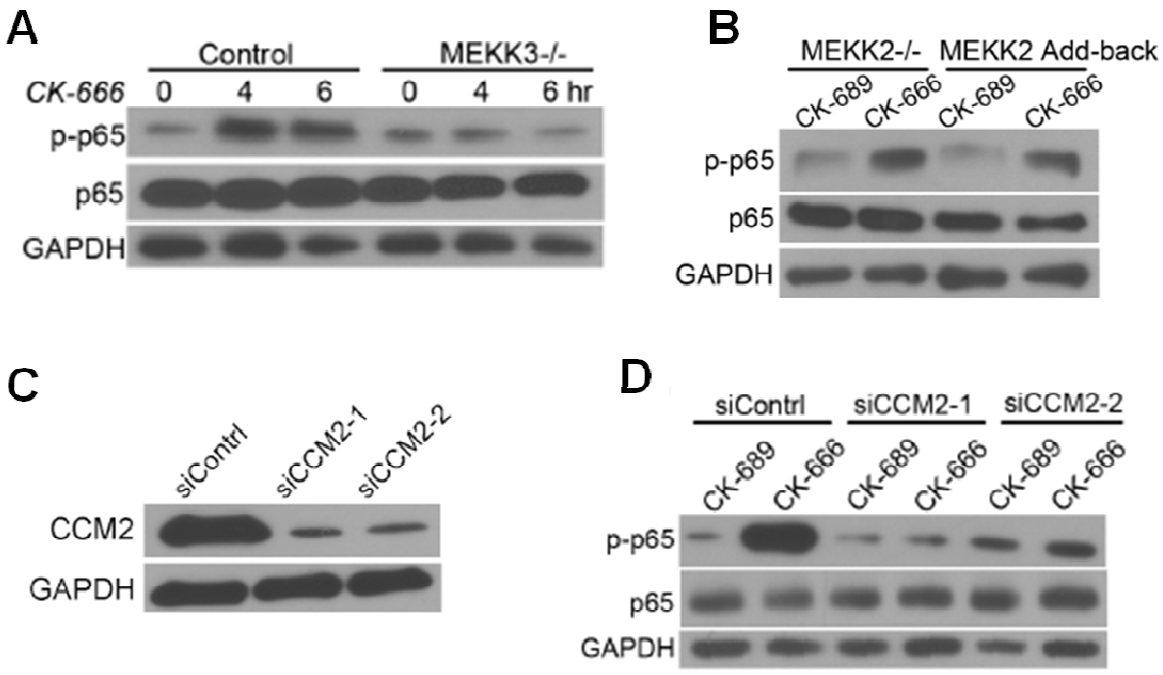
A
Control
MEKK3-/-
CK-666 0 4 6 0 4 6 hr
p-p65
p65
GAPDH
B
MEKK2-/-
MEKK2 Add-back
CK-689
CK-666
CK-689
CK-666
p-p65
p65
GAPDH
C
siContrl
siCCM2-1
siCCM2-2
CCM2
GAPDH
D
siContrl
siCCM2-1
siCCM2-2
CK-689
CK-666
CK-689
CK-666
CK-689
CK-666
p-p65
p65
GAPDH

Figure 29 MEKK3/CCM2 is regulating NF-κB activation upon loss of Arp2/3 activity

A) Western blot showing p-p65, p65 and GAPDH levels of control and MEKK3-/- MEF cells upon 100μM CK-666 treatment for indicated time.

B) MEKK2 does not regulate loss of Arp2/3-induced NF-κB activation. MEKK2-/- or MEKK2 -/-/MEKK2 addback MEFs were treated with 100 μM CK-666 or its inactive control compound CK-689 for 6 hrs before harvesting cells. p-p65, p65 and GAPDH were blotted.

C) CCM2 is effectively silenced using siRNA. Western blot of IA32 cells treated with control siRNA (siContrl), two CCM2 siRNAs (siCCM2-1 and siCCM2-2) were harvested and blotted for CCM2 and GAPDH.

D) Western blot showing p-p65, p65 and GAPDH levels of control siRNA and two CCM2 siRNA treated IA32 cells with 100μM CK-689 or CK-666 treatment for 6 hrs.

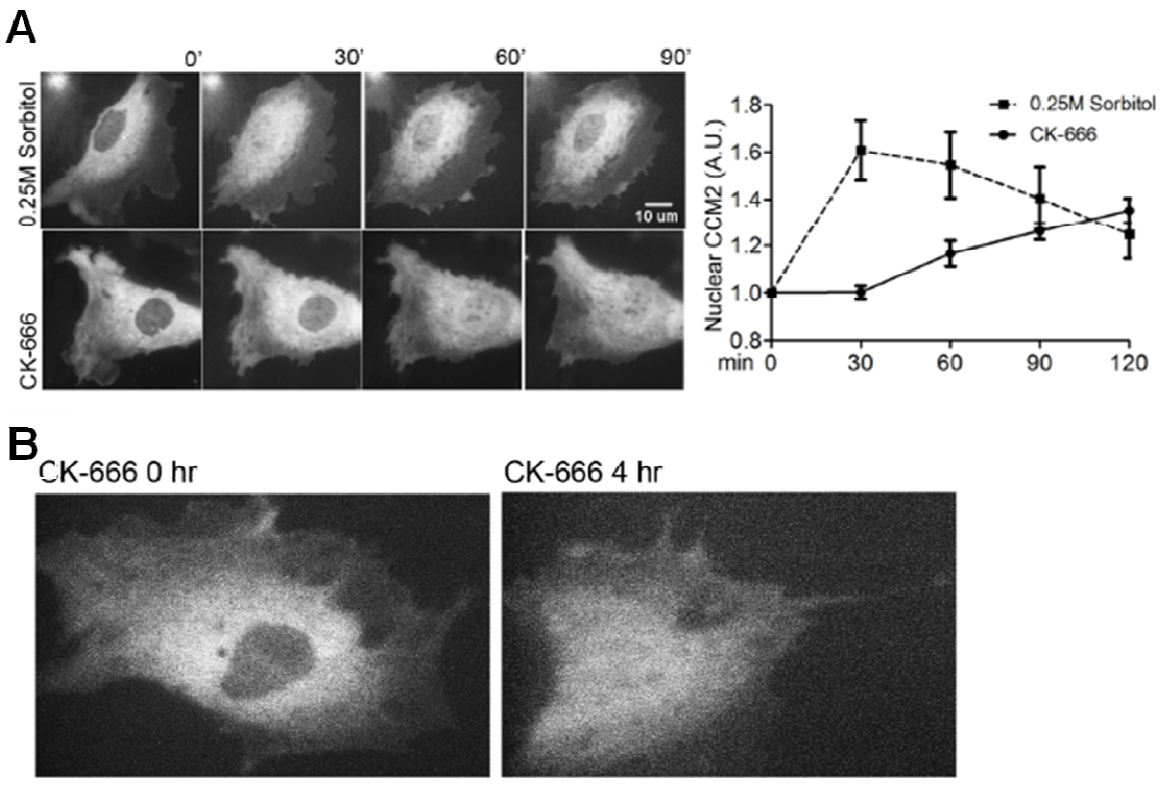

Figure 30 CCM2 shows nuclear translocation upon Arp2/3 inhibition

A) (Left) Timelapse images showing representative cells expressing YPET-CCM2 treated in 0.25M sorbitol (top) or 100μM CK-666 (bottom) containing media for indicated time, scale bar: 10 μm; (Right) quantification of nuclear CCM2 from timelapse movies, N=20.

B) Fluorescent images showing a representative YPET-CCM2 expressing cell before (left) and after (right) 4 hrs of CK-666 treatment. Cells were plated in glass bottom dishes and time-lapse images were taken every 90 sec to monitor cell morphology change and CCM2 translocalization.

Arp2/3-depleted cells show altered osmotic-stress response

These observations suggest that the Arp2/3 complex and the branched actin network that it generates may play a role in osmotic stress responses. Cells depleted of Arp2/3 complex show significantly higher cell death under hyper-osmotic conditions (sorbitol treatment, Figure 31A). Using live-cell imaging, we observed a striking mobilization of Arp2/3 complex to cell periphery in response to hyper-osmotic stress (Figure 31B). Cells respond to varying osmotic conditions by dynamic volume regulation [88]. Whereas control cells decreased their cell volume in response to hyper-osmotic conditions, Arp2/3-depleted cells were unable to decrease their cell volume with hyper-osmitic stress, but did show enhanced swelling under hypo-osmotic conditions (Figure 31C).

p38MAPK is a stress-activated MAPK that is known to respond to osmotic stress [89]. To test the role of Arp2/3 in p38MAPK osmotic signaling, we blotted for p38MAPK phosphorylation in control and 2xKD cells treated with sorbitol. Control cells showed the expected transient activation of p38MAPK while Arp2/3-depleted cells had high basal p38MAPK activation that increased upon hyperosmotic stress, but never decreased, suggesting a defect in adaptation of this response without Arp2/3 complex (Figure 31D).

Based on the volume regulation and signaling defects in cells depleted of Arp2/3 complex, we postulated that reducing osmolarity (hypo-osmotic conditions) might rescue the aberrant stress signaling. Indeed, when we treated Arp2/3-depleted cells with hypo-osmotic media, we observed decreased p38MAPK activity within 1 hr and decreased NF-κB activity within 4 hrs (Figure 31E). Therefore, in the absence of

Arp2/3, cells appear unable to adapt to hyperosmotic stress with a physiological rapid decrease in volume, and exhibit evidence of activated signaling associated with hyper-osmotic state even when in isotonic media.

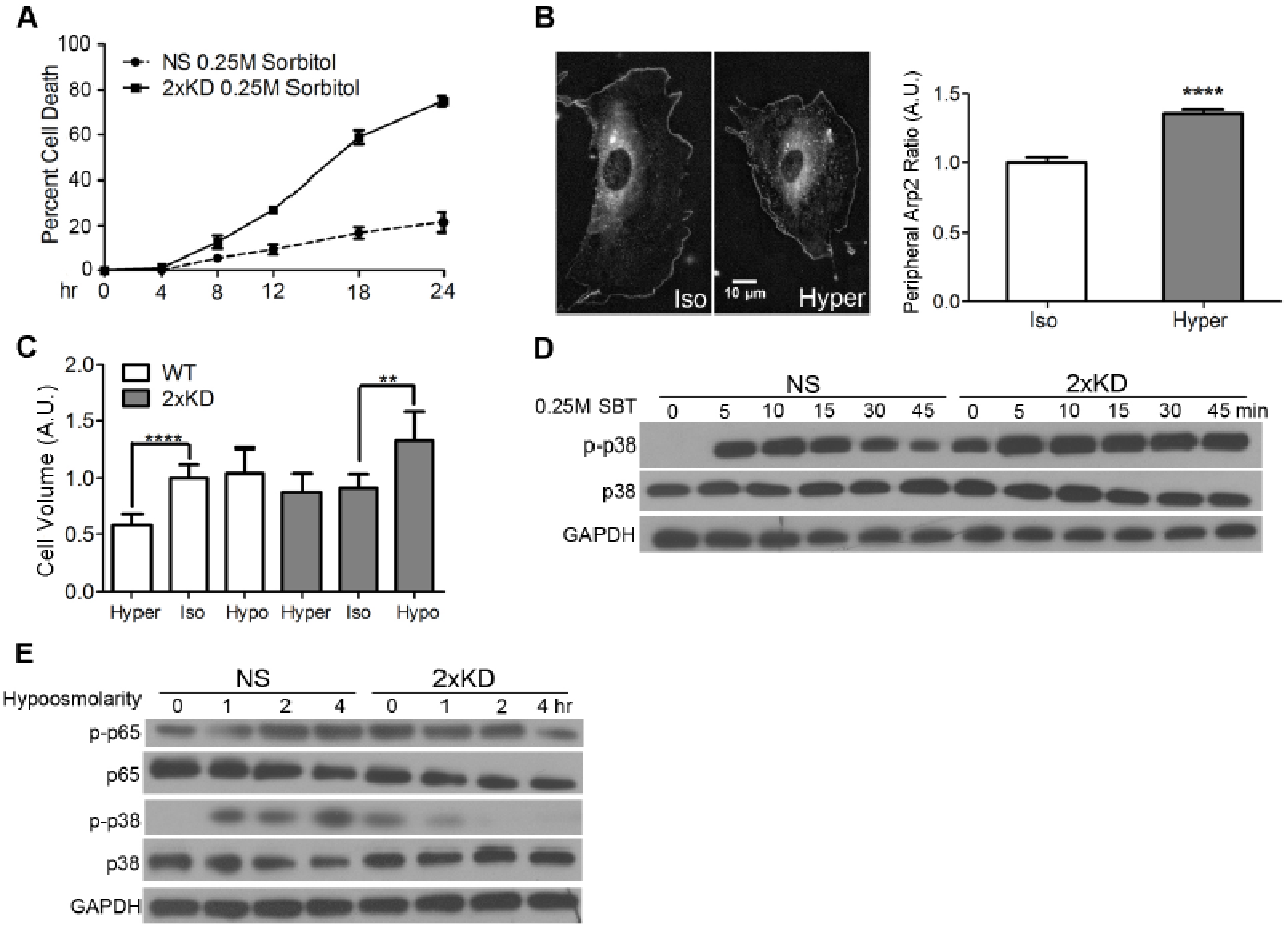
A
Percent Cell Death
NS 0.25M Sorbitol
2xKD 0.25M Sorbitol
hr
B
Iso
Hyper
10 μm
Peripheral Arp2 Ratio (A.U.)
****
C
Cell Volume (A.U.)
WT
2xKD
****
**
Hyper
Iso
Hypo
Hyper
Iso
Hypo
D
0.25M SBT
NS
2xKD
min
p-p38
p38
GAPDH
E
Hypoosmolarity
NS
2xKD
hr
p-p65
p65
p-p38
p38
GAPDH

Figure 31 Loss of Arp2/3 complex changes osmotic signaling

A) Graph showing cell death rate of NS and 2xKD cells in hyperosmotic conditions (0.25M sorbitol containing media). Cells were plated on fibronectin coated glass-bottom dishes. 1 µg/mL propidium iodide was added to the media before imaging cells for 24 hrs. Numbers of fluorescent cells (indicating cell death) and numbers of total cells were counted at indicated timepoints to plot the percent cell death. N=200 cells were analyzed for each group.

B) (Left) Representative images showing Arp2-EGFP-expressing cells under iso- and hyper-osmotic conditions. (Right) Quantification of peripheral Arp2 under iso- and hyper-osmotic conditions, N=30, ****P<0.001 by Student's t test. Cells were fixed and imaged as indicated in Methods. Arp2-EGFP signal were identified manually and its length versus the whole cell perimeter was defined as peripheral Arp2 ratio and plotted.

C) Graph showing cell volume of NS and 2xKD cells in hypo-, iso- (50% mixture of H_2O and DMEM media) and hyper- (0.25M sorbitol containing media) osmotic conditions for 20 min. N=80, ****P<0.001, **P<0.01 by Student's t test.

D) Western blot showing p-p38, p38 and GAPDH levels of NS and 2xKD cells under hyperosmotic conditions at different timepoints.

E) Western blot showing p-p65, p65, p-p38, p38 and GAPDH levels of NS and 2xKD cells in hypoosmotic conditions at different timepoints.

3.4 Discussion

In summary, our findings indicate that loss of Arp2/3 complex activates the NF-κB pathway and leads to strong increases in numerous secreted factors such as chemokines, growth factors and matrix metaloproteases (MMPs). This SASP-like response is mediated by the CCM2-MEKK3 pathway which is also critical for osmotic stress signaling. Consistent with this finding, Arp2/3-depleted cells are hyper-sensitive to osmotic stress and display elevated activation of this pathway under isotonic conditions. These findings indicate that Arp2/3-branched actin limits osmotic stress signaling and participates in the dynamic remodeling of the actin cortex when cells are challenged by hyperosmotic conditions. Whether Arp2/3-generated branched actin affects signaling though scaffolding, provides mechanical rigidity or both remains to be determined. These results also show that manipulation of the Arp2/3 actin cytoskeleton can lead to both cell autonomous and cell non-autonomous effects. These non-autonomous effects explain the context-dependent role of the Arp2/3 complex in fibroblast chemotaxis and could have far-reaching implications for the interpretation of experiments involving the manipulation of pathways upstream of Arp2/3 (eg. Rac/WAVE). Furthermore, this effect could explain why patients with Wiskott-Aldrich syndrome (who lack the Arp2/3-activating protein WASP) have cytoskeletal defects leading to immune cell dysfunction, as well as autoimmune and hyper-inflammatory complications such as arthritis and inflammatory bowel disease [90, 91], possibly due to increased transcription of inflammatory genes [92].

Non-cell autonoumous effects of Arp2/3 complex perturbation: Perhaps one of the most surprising findings we made was that perturbing Arp2/3-branched actin networks leads to the expected cell autonomous defects, but also non-cell autonomous effects via the up-regulation of genes encoding a variety of secreted proteins. We show that fibroblast chemotaxis can be significantly affected by these secreted factors, depending on the precise experimental regime. This finding resolves the contradictory findings of our group and Suraneni et al on the role of the Arp2/3 complex during fibroblast chemotaxis [29, 77]. In hindsight, each group got the expected result for the experiment performed based on the exchange of fresh media or lack thereof. However, this concept has much broader implications than explaining divergent experimental findings. The pro-inflammatory effects of perturbing Arp2/3 and possibly upstream regulatory pathways such as small GTPases (Rac, Cdc42) and Nucleation promoting factors (eg. Scar/WAVE) should be taken into consideration when evaluating phenotypes of knockout mice and in other experimental systems. In metastatic cancer, loss of the Cyfip1 subunit of the Wave Regulatory Complex has been shown to increase invasive behavior [93, 94]. While some of this effect may arise due to cell autonomous effects on the cytoskeleton, our findings suggest possible non-cell autonomous effects of secreted factors should also be examined in this case. Finally, loss of proper Arp2/3 regulation may also explain inflammatory and autoimmune phenotypes in human diseases such as Wiskott-Aldrich Syndrome where mutation of the WAS gene (encoding the Arp2/3-activating NPF WASp) may change the transcription of inflammatory genes in addition to altering cell autonomous functions [90, 92].

The relationship between Arp2/3 and CCM2-MEKK3- NF-κB signaling: Global disruption of the actin cytoskeleton is known to affect the activities of transcription factors including NF-κB [38, 39]. However, the underlying mechanisms of NF-κB activation induced by actin disrupting drugs are largely unknown. Here, using cultured cells and zebrafish embryos, we show the perturbation of a key regulator of branched actin leads to NF-κB activation and subsequent increased transcription of genes encoding secretory factors. We also identified the MAPK kinase MEKK3 and scaffold protein CCM2 as being critical for this pathway. MEKK3 participates in multiple signaling cascades, but CCM2 (aka OSM) was originally identified as a scaffold for MEKK3 with F-actin binding capability that is essential for the osmotic stress response [84]. Independently, CCM2 was identified as a gene mutated in cerebral cavernous malformation syndrome and is part of a complex of CCM proteins (including CCM1 and CCM3) that are thought to regulate vascular integrity and endothelial barrier function via RhoA signaling [95-98]. Our data indicate that CCM2 translocates to the nucleus upon hyper-osmotic stress or Arp2/3 inhibition. Interestingly, only a portion of the CCM2 translocates in either case suggesting that it may participate in multiple protein complexes that are under different regulatory control. The relationship between CCM2's function as an MEKK3 scaffold during osmotic stress response and its role in the CCM complex is unclear and will require further investigation.

The role of Arp2/3 complex in osmotic stress, volume regulation and the dynamic actin cortex: The actin cortex is critical for providing mechanical integrity of the plasma membrane and the homeostasis of cell volume in response to osmotic shifts

[99-101]. Defects in osmotic stress response leads to pathological conditions seen in corneal epithelial cells, osteoarthritic human articular chondrocytes, adipocytes and muscle cells [102-104]. Cells dynamically trigger signaling pathways, rearrange cytoskeleton networks, and alter their volume, in order to adapt to varying osmotic conditions [105, 106]. Although the actin cortex is central to osmotic adaptation, little is known about how cells nucleate, polymerize and remodel actin filament networks in the cortex to response to osmotic stress [107]. Here we have shown that Arp2/3 complex generated branched actin plays important role in adapting to osmotic stress. Future studies will focus on the specific NPFs that activate Arp2/3 complex in response to osmotic stress and the biochemical and mechanical consequences of this dynamic actin response.

3.5 Materials and methods

Reagents and Materials:

Commercial antibodies were obtained from Cell Signaling Technologies (Akt (pan), Phosphor-Akt(Ser473), p38 MAP Kinase, Phospho-p38 MAP Kinase (Thr180/Tyr182), NF-κB p65, Phospho-NF-κB p65 (Ser536), Phospho-HSP27 (Ser82)) and Ambion Applied Biosystems (Anti-GAPDH). Rhodamine Red-X and HRP conjugated secondary antibodies were from Jackson ImmunoResearch Laboratories. AlexaFluor647 dye conjugated phalloidin was from Invitrogen. p38MAPK inhibitor SB203580, Arp2/3 complex inhibitor CK-666 and its inactive control CK-689 were from EMD4Biosciences. D-sorbitol is from Sigma-Aldrich. Human plasma fibronectin, PDGF and EGF were from BD Biosciences. Western blotting was done by standard techniques.

Propidium iodide was from Sigma-Aldrich. IKK inhibitor cmpdA was a gift from the Baldwin Lab in UNC. Two QIAGEN siRNAs targeted against siCCM2 were used (SI00943446 & SI00943453).

RNA preparation, RNA-seq and qRT-PCR: Total RNA was isolated from cells (RNAeasy Plus, Qiagen) and validated to have RNA Integrity Numbers (RIN) above 8.5 using a Bioanalyzer (Agilent). For RNA-Seq, polyA+ RNA was enriched (Oligotex mRNA mini kit, Qiagen), fragmented (RNA Fragmentation Reagents, Ambion) and cDNA was generated (SuperScript II, Invitrogen) by random priming followed by second strand synthesis (DNA Polymerase I, Enzymatics) and purified (PCR purification kit, Qiagen). Libraries were prepared according to the manufacturer's

specifications (Illumina). Sequencing was performed using 50-bp single-end reads (Illumina HiSeq 2000). Reads were aligned to the reference mouse genome (mm9) using TopHat [108] and gene expression was estimated by calculating RPKM [109] for all Ensembl genes, analyzing only exonic reads. For qRT-PCR, cDNA was generated from total RNA (SuperScript II, Invitrogen) using a 50:50% mixture of random primers (Invitrogen) and oligo-dT primer (Promega). This cDNA was used directly with TaqMan Gene Expression Mastermix and TaqMan Gene Expression Assays (Applied Biosystems) to be read on a Viia7 qRT-PCR machine (Applied Biosystems). qRT-PCR data was analyzed by the Pfaffl method [110].

Cell culture and transient transfection: Cells were cultured in DMEM supplemented with 10% FBS (HyClone), 100 U/mL penicillin, 100 µg/mL streptomycin and 292 µg/mL L-glutamine. DMEM supplemented with 0.1% fatty-acid free BSA (Equitech-Bio), 100 U/mL penicillin, 100 µg/mL streptomycin and 292 µg/mL L-glutamine was used to culture cells during serum starvation. Transient transfections were performed using X-tremeGENE 9(Roche) for HEK293 FT cells and NanoJuice (Novagen) for IA32 cells. siRNA transfection was performed with Lipofectamine RNAiMax (Invitrogen).

Zebrafish experiments: All experiments using zebrafish were performed using protocols approved by the Animal Studies Committee of the University of North Carolina at Chapel Hill. Live zebrafish were anesthetized and imaged as described [111]. Day 2 post fertilization pNF-κB:EGFP zebrafish were treated with indicated drugs for 12 hrs before imaging. Fluorescence measurements within a given

experiment were collected using identical camera settings and analyzed at a common threshold. EGFP fluorescence densitometry of 8-bit grayscale images was performed using ImageJ software. For tissue analysis, areas of interest were selected using shape tools, recorded using the ROI manger, and applied to each image. Mean fluorescence intensity values were calculated for each image and plotted using Prism (GraphPad) software.

Cell Volume Measurement: Cells were treated with trypsin for 3 min when they were rounded and lifted from the culture dish. A gentle wash with sterile DPBS was performed before re-suspending cells in indicated osmotic solutions for 20 min. Cells were then mounted on coverslips to take DIC images. Cell diameter was measured with ImageJ to calculate cell volume.

Cell Viability Assay: Cells were plated on 10 µg/mL FN-coated glass bottom culture dishes (MatTek Corporation) for 8-12 hr before imaging. Propidium iodide was added to imaging dishes to a final concentration of 1 µg/mL. Time-lapse microscopy was performed on an Olympus VivaView FL incubator fluorescent microscope (20x objective) with a Hamamatsu camera (OrcaERAG - c4742-80-12AG). Fluorescent cells indicating cell death were counted at indicated timepoints. Curve of percent cell death was generated from Prism.

ELISAs and conditioned media: ELISA kit to detect IL-6 was from eBioscience. MMP3 was detected with ELISA kit from RayBio and HGF were detected with ELISA

kit from abcam. Cells were washed with serum-free DMEM and incubated in serum-free DMEM for 24 hrs. Media were collected and filtered before performing ELISAs. All ELISA data were normalized to cell number.

Light Microscopy and image analysis

Immunofluorescence: For immunofluorescent staining, the cells were fixed, stained and mounted as described previously (Bear et al., 2002). Cells were plated on acid-washed coverslips coated with 10 µg/mL FN overnight before fixing with 4% PFA and permeabilized in 0.1% Triton X-100 in PBS for 5 min. Cells were stained with AlexaFluor-647 phalloidin for F-actin (1:400 dilution). After three washes in PBS, the coverslips were mounted onto slides with Fluoromount G (Electron Microscopy Sciences). Images were captured using an IX-81 Olympus inverted microscope with a 60× 1.42 NA objective, a CCD camera (C4742-80-12AG, Hamamatsu) and an automated X–Y stage. Images were combined and annotated in Photoshop for presentation.

Nuclear CCM2 quantification: Fluorescent timelapse images were taken with cells expressing YPET-CCM2 under indicated conditions. Images at different timepoints were selected and cell nucleus outlined. Mean intensity of CCM2 signal within the outlined region was measured. Intensity was then normalized to time 0 and plotted using Prism.

Peripheral Arp2 quantification: Fluorescent images were taken with the same imaging set-up. Images were then processed with ImageJ software. Arp2-EGFP signal near cell edge were identified and drawn out with freehand line function. The length l of the line was then measured and recorded. The perimeter of the same cell was measured the same way and recorded as L. The ratio of l/L was defined as Peripheral Arp2 ratio for each cell.

Single cell tracking: Cells were plated on 10 μg/mL FN-coated glass bottom culture dishes (MatTek Corporation) for 8-12 hr before imaging. Time-lapse microscopy was performed on an Olympus VivaView FL incubator fluorescent microscope (20x objective) with a Hamamatsu camera (OrcaERAG - c4742-80-12AG). Cell speed was measured with ImageJ using the Manual Tracking plugin (http://rsbweb.nih.gov/ij/plugins/track/track.html).

Directional migration assays

Microfludic device preparation: Transparency masks were printed using a highresolution printer (Fineline Imaging, CO). The pattern for the chemotaxis chamber was fabricated on 4" silicon wafers using a two-step photolithography process. Polymethylsiloxane (PDMS) was then poured on the wafer and cured in overnight at 70ºC. Individual PDMS devices were cut out from the wafer and placed in a clean dish until use. Ports were then punched out in the devices. The devices were washed with water and ethanol and blow-dried.The PDMS device was placed into contact with glass dish bottom immediately following plasma treatment of both

pieces, ensuring that an irreversible seal was formed. The cell culture chamber was then filled with 10 µg/mL FN for 1 hr at 37 ºC, followed by flushing with sterile PBS. Cells were loaded into the cell culture chamber using a gel loading pipette tip. The cell chamber ports were plugged with short pieces of tubing (Upchurch Scientific, .0025” x 1/32”).

Chemotactic gradients: The exit ports of the sink and source channels were connected to waste using tubing of ID 0.015”. Gas tight 100 µL Hamilton glass syringes (81020,1710TLL 100 µL SYR) were connected to 27 1/2 gauge needles connected to tubing. The source syringe and tubing were filled indicated conditioned medium containing indicated chemoattractant and 10 µg/mL of TRITC-dextran to visualize the gradient. The sink syringe and tubing were filled with indicated conditioned medium only. The tubing was then inserted into the source and sink channels respectively, and the syringe pump was operated at a flow rate of 20 nL/min. A stable gradient was then established in the cell culture chamber within 30 min, and typically remained stable for 18 hr as monitored by TRITC-dextran fluorescent intensity.

Directional migration image acquisition and analysis: Chemotaxis assays were performed on an Olympus IX81 inverted microscope with a Hamamatsu orca-ER camera operated by MetaMorph imaging software. A 20X objective was used. Images were collected every 10 min for over 12 hr. Individual cells were manually tracked using ImageJ software Manual Tracking plug-in. The tracks obtained were

further analyzed using the chemotaxis tool developed by IBIDI (http://www.ibidi.de/applications/ap_chemotaxis.html#imageanalysis). This analysis tool was used to extract the Forward Migration Index (FMI) and histogram of angular direction of tracks from the manual tracking results. To obtain the Compass Parameter (CP), the histograms obtained were further analyzed in GraphPad Prism software by performing a non linear curve fit to the chemotaxis equation.

Chapter 4

Conclusions and future prospects

During the course of these studies, we have generated and characterized a stable mammalian cell line depleted of Arp2/3 complex. Using this cell line, we provided clear evidence supporting the role of Arp2/3 in making branched actin networks and maintaining lamellipodia structure. More importantly, we systematically investigated the cell autonomous and non-autonomous roles of Arp2/3-branched actin in cell migration. Our results show that Arp2/3-depleted cells have dramatically decreased random migration speed and defective haptotactic migration but are still capable of chemotaxis (Figure 32). Depletion of Arp2/3 activity affects NF-κB signaling pathways through MEKK3/CCM2, resulting in activation of secretory factors which in turn could affect cell migration in a non-autonomous way. Many questions such as the role of Arp2/3 in haptotaxis, the broader impact of non-cell-autonomous effects and the role of Arp2/3 in maintaining actin cortex remain to be answered.

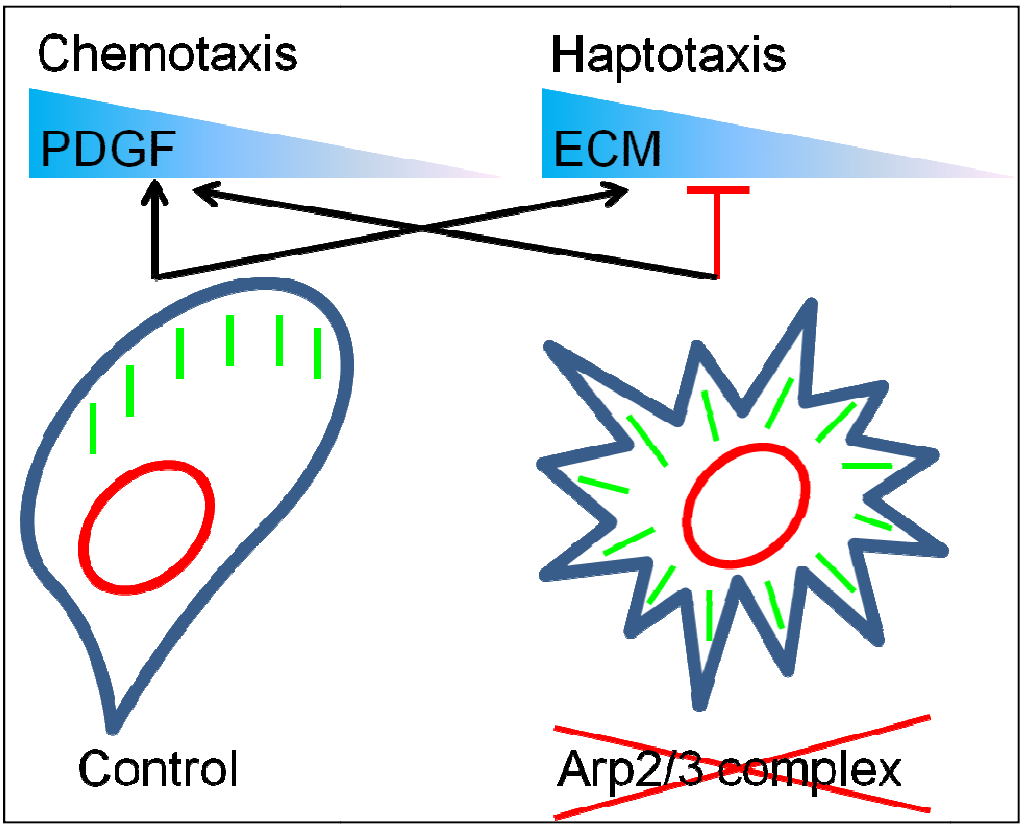

Figure 32 Graph illustrating the effects of Arp2/3-depletion on cell morphology, focal adhesion alignment, and directional migration

We showed that without Arp2/3 complex, cells are depleted of lamellipodia and have decreased 2D migration speed. We also showed that the Arp2/3-depleted cells have extensive filopodia and perform the “filling-the-gap” type of motility. By filling the gap between filopodia, Arp2/3-depleted cells undergo locomotion, partly explaining the residual motility in 2xKD cells. As we showed, lamellipodia formation and motility is totally dependent on Arp2/3 and branched actin while filopodia can be independent of this network. Moreover, without Arp2/3, cells are defected in haptotaxis. This raised the question of how the Arp2/3 complex affects haptotaxis. One significant difference we saw between wildtype and 2xKD cells is the organization of focal adhesions. Firstly, the focal adhesion alignment is dramatically decreased in 2xKD cells; secondly, we did not detect clear nascent adhesions in 2xKD cells which in the control cells reside as a thin line near the periphery of the lamellipodia; lastly, the elongated focal adhesions underneath the nucleus (presumably “fibrilla focal adhesions”) are not obvious in 2xKD cells. While other hypotheses are worth pursuing as well, the differences in focal adhesion formation and orientation are definitely very intriguing to look into. Perturbing focal adhesions in haptotaxis assays may reveal some clues. It is also useful to compare other haptotaxis-defect phenomena and compare the mechanisms with the Arp2/3-depletion condition.

We have identified the non-cell-autonomous role of Arp2/3 complex in chemotaxis. The secretory factors affect signaling pathways in EGF chemotaxis and decreased cell directionality. This is only one example of the non-cell-autonomous effects. The growth factors, cytokines and MMPs secreted by Arp2/3-depleted cells

may have other profound effects, especially considering in vivo situations. Whether the pro-inflammation factors will affect immune response in vivo, and whether the MMPs can facilitate tumor invasion are two interesting questions to follow up. With in vitro 3D co-culture system and in vivo characterizations, these hypotheses can be easily tested.

We showed that the Arp2/3-depleted cells have abnormal osmotic stress responses-one being the rewired signaling pathways, the other being the altered volume regulation. It has been reported that actin cortex is playing an important role in osmotic stress regulation [41], however, whether Arp2/3 plays a role in homeostasis of actin cortex is unknown. Our Arp2/3-depleted cells provide an ideal system to test whether the physical properties of the actin cortex are changed when the branched actin network is absent. Using 3D-Force Microscopy [112] and live-cell Atomic Force Microscopy [113], we will be able to access the role of Arp2/3 in cortex integrity and stiffness.

Here, I have described many unanswered questions about Arp2/3 function. The data presented in the earlier chapters has produced useful information about the multiple roles of Arp2/3 and branched actin in cell physiology. These data have opened a new area of Arp2/3 study that I hope will be beneficial for other researchers and future experiments may identify more key physiological roles for Arp2/3 and branched actin network.

References

1. Condeelis, J., R.H. Singer, and J.E. Segall, *The great escape: when cancer cells hijack the genes for chemotaxis and motility.* Annu Rev Cell Dev Biol, 2005. **21**: p. 695-718.

2. Wickramarachchi, D.C., A.N. Theofilopoulos, and D.H. Kono, *Immune pathology associated with altered actin cytoskeleton regulation.* Autoimmunity, 2010. **43**(1): p. 64-75.

3. Lammermann, T. and M. Sixt, *Mechanical modes of 'amoeboid' cell migration.* Curr Opin Cell Biol, 2009. **21**(5): p. 636-44.

4. O'Neill, G.M., *The coordination between actin filaments and adhesion in mesenchymal migration.* Cell Adh Migr, 2009. **3**(4): p. 355-7.

5. Ridley, A.J., et al., *Cell migration: integrating signals from front to back.* Science, 2003. **302**(5651): p. 1704-9.

6. Revenu, C., et al., *A new role for the architecture of microvillar actin bundles in apical retention of membrane proteins.* Mol Biol Cell, 2012. **23**(2): p. 324-36.

7. Cai, L., et al., *Coronin 1B coordinates Arp2/3 complex and cofilin activities at the leading edge.* Cell, 2007. **128**(5): p. 915-29.

8. Cai, L., et al., *Coronin 1B antagonizes cortactin and remodels Arp2/3-containing actin branches in lamellipodia.* Cell, 2008. **134**(5): p. 828-42.

9. Miki, H., S. Suetsugu, and T. Takenawa, *WAVE, a novel WASP-family protein involved in actin reorganization induced by Rac.* EMBO J, 1998. **17**(23): p. 6932-41.

10. Luo, L., *Rho GTPases in neuronal morphogenesis.* Nat Rev Neurosci, 2000. **1**(3): p. 173-80.

11. Watanabe, N., et al., *Cooperation between mDia1 and ROCK in Rho-induced actin reorganization.* Nat Cell Biol, 1999. **1**(3): p. 136-43.

12. Rouiller, I., et al., *The structural basis of actin filament branching by the Arp2/3 complex.* J Cell Biol, 2008. **180**(5): p. 887-95.

13. Goley, E.D. and M.D. Welch, *The ARP2/3 complex: an actin nucleator comes of age.* Nature Reviews Molecular Cell Biology, 2006. **7**(10): p. 713-726.

14. Veltman, D.M. and R.H. Insall, *WASP family proteins: their evolution and its physiological implications.* Mol Biol Cell, 2010. **21**(16): p. 2880-93.

15. Pollard, T.D., *Regulation of actin filament assembly by Arp2/3 complex and formins.* Annu Rev Biophys Biomol Struct, 2007. **36**: p. 451-77.

16. Higgs, H.N. and T.D. Pollard, *Regulation of actin polymerization by Arp2/3 complex and WASp/Scar proteins.* J Biol Chem, 1999. **274**(46): p. 32531-4.

17. Weaver, A.M., et al., *Cortactin promotes and stabilizes Arp2/3-induced actin filament network formation.* Curr Biol, 2001. **11**(5): p. 370-4.

18. Zencheck, W.D., et al., *Nucleotide- and activator-dependent structural and dynamic changes of arp2/3 complex monitored by hydrogen/deuterium exchange and mass spectrometry.* J Mol Biol, 2009. **390**(3): p. 414-27.

19. Gandhi, M., et al., *GMF is a cofilin homolog that binds Arp2/3 complex to stimulate filament debranching and inhibit actin nucleation.* Curr Biol, 2010. **20**(9): p. 861-7.

20. Maritzen, T., et al., *Gadkin negatively regulates cell spreading and motility via sequestration of the actin-nucleating ARP2/3 complex.* Proc Natl Acad Sci U S A, 2012. **109**(26): p. 10382-7.

21. Rocca, D.L., et al., *Inhibition of Arp2/3-mediated actin polymerization by PICK1 regulates neuronal morphology and AMPA receptor endocytosis.* Nat Cell Biol, 2008. **10**(3): p. 259-71.

22. Pollard, T. and G. Borisy, *Cellular motility driven by assembly and disassembly of actin filaments.* Cell, 2003. **112**(4): p. 453-65.

23. Schwob, E. and R.P. Martin, *New yeast actin-like gene required late in the cell cycle.* Nature, 1992. **355**(6356): p. 179-82.

24. Zaki, M., et al., *Replacement of the essential Dictyostelium Arp2 gene by its Entamoeba homologue using parasexual genetics.* BMC genetics, 2007. **8**: p. 28.

25. Yae, K., et al., *Sleeping beauty transposon-based phenotypic analysis of mice: lack of Arpc3 results in defective trophoblast outgrowth.* Mol Cell Biol, 2006. **26**(16): p. 6185-96.

26. Pollard, T.D. and J.A. Cooper, *Actin, a Central Player in Cell Shape and Movement.* Science, 2009. **326**(5957): p. 1208-1212.

27. Allen, C.D., et al., *Imaging of germinal center selection events during affinity maturation.* Science, 2007. **315**(5811): p. 528-31.

28. Swaney, K.F., C.H. Huang, and P.N. Devreotes, *Eukaryotic chemotaxis: a network of signaling pathways controls motility, directional sensing, and polarity.* Annu Rev Biophys, 2010. **39**: p. 265-89.

29. Wu, C., et al., *Arp2/3 is critical for lamellipodia and response to extracellular matrix cues but is dispensable for chemotaxis.* Cell, 2012. **148**(5): p. 973-87.

30. Vicente-Manzanares, M., *Cell migration: cooperation between myosin II isoforms in durotaxis.* Curr Biol, 2013. **23**(1): p. R28-9.

31. Rotty, J.D., C. Wu, and J.E. Bear, *New insights into the regulation and cellular functions of the ARP2/3 complex.* Nat Rev Mol Cell Biol, 2013. **14**(1): p. 7-12.

32. Bear, J.E., et al., *Negative regulation of fibroblast motility by Ena/VASP proteins.* Cell, 2000. **101**(7): p. 717-28.

33. Bear, J.E., et al., *Antagonism between Ena/VASP proteins and actin filament capping regulates fibroblast motility.* Cell, 2002. **109**(4): p. 509-21.

34. Spiering, D. and L. Hodgson, *Dynamics of the Rho-family small GTPases in actin regulation and motility.* Cell Adh Migr, 2011. **5**(2): p. 170-80.

35. Carpenter, C.L., *Actin cytoskeleton and cell signaling.* Crit Care Med, 2000. **28**(4 Suppl): p. N94-9.

36. Vicente-Manzanares, M., C.K. Choi, and A.R. Horwitz, *Integrins in cell migration--the actin connection.* J Cell Sci, 2009. **122**(Pt 2): p. 199-206.

37. Pathak, R., et al., *The microtubule-associated Rho activating factor GEF-H1 interacts with exocyst complex to regulate vesicle traffic.* Dev Cell, 2012. **23**(2): p. 397-411.

38. Descot, A., et al., *Negative regulation of the EGFR-MAPK cascade by actin-MAL-mediated Mig6/Errfi-1 induction.* Mol Cell, 2009. **35**(3): p. 291-304.

39. Kustermans, G., et al., *Perturbation of actin dynamics induces NF-kappaB activation in myelomonocytic cells through an NADPH oxidase-dependent pathway.* Biochem J, 2005. **387**(Pt 2): p. 531-40.

40. Coppe, J.P., et al., *Senescence-associated secretory phenotypes reveal cell-nonautonomous functions of oncogenic RAS and the p53 tumor suppressor.* PLoS Biol, 2008. **6**(12): p. 2853-68.

41. Ohtani, N. and E. Hara, *Roles and mechanisms of cellular senescence in regulation of tissue homeostasis.* Cancer Sci, 2013.

42. Condeelis, J., R.H. Singer, and J.E. Segall, *The great escape: when cancer cells hijack the genes for chemotaxis and motility.* Annual review of cell and developmental biology, 2005. **21**: p. 695-718.

43. Swaney, K.F., C.H. Huang, and P.N. Devreotes, *Eukaryotic chemotaxis: a network of signaling pathways controls motility, directional sensing, and polarity.* Annual review of biophysics, 2010. **39**: p. 265-89.

44. Parent, C.A., *Making all the right moves: chemotaxis in neutrophils and Dictyostelium.* Current opinion in cell biology, 2004. **16**(1): p. 4-13.

45. Thiery, J.P., *Mechanisms of cell migration in the vertebrate embryo.* Cell differentiation, 1984. **15**(1): p. 1-15.

46. Wynn, T.A., *Cellular and molecular mechanisms of fibrosis.* The Journal of pathology, 2008. **214**(2): p. 199-210.

47. Svitkina, T.M. and G.G. Borisy, *Arp2/3 complex and actin depolymerizing factor/cofilin in dendritic organization and treadmilling of actin filament array in lamellipodia.* The Journal of cell biology, 1999. **145**(5): p. 1009-26.

48. Webb, D.J., J.T. Parsons, and A.F. Horwitz, *Adhesion assembly, disassembly and turnover in migrating cells -- over and over and over again.* Nature cell biology, 2002. **4**(4): p. E97-100.

49. Goley, E.D. and M.D. Welch, *The ARP2/3 complex: an actin nucleator comes of age.* Nature reviews. Molecular cell biology, 2006. **7**(10): p. 713-26.

50. Rogers, S.L., et al., *Molecular requirements for actin-based lamella formation in Drosophila S2 cells.* J Cell Biol, 2003. **162**(6): p. 1079-88.

51. Nicholson-Dykstra, S.M. and H.N. Higgs, *Arp2 depletion inhibits sheet-like protrusions but not linear protrusions of fibroblasts and lymphocytes.* Cell motility and the cytoskeleton, 2008. **65**(11): p. 904-22.

52. Steffen, A., et al., *Filopodia formation in the absence of functional WAVE- and Arp2/3-complexes.* Molecular biology of the cell, 2006. **17**(6): p. 2581-91.

53. Di Nardo, A., et al., *Arp2/3 complex-deficient mouse fibroblasts are viable and have normal leading-edge actin structure and function.* Proceedings of the National Academy of Sciences of the United States of America, 2005. **102**(45): p. 16263-8.

54. Urban, E., et al., *Electron tomography reveals unbranched networks of actin filaments in lamellipodia.* Nature cell biology, 2010. **12**(5): p. 429-35.

55. Vitriol, E.A., et al., *Enhanced EGFP-chromophore-assisted laser inactivation using deficient cells rescued with functional EGFP-fusion proteins.* Proc Natl Acad Sci U S A, 2007. **104**(16): p. 6702-7.

56. Kamijo, T., et al., *Tumor suppression at the mouse INK4a locus mediated by the alternative reading frame product p19ARF.* Cell, 1997. **91**(5): p. 649-59.

57. Ozgur, S., B. Damania, and J. Griffith, *The Kaposi's sarcoma-associated herpesvirus ORF6 DNA binding protein forms long DNA-free helical protein filaments.* Journal of structural biology, 2011. **174**(1): p. 37-43.

58. Nolen, B.J., et al., *Characterization of two classes of small molecule inhibitors of Arp2/3 complex.* Nature, 2009. **460**(7258): p. 1031-4.

59. Goeckeler, Z.M., P.C. Bridgman, and R.B. Wysolmerski, *Nonmuscle myosin II is responsible for maintaining endothelial cell basal tone and stress fiber integrity.* American journal of physiology. Cell physiology, 2008. **295**(4): p. C994-1006.

60. Shamloo, A., et al., *Endothelial cell polarization and chemotaxis in a microfluidic device.* Lab on a chip, 2008. **8**(8): p. 1292-9.

61. Arrieumerlou, C. and T. Meyer, *A local coupling model and compass parameter for eukaryotic chemotaxis.* Developmental cell, 2005. **8**(2): p. 215-27.

62. DiMilla, P.A., et al., *Maximal migration of human smooth muscle cells on fibronectin and type IV collagen occurs at an intermediate attachment strength.* J Cell Biol, 1993. **122**(3): p. 729-37.

63. Gupton, S.L. and C.M. Waterman-Storer, *Spatiotemporal feedback between actomyosin and focal-adhesion systems optimizes rapid cell migration.* Cell, 2006. **125**(7): p. 1361-74.

64. Berginski, M.E., et al., *High-resolution quantification of focal adhesion spatiotemporal dynamics in living cells.* PLoS ONE, 2011. **6**(7): p. e22025.

65. Kim, W.Y. and N.E. Sharpless, *The regulation of INK4/ARF in cancer and aging.* Cell, 2006. **127**(2): p. 265-75.

66. Mullins, R., J. Heuser, and T. Pollard, *The interaction of Arp2/3 complex with actin: nucleation, high affinity pointed end capping, and formation of branching networks of filaments.* Proc Natl Acad Sci U S A, 1998. **95**(11): p. 6181-6.

67. Monypenny, J., et al., *Cdc42 and Rac family GTPases regulate mode and speed but not direction of primary fibroblast migration during platelet-derived growth factor-dependent chemotaxis.* Molecular and cellular biology, 2009. **29**(10): p. 2730-47.

68. Hoeller, O. and R.R. Kay, *Chemotaxis in the absence of PIP3 gradients.* Current biology : CB, 2007. **17**(9): p. 813-7.

69. Melvin, A.T., et al., *In chemotaxing fibroblasts, both high-fidelity and weakly biased cell movements track the localization of PI3K signaling.* Biophysical journal, 2011. **100**(8): p. 1893-901.

70. Isaji, T., et al., *N-glycosylation of the I-like domain of beta1 integrin is essential for beta1 integrin expression and biological function: identification of the minimal N-glycosylation requirement for alpha5beta1.* The Journal of biological chemistry, 2009. **284**(18): p. 12207-16.

71. Katsumoto, T., et al., *The effect of tannic acid on the preservation of tissue culture cells for scanning electron microscopy.* Journal of electron microscopy, 1981. **30**(3): p. 177-82.

72. Svitkina, T.M.a.B., G. G., *Correlative light and electron microscopy studies of cytoskeletal dynamics.* Cell Biology: A Laboratory Handbook (Ed. J. Celis), 2005. **v. 3**(Chapter 28): p. 277-286.

73. Burridge, K. and E.S. Wittchen, *The tension mounts: stress fibers as force-generating mechanotransducers.* J Cell Biol, 2013. **200**(1): p. 9-19.

74. Campisi, J., *Aging and cancer cell biology, 2008.* Aging Cell, 2008. **7**(3): p. 281-4.

75. Freund, A., C.K. Patil, and J. Campisi, *p38MAPK is a novel DNA damage response-independent regulator of the senescence-associated secretory phenotype.* EMBO J, 2011. **30**(8): p. 1536-48.

76. Salminen, A., A. Kauppinen, and K. Kaarniranta, *Emerging role of NF-kappaB signaling in the induction of senescence-associated secretory phenotype (SASP).* Cell Signal, 2012. **24**(4): p. 835-45.

77. Suraneni, P., et al., *The Arp2/3 complex is required for lamellipodia extension and directional fibroblast cell migration.* J Cell Biol, 2012. **197**(2): p. 239-51.

78. Shamloo, A., et al., *Endothelial cell polarization and chemotaxis in a microfluidic device.* Lab Chip, 2008. **8**(8): p. 1292-9.

79. Kuilman, T., et al., *Oncogene-induced senescence relayed by an interleukin-dependent inflammatory network.* Cell, 2008. **133**(6): p. 1019-31.

80. Chien, Y., et al., *Control of the senescence-associated secretory phenotype by NF-kappaB promotes senescence and enhances chemosensitivity.* Genes Dev, 2011. **25**(20): p. 2125-36.

81. Karin, M., *Nuclear factor-kappaB in cancer development and progression.* Nature, 2006. **441**(7092): p. 431-6.

82. Stein, S.J. and A.S. Baldwin, *NF-kappaB suppresses ROS levels in BCR-ABL(+) cells to prevent activation of JNK and cell death.* Oncogene, 2011. **30**(45): p. 4557-66.

83. Kanther, M., et al., *Microbial colonization induces dynamic temporal and spatial patterns of NF-kappaB activation in the zebrafish digestive tract.* Gastroenterology, 2011. **141**(1): p. 197-207.

84. Uhlik, M.T., et al., *Rac-MEKK3-MKK3 scaffolding for p38 MAPK activation during hyperosmotic shock.* Nat Cell Biol, 2003. **5**(12): p. 1104-10.

85. Sun, W. and J. Yang, *Molecular basis of lysophosphatidic acid-induced NF-kappaB activation.* Cell Signal, 2010. **22**(12): p. 1799-803.

86. Schmidt, C., et al., *Mechanisms of proinflammatory cytokine-induced biphasic NF-kappaB activation.* Mol Cell, 2003. **12**(5): p. 1287-300.

87. Maruyama, T., et al., *CHIP-dependent termination of MEKK2 regulates temporal ERK activation required for proper hyperosmotic response.* EMBO J, 2010. **29**(15): p. 2501-14.

88. Hoffmann, E.K. and S.F. Pedersen, *Sensors and signal transduction pathways in vertebrate cell volume regulation.* Contrib Nephrol, 2006. **152**: p. 54-104.

89. Nielsen, M.B., S.T. Christensen, and E.K. Hoffmann, *Effects of osmotic stress on the activity of MAPKs and PDGFR-beta-mediated signal transduction in NIH-3T3 fibroblasts.* Am J Physiol Cell Physiol, 2008. **294**(4): p. C1046-55.

90. Dupuis-Girod, S., et al., *Autoimmunity in Wiskott-Aldrich syndrome: risk factors, clinical features, and outcome in a single-center cohort of 55 patients.* Pediatrics, 2003. **111**(5 Pt 1): p. e622-7.

91. Goyal, R., et al., *Rheumatologic and autoimmune manifestations of primary immunodeficiency disorders.* Curr Opin Rheumatol, 2009. **21**(1): p. 78-84.

92. Prete, F., et al., *Wiskott-Aldrich syndrome protein-mediated actin dynamics control type-I interferon production in plasmacytoid dendritic cells.* J Exp Med, 2013.

93. Silva, J.M., et al., *Cyfip1 is a putative invasion suppressor in epithelial cancers.* Cell, 2009. **137**(6): p. 1047-61.

94. Machesky, L.M. and H.R. Tang, *Actin-based protrusions: promoters or inhibitors of cancer invasion?* Cancer Cell, 2009. **16**(1): p. 5-7.

95. Stockton, R.A., et al., *Cerebral cavernous malformations proteins inhibit Rho kinase to stabilize vascular integrity.* J Exp Med, 2010. **207**(4): p. 881-96.

96. Borikova, A.L., et al., *Rho kinase inhibition rescues the endothelial cell cerebral cavernous malformation phenotype.* J Biol Chem, 2010. **285**(16): p. 11760-4.

97. Faurobert, E. and C. Albiges-Rizo, *Recent insights into cerebral cavernous malformations: a complex jigsaw puzzle under construction.* FEBS J, 2010. **277**(5): p. 1084-96.

98. Liquori, C.L., et al., *Mutations in a gene encoding a novel protein containing a phosphotyrosine-binding domain cause type 2 cerebral cavernous malformations.* Am J Hum Genet, 2003. **73**(6): p. 1459-64.

99. Pedersen, S.F., E.K. Hoffmann, and J.W. Mills, *The cytoskeleton and cell volume regulation.* Comp Biochem Physiol A Mol Integr Physiol, 2001. **130**(3): p. 385-99.

100. Henson, J.H., *Relationships between the actin cytoskeleton and cell volume regulation.* Microsc Res Tech, 1999. **47**(2): p. 155-62.

101. Moustakas, A., et al., *The cytoskeleton in cell volume regulation.* Contrib Nephrol, 1998. **123**: p. 121-34.

102. Ly, D.L., et al., *Hyperosmotic stress regulates the distribution and stability of myocardin-related transcription factor, a key modulator of the cytoskeleton.* Am J Physiol Cell Physiol, 2013. **304**(2): p. C115-27.

103. Chen, Z., et al., *Hyperosmolarity-induced cornification of human corneal epithelial cells is regulated by JNK MAPK.* Invest Ophthalmol Vis Sci, 2008. **49**(2): p. 539-49.

104. Gual, P., Y. Le Marchand-Brustel, and J. Tanti, *Positive and negative regulation of glucose uptake by hyperosmotic stress.* Diabetes Metab, 2003. **29**(6): p. 566-75.

105. Lang, F., *Mechanisms and significance of cell volume regulation.* J Am Coll Nutr, 2007. **26**(5 Suppl): p. 613S-623S.

106. Hoffmann, E.K., I.H. Lambert, and S.F. Pedersen, *Physiology of cell volume regulation in vertebrates.* Physiol Rev, 2009. **89**(1): p. 193-277.

107. Salbreux, G., G. Charras, and E. Paluch, *Actin cortex mechanics and cellular morphogenesis.* Trends Cell Biol, 2012. **22**(10): p. 536-45.

108. Trapnell, C., L. Pachter, and S.L. Salzberg, *TopHat: discovering splice junctions with RNA-Seq.* Bioinformatics, 2009. **25**(9): p. 1105-11.

109. Mortazavi, A., et al., *Mapping and quantifying mammalian transcriptomes by RNA-Seq.* Nat Methods, 2008. **5**(7): p. 621-8.

110. Pfaffl, M.W., *A new mathematical model for relative quantification in real-time RT-PCR.* Nucleic Acids Res, 2001. **29**(9): p. e45.

111. Flynn, E.J., 3rd, C.M. Trent, and J.F. Rawls, *Ontogeny and nutritional control of adipogenesis in zebrafish (Danio rerio).* J Lipid Res, 2009. **50**(8): p. 1641-52.

112. Guilluy, C., et al., *The Rho GEFs LARG and GEF-H1 regulate the mechanical response to force on integrins.* Nat Cell Biol, 2011. **13**(6): p. 722-7.

113. Heinisch, J.J., et al., *Atomic force microscopy - looking at mechanosensors on the cell surface.* J Cell Sci, 2012. **125**(Pt 18): p. 4189-95.